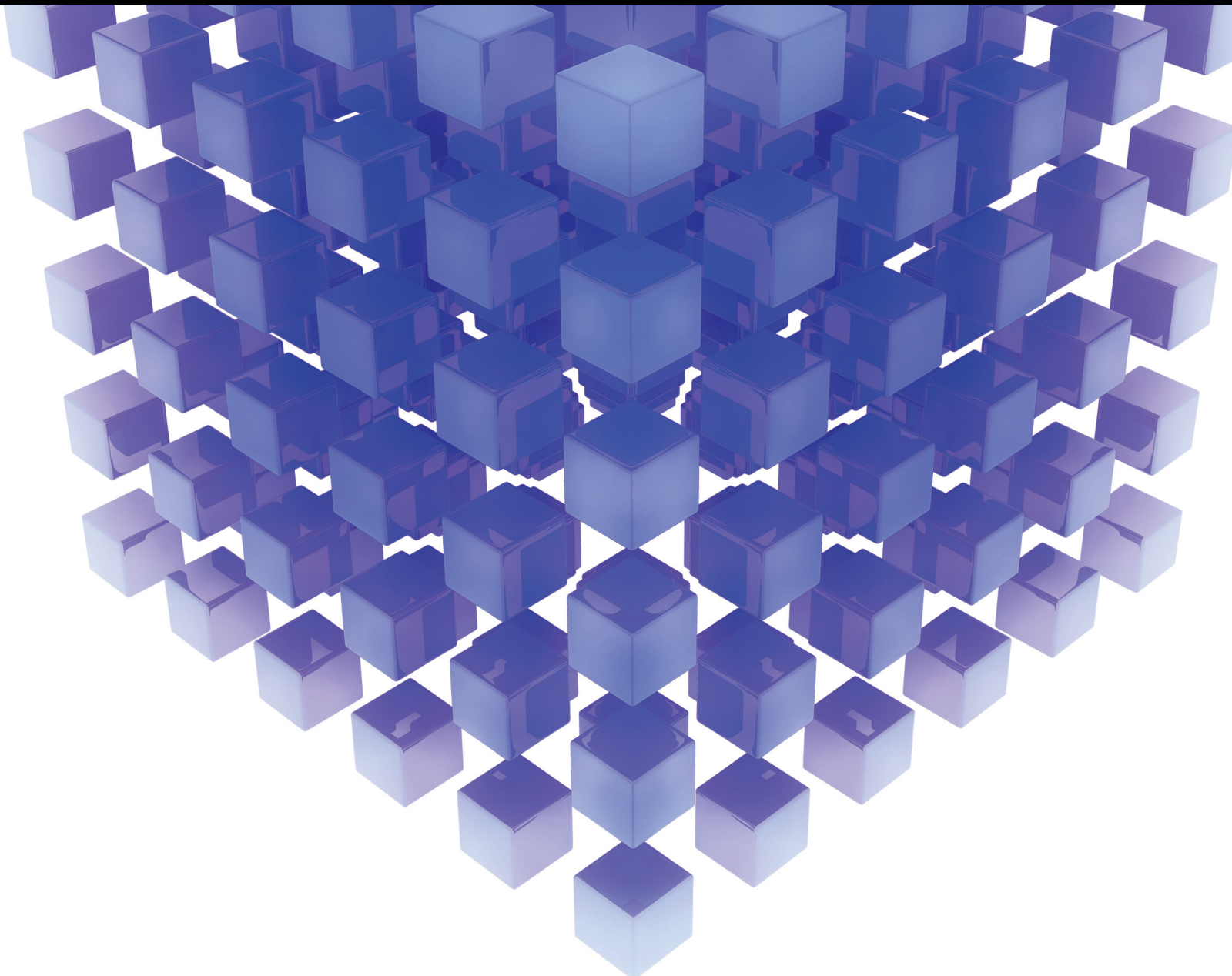


Mathematical Problems in Engineering

# Intelligent Management of Oil and Gas Storage and Transportation Systems

Lead Guest Editor: Haoran Zhang

Guest Editors: Qi Liao and Yufei Wang





---

# **Intelligent Management of Oil and Gas Storage and Transportation Systems**

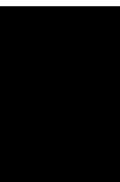
Mathematical Problems in Engineering

---

# **Intelligent Management of Oil and Gas Storage and Transportation Systems**

Lead Guest Editor: Haoran Zhang

Guest Editors: Qi Liao and Yufei Wang




---

Copyright © 2021 Hindawi Limited. All rights reserved.

This is a special issue published in “Mathematical Problems in Engineering.” All articles are open access articles distributed under the Creative Commons Attribution License, which permits unrestricted use, distribution, and reproduction in any medium, provided the original work is properly cited.



# Chief Editor

Guangming Xie , China

## Academic Editors

Kumaravel A , India  
Waqas Abbasi, Pakistan  
Mohamed Abd El Aziz , Egypt  
Mahmoud Abdel-Aty , Egypt  
Mohammed S. Abdo, Yemen  
Mohammad Yaghoub Abdollahzadeh  
Jamalabadi , Republic of Korea  
Rahib Abiyev , Turkey  
Leonardo Acho , Spain  
Daniela Addessi , Italy  
Arooj Adeel , Pakistan  
Waleed Adel , Egypt  
Ramesh Agarwal , USA  
Francesco Aggogeri , Italy  
Ricardo Aguilar-Lopez , Mexico  
Afaq Ahmad , Pakistan  
Naveed Ahmed , Pakistan  
Elias Aifantis , USA  
Akif Akgul , Turkey  
Tareq Al-shami , Yemen  
Guido Ala, Italy  
Andrea Alaimo , Italy  
Reza Alam, USA  
Osamah Albahri , Malaysia  
Nicholas Alexander , United Kingdom  
Salvatore Alfonzetti, Italy  
Ghous Ali , Pakistan  
Nouman Ali , Pakistan  
Mohammad D. Aliyu , Canada  
Juan A. Almendral , Spain  
A.K. Alomari, Jordan  
José Domingo Álvarez , Spain  
Cláudio Alves , Portugal  
Juan P. Amezcua-Sanchez, Mexico  
Mukherjee Amitava, India  
Lionel Amodeo, France  
Sebastian Anita, Romania  
Costanza Arico , Italy  
Sabri Arik, Turkey  
Fausto Arpino , Italy  
Rashad Asharabi , Saudi Arabia  
Farhad Aslani , Australia  
Mohsen Asle Zaem , USA

Andrea Avanzini , Italy  
Richard I. Avery , USA  
Viktor Avrutin , Germany  
Mohammed A. Awadallah , Malaysia  
Francesco Aymerich , Italy  
Sajad Azizi , Belgium  
Michele Bacciocchi , Italy  
Seungik Baek , USA  
Khaled Bahlali, France  
M.V.A Raju Bahubalendruni, India  
Pedro Balaguer , Spain  
P. Balasubramaniam, India  
Stefan Balint , Romania  
Ines Tejado Balsera , Spain  
Alfonso Banos , Spain  
Jerzy Baranowski , Poland  
Tudor Barbu , Romania  
Andrzej Bartoszewicz , Poland  
Sergio Baselga , Spain  
S. Caglar Baslamisli , Turkey  
David Bassir , France  
Chiara Bedon , Italy  
Azeddine Beghdadi, France  
Andriette Bekker , South Africa  
Francisco Beltran-Carbajal , Mexico  
Abdellatif Ben Makhlof , Saudi Arabia  
Denis Benasciutti , Italy  
Ivano Benedetti , Italy  
Rosa M. Benito , Spain  
Elena Benvenuti , Italy  
Giovanni Berselli, Italy  
Michele Betti , Italy  
Pietro Bia , Italy  
Carlo Bianca , France  
Simone Bianco , Italy  
Vincenzo Bianco, Italy  
Vittorio Bianco, Italy  
David Bigaud , France  
Sardar Muhammad Bilal , Pakistan  
Antonio Bilotta , Italy  
Sylvio R. Bistafa, Brazil  
Chiara Boccaletti , Italy  
Rodolfo Bontempo , Italy  
Alberto Borboni , Italy  
Marco Bortolini, Italy

Paolo Boscariol, Italy  
Daniela Boso , Italy  
Guillermo Botella-Juan, Spain  
Abdesselem Boulkroune , Algeria  
Boulaïd Boulkroune, Belgium  
Fabio Bovenga , Italy  
Francesco Braghin , Italy  
Ricardo Branco, Portugal  
Julien Bruchon , France  
Matteo Bruggi , Italy  
Michele Brun , Italy  
Maria Elena Bruni, Italy  
Maria Angela Butturi , Italy  
Bartłomiej Błachowski , Poland  
Dhanamjayulu C , India  
Raquel Caballero-Águila , Spain  
Filippo Cacace , Italy  
Salvatore Caddemi , Italy  
Zuowei Cai , China  
Roberto Caldelli , Italy  
Francesco Cannizzaro , Italy  
Maosen Cao , China  
Ana Carpio, Spain  
Rodrigo Carvajal , Chile  
Caterina Casavola, Italy  
Sara Casciati, Italy  
Federica Caselli , Italy  
Carmen Castillo , Spain  
Inmaculada T. Castro , Spain  
Miguel Castro , Portugal  
Giuseppe Catalanotti , United Kingdom  
Alberto Cavallo , Italy  
Gabriele Cazzulani , Italy  
Fatih Vehbi Celebi, Turkey  
Miguel Cerrolaza , Venezuela  
Gregory Chagnon , France  
Ching-Ter Chang , Taiwan  
Kuei-Lun Chang , Taiwan  
Qing Chang , USA  
Xiaoheng Chang , China  
Prasenjit Chatterjee , Lithuania  
Kacem Chehdi, France  
Peter N. Cheimets, USA  
Chih-Chiang Chen , Taiwan  
He Chen , China



































Kebing Chen , China  
Mengxin Chen , China  
Shyi-Ming Chen , Taiwan  
Xizhong Chen , Ireland  
Xue-Bo Chen , China  
Zhiwen Chen , China  
Qiang Cheng, USA  
Zeyang Cheng, China  
Luca Chiapponi , Italy  
Francisco Chicano , Spain  
Tirivanhu Chinyoka , South Africa  
Adrian Chmielewski , Poland  
Seongim Choi , USA  
Gautam Choubey , India  
Hung-Yuan Chung , Taiwan  
Yusheng Ci, China  
Simone Cinquemani , Italy  
Roberto G. Citarella , Italy  
Joaquim Ciurana , Spain  
John D. Clayton , USA  
Piero Colajanni , Italy  
Giuseppina Colicchio, Italy  
Vassilios Constantoudis , Greece  
Enrico Conte, Italy  
Alessandro Contento , USA  
Mario Cools , Belgium  
Gino Cortellessa, Italy  
Carlo Cosentino , Italy  
Paolo Crippa , Italy  
Erik Cuevas , Mexico  
Guozeng Cui , China  
Mehmet Cunkas , Turkey  
Giuseppe D'Aniello , Italy  
Peter Dabnichki, Australia  
Weizhong Dai , USA  
Zhifeng Dai , China  
Purushothaman Damodaran , USA  
Sergey Dashkovskiy, Germany  
Adiel T. De Almeida-Filho , Brazil  
Fabio De Angelis , Italy  
Samuele De Bartolo , Italy  
Stefano De Miranda , Italy  
Filippo De Monte , Italy

José António Fonseca De Oliveira  
Correia , Portugal  
Jose Renato De Sousa , Brazil  
Michael Defoort, France  
Alessandro Della Corte, Italy  
Laurent Dewasme , Belgium  
Sanku Dey , India  
Gianpaolo Di Bona , Italy  
Roberta Di Pace , Italy  
Francesca Di Puccio , Italy  
Ramón I. Diego , Spain  
Yannis Dimakopoulos , Greece  
Hasan Dinçer , Turkey  
José M. Domínguez , Spain  
Georgios Dounias, Greece  
Bo Du , China  
Emil Dumic, Croatia  
Madalina Dumitriu , United Kingdom  
Premraj Durairaj , India  
Saeed Eftekhar Azam, USA  
Said El Kafhali , Morocco  
Antonio Elipe , Spain  
R. Emre Erkmen, Canada  
John Escobar , Colombia  
Leandro F. F. Miguel , Brazil  
FRANCESCO FOTI , Italy  
Andrea L. Facci , Italy  
Shahla Faisal , Pakistan  
Giovanni Falsone , Italy  
Hua Fan, China  
Jianguang Fang, Australia  
Nicholas Fantuzzi , Italy  
Muhammad Shahid Farid , Pakistan  
Hamed Faruqi, Iran  
Yann Favennec, France  
Fiorenzo A. Fazzolari , United Kingdom  
Giuseppe Fedele , Italy  
Roberto Fedele , Italy  
Baowei Feng , China  
Mohammad Ferdows , Bangladesh  
Arturo J. Fernández , Spain  
Jesus M. Fernandez Oro, Spain  
Francesco Ferrise, Italy  
Eric Feulvarch , France  
Thierry Floquet, France


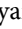




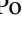





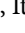
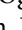



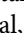

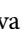
Eric Florentin , France  
Gerardo Flores, Mexico  
Antonio Forcina , Italy  
Alessandro Formisano, Italy  
Francesco Franco , Italy  
Elisa Francomano , Italy  
Juan Frausto-Solis, Mexico  
Shujun Fu , China  
Juan C. G. Prada , Spain  
HECTOR GOMEZ , Chile  
Matteo Gaeta , Italy  
Mauro Gaggero , Italy  
Zoran Gajic , USA  
Jaime Gallardo-Alvarado , Mexico  
Mosè Gallo , Italy  
Akemi Gálvez , Spain  
Maria L. Gandarias , Spain  
Hao Gao , Hong Kong  
Xingbao Gao , China  
Yan Gao , China  
Zhiwei Gao , United Kingdom  
Giovanni Garcea , Italy  
José García , Chile  
Harish Garg , India  
Alessandro Gasparetto , Italy  
Stylianos Georgantzinou, Greece  
Fotios Georgiades , India  
Parviz Ghadimi , Iran  
Ştefan Cristian Gherghina , Romania  
Georgios I. Giannopoulos , Greece  
Agathoklis Giaralis , United Kingdom  
Anna M. Gil-Lafuente , Spain  
Ivan Giorgio , Italy  
Gaetano Giunta , Luxembourg  
Jefferson L.M.A. Gomes , United Kingdom  
Emilio Gómez-Déniz , Spain  
Antonio M. Gonçalves de Lima , Brazil  
Qunxi Gong , China  
Chris Goodrich, USA  
Rama S. R. Gorla, USA  
Veena Goswami , India  
Xunjie Gou , Spain  
Jakub Grabski , Poland

Antoine Grall , France  
George A. Gravvanis , Greece  
Fabrizio Greco , Italy  
David Greiner , Spain  
Jason Gu , Canada  
Federico Guarracino , Italy  
Michele Guida , Italy  
Muhammet Gul , Turkey  
Dong-Sheng Guo , China  
Hu Guo , China  
Zhaoxia Guo, China  
Yusuf Gurefe, Turkey  
Salim HEDDAM , Algeria  
ABID HUSSANAN, China  
Quang Phuc Ha, Australia  
Li Haitao , China  
Petr Hájek , Czech Republic  
Mohamed Hamdy , Egypt  
Muhammad Hamid , United Kingdom  
Renke Han , United Kingdom  
Weimin Han , USA  
Xingsi Han, China  
Zhen-Lai Han , China  
Thomas Hanne , Switzerland  
Xinan Hao , China  
Mohammad A. Hariri-Ardebili , USA  
Khalid Hattaf , Morocco  
Defeng He , China  
Xiao-Qiao He, China  
Yanchao He, China  
Yu-Ling He , China  
Ramdane Hedjar , Saudi Arabia  
Jude Hemanth , India  
Reza Hemmati, Iran  
Nicolae Herisanu , Romania  
Alfredo G. Hernández-Díaz , Spain  
M.I. Herreros , Spain  
Eckhard Hitzer , Japan  
Paul Honeine , France  
Jaromir Horacek , Czech Republic  
Lei Hou , China  
Yingkun Hou , China  
Yu-Chen Hu , Taiwan  
Yunfeng Hu, China  
Can Huang , China  
Gordon Huang , Canada  
Linsheng Huo , China  
Sajid Hussain, Canada  
Asier Ibeas , Spain  
Orest V. Iftime , The Netherlands  
Przemyslaw Ignaciuk , Poland  
Giacomo Innocenti , Italy  
Emilio Insfran Pelozo , Spain  
Azeem Irshad, Pakistan  
Alessio Ishizaka, France  
Benjamin Ivorra , Spain  
Breno Jacob , Brazil  
Reema Jain , India  
Tushar Jain , India  
Amin Jajarmi , Iran  
Chiranjibe Jana , India  
Łukasz Jankowski , Poland  
Samuel N. Jator , USA  
Juan Carlos Jáuregui-Correa , Mexico  
Kandasamy Jayakrishna, India  
Reza Jazar, Australia  
Khalide Jbilou, France  
Isabel S. Jesus , Portugal  
Chao Ji , China  
Qing-Chao Jiang , China  
Peng-fei Jiao , China  
Ricardo Fabricio Escobar Jiménez , Mexico  
Emilio Jiménez Macías , Spain  
Maolin Jin, Republic of Korea  
Zhuo Jin, Australia  
Ramash Kumar K , India  
BHABEN KALITA , USA  
MOHAMMAD REZA KHEDMATI , Iran  
Viacheslav Kalashnikov , Mexico  
Mathiyalagan Kalidass , India  
Tamas Kalmar-Nagy , Hungary  
Rajesh Kaluri , India  
Jyottheswara Reddy Kalvakurthi, India  
Zhao Kang , China  
Ramani Kannan , Malaysia  
Tomasz Kapitaniak , Poland  
Julius Kaplunov, United Kingdom  
Konstantinos Karamanos, Belgium  
Michal Kawulok, Poland

Irfan Kaymaz , Turkey  
Vahid Kayvanfar , Qatar  
Krzysztof Kecik , Poland  
Mohamed Khader , Egypt  
Chaudry M. Khalique , South Africa  
Mukhtaj Khan , Pakistan  
Shahid Khan , Pakistan  
Nam-Il Kim, Republic of Korea  
Philipp V. Kiryukhantsev-Korneev ,  
Russia  
P.V.V Kishore , India  
Jan Koci , Czech Republic  
Ioannis Kostavelis , Greece  
Sotiris B. Kotsiantis , Greece  
Frederic Kratz , France  
Vamsi Krishna , India  
Edyta Kucharska, Poland  
Krzysztof S. Kulpa , Poland  
Kamal Kumar, India  
Prof. Ashwani Kumar , India  
Michal Kunicki , Poland  
Cedrick A. K. Kwuimy , USA  
Kyandoghere Kyamakya, Austria  
Ivan Kyrchei , Ukraine  
Márcio J. Lacerda , Brazil  
Eduardo Lalla , The Netherlands  
Giovanni Lancioni , Italy  
Jaroslaw Latalski , Poland  
Hervé Laurent , France  
Agostino Lauria , Italy  
Aimé Lay-Ekuakille , Italy  
Nicolas J. Leconte , France  
Kun-Chou Lee , Taiwan  
Dimitri Lefebvre , France  
Eric Lefevre , France  
Marek Lefik, Poland  
Yaguo Lei , China  
Kauko Leiviskä , Finland  
Ervin Lenzi , Brazil  
ChenFeng Li , China  
Jian Li , USA  
Jun Li , China  
Yueyang Li , China  
Zhao Li , China

Zhen Li , China  
En-Qiang Lin, USA  
Jian Lin , China  
Qibin Lin, China  
Yao-Jin Lin, China  
Zhiyun Lin , China  
Bin Liu , China  
Bo Liu , China  
Heng Liu , China  
Jianxu Liu , Thailand  
Lei Liu , China  
Sixin Liu , China  
Wanquan Liu , China  
Yu Liu , China  
Yuanchang Liu , United Kingdom  
Bonifacio Llamazares , Spain  
Alessandro Lo Schiavo , Italy  
Jean Jacques Loiseau , France  
Francesco Lolli , Italy  
Paolo Lonetti , Italy  
António M. Lopes , Portugal  
Sebastian López, Spain  
Luis M. López-Ochoa , Spain  
Vassilios C. Loukopoulos, Greece  
Gabriele Maria Lozito , Italy  
Zhiguo Luo , China  
Gabriel Luque , Spain  
Valentin Lychagin, Norway  
YUE MEI, China  
Junwei Ma , China  
Xuanlong Ma , China  
Antonio Madeo , Italy  
Alessandro Magnani , Belgium  
Toqeer Mahmood , Pakistan  
Fazal M. Mahomed , South Africa  
Arunava Majumder , India  
Sarfranz Nawaz Malik, Pakistan  
Paolo Manfredi , Italy  
Adnan Maqsood , Pakistan  
Muazzam Maqsood, Pakistan  
Giuseppe Carlo Marano , Italy  
Damijan Markovic, France  
Filipe J. Marques , Portugal  
Luca Martinelli , Italy  
Denizar Cruz Martins, Brazil






























Francisco J. Martos , Spain  
Elio Masciari , Italy  
Paolo Massioni , France  
Alessandro Mauro , Italy  
Jonathan Mayo-Maldonado , Mexico  
Pier Luigi Mazzeo , Italy  
Laura Mazzola, Italy  
Driss Mehdi , France  
Zahid Mehmood , Pakistan  
Roderick Melnik , Canada  
Xiangyu Meng , USA  
Jose Merodio , Spain  
Alessio Merola , Italy  
Mahmoud Mesbah , Iran  
Luciano Mescia , Italy  
Laurent Mevel , France  
Constantine Michailides , Cyprus  
Mariusz Michta , Poland  
Prankul Middha, Norway  
Aki Mikkola , Finland  
Giovanni Minafò , Italy  
Edmondo Minisci , United Kingdom  
Hiroyuki Mino , Japan  
Dimitrios Mitsotakis , New Zealand  
Ardashir Mohammadzadeh , Iran  
Francisco J. Montáns , Spain  
Francesco Montefusco , Italy  
Gisele Mophou , France  
Rafael Morales , Spain  
Marco Morandini , Italy  
Javier Moreno-Valenzuela , Mexico  
Simone Morganti , Italy  
Caroline Mota , Brazil  
Aziz Moukrim , France  
Shen Mouquan , China  
Dimitris Mourtzis , Greece  
Emiliano Mucchi , Italy  
Taseer Muhammad, Saudi Arabia  
Ghulam Muhiuddin, Saudi Arabia  
Amitava Mukherjee , India  
Josefa Mula , Spain  
Jose J. Muñoz , Spain  
Giuseppe Muscolino, Italy  
Marco Mussetta , Italy

Hariharan Muthusamy, India  
Alessandro Naddeo , Italy  
Raj Nandkeolyar, India  
Keivan Navaie , United Kingdom  
Soumya Nayak, India  
Adrian Neagu , USA  
Erivelton Geraldo Nepomuceno , Brazil  
AMA Neves, Portugal  
Ha Quang Thinh Ngo , Vietnam  
Nhon Nguyen-Thanh, Singapore  
Papakostas Nikolaos , Ireland  
Jelena Nikolic , Serbia  
Tatsushi Nishi, Japan  
Shanzhou Niu , China  
Ben T. Nohara , Japan  
Mohammed Nouari , France  
Mustapha Nourelfath, Canada  
Kazem Nouri , Iran  
Ciro Núñez-Gutiérrez , Mexico  
Włodzimierz Ogryczak, Poland  
Roger Ohayon, France  
Krzysztof Okarma , Poland  
Mitsuhiro Okayasu, Japan  
Murat Olgun , Turkey  
Diego Oliva, Mexico  
Alberto Olivares , Spain  
Enrique Onieva , Spain  
Calogero Orlando , Italy  
Susana Ortega-Cisneros , Mexico  
Sergio Ortobelli, Italy  
Naohisa Otsuka , Japan  
Sid Ahmed Ould Ahmed Mahmoud , Saudi Arabia  
Taoreed Owolabi , Nigeria  
EUGENIA PETROPOULOU , Greece  
Arturo Pagano, Italy  
Madhumangal Pal, India  
Pasquale Palumbo , Italy  
Dragan Pamučar, Serbia  
Weifeng Pan , China  
Chandan Pandey, India  
Rui Pang, United Kingdom  
Jürgen Pannek , Germany  
Elena Panteley, France  
Achille Paolone, Italy

George A. Papakostas , Greece  
Xosé M. Pardo , Spain  
You-Jin Park, Taiwan  
Manuel Pastor, Spain  
Pubudu N. Pathirana , Australia  
Surajit Kumar Paul , India  
Luis Payá , Spain  
Igor Pažanin , Croatia  
Libor Pekař , Czech Republic  
Francesco Pellicano , Italy  
Marcello Pellicciari , Italy  
Jian Peng , China  
Mingshu Peng, China  
Xiang Peng , China  
Xindong Peng, China  
Yuexing Peng, China  
Marzio Pennisi , Italy  
Maria Patrizia Pera , Italy  
Matjaz Perc , Slovenia  
A. M. Bastos Pereira , Portugal  
Wesley Peres, Brazil  
F. Javier Pérez-Pinal , Mexico  
Michele Perrella, Italy  
Francesco Pesavento , Italy  
Francesco Petrini , Italy  
Hoang Vu Phan, Republic of Korea  
Lukasz Pieczonka , Poland  
Dario Piga , Switzerland  
Marco Pizzarelli , Italy  
Javier Plaza , Spain  
Goutam Pohit , India  
Dragan Poljak , Croatia  
Jorge Pomares , Spain  
Hiram Ponce , Mexico  
Sébastien Poncet , Canada  
Volodymyr Ponomaryov , Mexico  
Jean-Christophe Ponsart , France  
Mauro Pontani , Italy  
Sivakumar Poruran, India  
Francesc Pozo , Spain  
Aditya Rio Prabowo , Indonesia  
Anchasa Pramuanjaroenkij , Thailand  
Leonardo Primavera , Italy  
B Rajanarayan Prusty, India

Krzysztof Puszynski , Poland  
Chuan Qin , China  
Dongdong Qin, China  
Jianlong Qiu , China  
Giuseppe Quaranta , Italy  
DR. RITU RAJ , India  
Vitomir Racic , Italy  
Carlo Rainieri , Italy  
Kumbakonam Ramamani Rajagopal, USA  
Ali Ramazani , USA  
Angel Manuel Ramos , Spain  
Higinio Ramos , Spain  
Muhammad Afzal Rana , Pakistan  
Muhammad Rashid, Saudi Arabia  
Manoj Rastogi, India  
Alessandro Rasulo , Italy  
S.S. Ravindran , USA  
Abdolrahman Razani , Iran  
Alessandro Reali , Italy  
Jose A. Reinoso , Spain  
Oscar Reinoso , Spain  
Haijun Ren , China  
Carlo Renno , Italy  
Fabrizio Renno , Italy  
Shahram Rezapour , Iran  
Ricardo Rianza , Spain  
Francesco Riganti-Fulginei , Italy  
Gerasimos Rigatos , Greece  
Francesco Ripamonti , Italy  
Jorge Rivera , Mexico  
Eugenio Roanes-Lozano , Spain  
Ana Maria A. C. Rocha , Portugal  
Luigi Rodino , Italy  
Francisco Rodríguez , Spain  
Rosana Rodríguez López, Spain  
Francisco Rossomando , Argentina  
Jose de Jesus Rubio , Mexico  
Weiguo Rui , China  
Rubén Ruiz , Spain  
Ivan D. Rukhlenko , Australia  
Dr. Eswaramoorthi S. , India  
Weichao SHI , United Kingdom  
Chaman Lal Sabharwal , USA  
Andrés Sáez , Spain



Bekir Sahin, Turkey  
Laxminarayan Sahoo , India  
John S. Sakellariou , Greece  
Michael Sakellariou , Greece  
Salvatore Salamone, USA  
Jose Vicente Salcedo , Spain  
Alejandro Salcido , Mexico  
Alejandro Salcido, Mexico  
Nunzio Salerno , Italy  
Rohit Salgotra , India  
Miguel A. Salido , Spain  
Sinan Salih , Iraq  
Alessandro Salvini , Italy  
Abdus Samad , India  
Sovan Samanta, India  
Nikolaos Samaras , Greece  
Ramon Sancibrian , Spain  
Giuseppe Sanfilippo , Italy  
Omar-Jacobo Santos, Mexico  
J Santos-Reyes , Mexico  
José A. Sanz-Herrera , Spain  
Musavarah Sarwar, Pakistan  
Shahzad Sarwar, Saudi Arabia  
Marcelo A. Savi , Brazil  
Andrey V. Savkin, Australia  
Tadeusz Sawik , Poland  
Roberta Sburlati, Italy  
Gustavo Scaglia , Argentina  
Thomas Schuster , Germany  
Hamid M. Sedighi , Iran  
Mijanur Rahaman Seikh, India  
Tapan Senapati , China  
Lotfi Senhadji , France  
Junwon Seo, USA  
Michele Serpilli, Italy  
Silvestar Šesnić , Croatia  
Gerardo Severino, Italy  
Ruben Sevilla , United Kingdom  
Stefano Sfarra , Italy  
Dr. Ismail Shah , Pakistan  
Leonid Shaikhet , Israel  
Vimal Shanmuganathan , India  
Prayas Sharma, India  
Bo Shen , Germany  
Hang Shen, China

Xin Pu Shen, China  
Dimitri O. Shepelsky, Ukraine  
Jian Shi , China  
Amin Shokrollahi, Australia  
Suzanne M. Shontz , USA  
Babak Shotorban , USA  
Zhan Shu , Canada  
Angelo Sifaleras , Greece  
Nuno Simões , Portugal  
Mehakpreet Singh , Ireland  
Piyush Pratap Singh , India  
Rajiv Singh, India  
Seralathan Sivamani , India  
S. Sivasankaran , Malaysia  
Christos H. Skiadas, Greece  
Konstantina Skouri , Greece  
Neale R. Smith , Mexico  
Bogdan Smolka, Poland  
Delfim Soares Jr. , Brazil  
Alba Sofi , Italy  
Francesco Soldovieri , Italy  
Raffaele Solimene , Italy  
Yang Song , Norway  
Jussi Sopanen , Finland  
Marco Spadini , Italy  
Paolo Spagnolo , Italy  
Ruben Specogna , Italy  
Vasilios Spitas , Greece  
Ivanka Stamova , USA  
Rafał Stanisławski , Poland  
Miladin Stefanović , Serbia  
Salvatore Strano , Italy  
Yakov Strelniker, Israel  
Kangkang Sun , China  
Qiuqin Sun , China  
Shuaishuai Sun, Australia  
Yanchao Sun , China  
Zong-Yao Sun , China  
Kumarasamy Suresh , India  
Sergey A. Suslov , Australia  
D.L. Suthar, Ethiopia  
D.L. Suthar , Ethiopia  
Andrzej Swierniak, Poland  
Andras Szekrenyes , Hungary  
Kumar K. Tamma, USA



Yong (Aaron) Tan, United Kingdom  
Marco Antonio Taneco-Hernández , Mexico  
Lu Tang , China  
Tianyou Tao, China  
Hafez Tari , USA  
Alessandro Tasora , Italy  
Sergio Teggi , Italy  
Adriana del Carmen Téllez-Anguiano , Mexico  
Ana C. Teodoro , Portugal  
Efstathios E. Theotokoglou , Greece  
Jing-Feng Tian, China  
Alexander Timokha , Norway  
Stefania Tomasiello , Italy  
Gisella Tomasini , Italy  
Isabella Torcicollo , Italy  
Francesco Tornabene , Italy  
Mariano Torrisi , Italy  
Thang nguyen Trung, Vietnam  
George Tsiatas , Greece  
Le Anh Tuan , Vietnam  
Nerio Tullini , Italy  
Emilio Turco , Italy  
Ilhan Tuzcu , USA  
Efstratios Tzirtzilakis , Greece  
FRANCISCO UREÑA , Spain  
Filippo Ubertini , Italy  
Mohammad Uddin , Australia  
Mohammad Safi Ullah , Bangladesh  
Serdar Ulubeyli , Turkey  
Mati Ur Rahman , Pakistan  
Panayiotis Vafeas , Greece  
Giuseppe Vairo , Italy  
Jesus Valdez-Resendiz , Mexico  
Eusebio Valero, Spain  
Stefano Valvano , Italy  
Carlos-Renato Vázquez , Mexico  
Martin Velasco Villa , Mexico  
Franck J. Vernerey, USA  
Georgios Veronis , USA  
Vincenzo Vespri , Italy  
Renato Vidoni , Italy  
Venkatesh Vijayaraghavan, Australia


Anna Vila, Spain  
Francisco R. Villatoro , Spain  
Francesca Vipiana , Italy  
Stanislav Vitek , Czech Republic  
Jan Vorel , Czech Republic  
Michael Vynnycky , Sweden  
Mohammad W. Alomari, Jordan  
Roman Wan-Wendner , Austria  
Bingchang Wang, China  
C. H. Wang , Taiwan  
Dagang Wang, China  
Guoqiang Wang , China  
Huaiyu Wang, China  
Hui Wang , China  
J.G. Wang, China  
Ji Wang , China  
Kang-Jia Wang , China  
Lei Wang , China  
Qiang Wang, China  
Qingling Wang , China  
Weiwei Wang , China  
Xinyu Wang , China  
Yong Wang , China  
Yung-Chung Wang , Taiwan  
Zhenbo Wang , USA  
Zhibo Wang, China  
Waldemar T. Wójcik, Poland  
Chi Wu , Australia  
Qihong Wu, China  
Yuqiang Wu, China  
Zhibin Wu , China  
Zhizheng Wu , China  
Michalis Xenos , Greece  
Hao Xiao , China  
Xiao Ping Xie , China  
Qingzheng Xu , China  
Binghan Xue , China  
Yi Xue , China  
Joseph J. Yame , France  
Chuanliang Yan , China  
Xinggang Yan , United Kingdom  
Hongtai Yang , China  
Jixiang Yang , China  
Mijia Yang, USA  
Ray-Yeng Yang, Taiwan

Zaoli Yang , China  
Jun Ye , China  
Min Ye , China  
Luis J. Yebra , Spain  
Peng-Yeng Yin , Taiwan  
Muhammad Haroon Yousaf , Pakistan  
Yuan Yuan, United Kingdom  
Qin Yuming, China  
Elena Zaitseva , Slovakia  
Arkadiusz Zak , Poland  
Mohammad Zakwan , India  
Ernesto Zambrano-Serrano , Mexico  
Francesco Zammori , Italy  
Jessica Zangari , Italy  
Rafal Zdunek , Poland  
Ibrahim Zeid, USA  
Nianyin Zeng , China  
Junyong Zhai , China  
Hao Zhang , China  
Haopeng Zhang , USA  
Jian Zhang , China  
Kai Zhang, China  
Lingfan Zhang , China  
Mingjie Zhang , Norway  
Qian Zhang , China  
Tianwei Zhang , China  
Tongqian Zhang , China  
Wenyu Zhang , China  
Xianming Zhang , Australia  
Xuping Zhang , Denmark  
Yinyan Zhang, China  
Yifan Zhao , United Kingdom  
Debao Zhou, USA  
Heng Zhou , China  
Jian G. Zhou , United Kingdom  
Junyong Zhou , China  
Xueqian Zhou , United Kingdom  
Zhe Zhou , China  
Wu-Le Zhu, China  
Gaetano Zizzo , Italy  
Mingcheng Zuo, China

# Contents

---


## **An Improved High-Intelligence Method of Gas and Oil Pipeline Prewarning System in Real Soil Environment**

Fang Wang, Jichuan Xing , Jinxin Li, Feng Zhao, and Shufeng Zhang  
Research Article (13 pages), Article ID 6673325, Volume 2021 (2021)

## **An FBG Strain Sensor-Based NPW Method for Natural Gas Pipeline Leakage Detection**

Qingmin Hou   
Research Article (8 pages), Article ID 5548503, Volume 2021 (2021)

## **Modified Leakage Rate Calculation Models of Natural Gas Pipelines**

Qingmin Hou , Daheng Yang, Xiaoyan Li, Guanghua Xiao, and Siu Chun Michael Ho  
Research Article (10 pages), Article ID 6673107, Volume 2020 (2020)

## **A Multisource Monitoring Data Coupling Analysis Method for Stress States of Oil Pipelines under Permafrost Thawing Settlement Load**

Changliang Jiang , Pengchao Chen , Rui Li , and Xiaoben Liu   
Research Article (15 pages), Article ID 6696680, Volume 2020 (2020)

## Research Article

# An Improved High-Intelligence Method of Gas and Oil Pipeline Prewarning System in Real Soil Environment

Fang Wang,<sup>1</sup> Jichuan Xing<sup>1</sup> ,<sup>1</sup> Jinxin Li,<sup>1</sup> Feng Zhao,<sup>2</sup> and Shufeng Zhang<sup>3</sup>

<sup>1</sup>Optoelectronic Department, Beijing Institute of Technology, Beijing 100081, China

<sup>2</sup>Hilong Petroleum Information Technology Company, Hilong Group of Companies, Shanghai 201103, China

<sup>3</sup>College of Computing, Southeast University, Nanjing 211189, China

Correspondence should be addressed to Jichuan Xing; michaelhsing@bit.edu.cn

Received 8 February 2021; Revised 22 February 2021; Accepted 18 September 2021; Published 19 October 2021

Academic Editor: Yufei Wang

Copyright © 2021 Fang Wang et al. This is an open access article distributed under the Creative Commons Attribution License, which permits unrestricted use, distribution, and reproduction in any medium, provided the original work is properly cited.

With the development of technology, the total extent of global pipeline transportation is also increased. However, the traditional long-distance optical fiber prewarning system has poor real-time performance and high false alarm rate when recognizing events threatening pipeline safety. The same vibration signal would vary greatly when collected in different soil environments and this problem would reduce the signal recognition accuracy of the prewarning system. In this paper, we studied this effect theoretically and analyzed soil vibration signals under different soil conditions. Then we studied the signal acquisition problem of long-distance gas and oil pipeline prewarning system in real soil environment. Ultimately, an improved high-intelligence method was proposed for optimization. This method is based on the real application environment, which is more suitable for the recognition of optical fiber vibration signals. Through experiments, the method yielded high recognition accuracy of above 95%. The results indicate that the method can significantly improve signal acquisition and recognition and has good adaptability and real-time performance in the real soil environment.

## 1. Introduction

Pipeline integrity is vital to the transmission of gas and oil [1–4]. Timely discovering the intrusion events around the pipelines and preventing pipeline leakage is the major direction of current researches. The optical fiber prewarning system (OFPS) is mainly used in underground cable and pipeline transportation safety. In comparison to other methods, distributed optical fiber sensing technology is used in the OFPS with higher positioning accuracy and sensitivity and lower investment cost [5–8]. Mainly, the OFPS includes two components of Pattern Recognition System (PRS) and Distributed Acoustic sensing System (DAS). DAS is a distributed acoustic wave sensing system enabling remote monitoring, and PRS is utilized to recognize and classify various events from the DAS-collected data. In this paper, the DAS based on the  $\Phi$ -Optical Time-domain Reflectometry ( $\Phi$ -OTDR) principle is utilized to collect the soil vibration signal [9–11]. Normally, gas and oil pipelines are

laid in a complex geographical environment. The same vibration signals will vary greatly when collected in different soil environments and this problem can reduce the signal recognition accuracy of the OFPS. The signal acquisition of the OFPS in the real soil environment is complicated and different from the simple environment in the laboratory [12, 13]. Figure 1 represents the OFPS in the real soil environment. The whole process is similar to a black box from the occurrence to the identification and classification of the vibration signals caused by the intrusion events [14, 15].

Currently, commonly used gas and oil pipeline prewarning technologies mainly include optical fiber sensing and seismic wave detection. Seismic wave detection technology is mainly used in places where there is no communication optical cable. The monitoring distance of a single seismic wave sensor is 150–200 m. Since the installation and maintenance of each sensor requires excavation, which leads to higher use and maintenance costs, this technology is only suitable for monitoring of key pipe

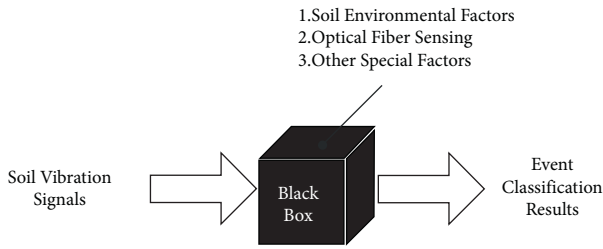


FIGURE 1: OFPS in the real soil environment.

sections [16]. Therefore, the long-distance gas and oil pipeline prewarning system mainly uses optical fiber sensing technology. According to the different optical principles used, the optical fiber sensing pipeline prewarning technology can be divided into four types: Mach-Zehnder, Sagnac, Bragg fiber grating, and  $\Phi$ -OTDR. The Mach-Zehnder technology requires a 3-core optical fiber, and the sensitivity of the system is limited; when multiple vibration events occur simultaneously, the system cannot distinguish and identify [17]. The structure of the Sagnac technology system is relatively complex, and the length of the delay fiber is required to be much larger than the length of the sensing fiber of the interferometer, which increases the difficulty of application [18]. The technology of Bragg fiber grating is complicated, and the installation and maintenance cost are relatively high [19]. The  $\Phi$ -OTDR method occupies less fiber resources, has higher sensitivity, can detect weak vibration signals, and can monitor and locate multiple vibration events that occur simultaneously at multiple points along the pipeline. Thus, the most commonly used today is the  $\Phi$ -OTDR technology. In recent years, some researches provide techniques to represent the system recognition accuracy of  $\Phi$ -ODTR [20]. Various  $\Phi$ -OTDR-based vibration sensor schemes have been suggested to increment the dynamic range (DR) and the signal-to-noise (SNR) of the vibration measurement by controlling or reducing the noise present in the system [21–23]. For a given spatial resolution (SR), increasing the optical peak power input to the fiber via an erbium doped fiber amplifier (EDFA) increases the DR and the SNR of the system. Other techniques have emerged to break totally this dilemma in the  $\Phi$ -OTDR system and enabled improving significantly the SR [24, 25]. Such methods mainly involve the linear frequency modulation pulse compression and the chirp pulse amplification. In these researches, only the optical fiber sensing system itself is enhanced; however, the recognition algorithm is not improved.

Artificial intelligence algorithms are applied in various fields of industry [26]. There are also some different algorithms in the field of optical fiber sensing. Different algorithms lead to significant differences in the accuracy of external intrusion event detection. Most of the methods used in the previous researches are hard to be applied. First, in some researches the signal used to input into the neural network (NN) is mainly about the feature vectors constructed by decomposing the signal spectra from the multilayer wavelets. The wavelet decomposition used to extract the features in [27, 28] generates a large number of wavelet coefficients, which increases the complexity of network training. This process of extracting signal features takes a lot of

time. Second, the NN in [29–31] used a single NN, which is hard to effectively learn the signal characteristics collected by the DAS. Besides, the existing experiments in [32–35] only utilized the data being generated very close to the sensed area (tens or hundreds of meters), which had a small sensing area or were at a location with a clean background environment. This makes it almost impossible to verify the recognition accuracy of the recognition model with dozens of kilometers' long distance and with unknown background noises. Thus, these systems are not able to fully meet the needs of the indicators, and soil signal processing is still not perfect. No article exists focusing on the role of the combination of soil environment and optical fiber sensing in the OFPS.

In this paper, we studied the signal acquisition problem of long-distance gas and oil pipeline prewarning system in real soil environment. Accordingly, an improved high-intelligence method was proposed for optimization. This method can solve the problem that the same vibration signal would vary greatly when collected in different soil environments, which would reduce the signal recognition accuracy of the prewarning system. This method is based on the real application environment, which has practical significance for industrial applications. The improved high-intelligence method is a new neural network method, which has the advantages of LSTM and CNN. LSTM is good at processing time-related data, and CNN can abstract and extract features from data at multiple time points to reduce invalid data. These advantages determine that the improved NN is more suitable for the recognition of optical fiber vibration signals than other traditional methods. It is a new attempt in the field of optical fiber prewarning. Through experiments, it is verified that this improved NN has good adaptability and real-time performance. We collected three types of event signals in different soil environments for training and recognition, and it is proved that the improved high-intelligence method has good adaptability, and the average recognition rate of three types of event signals is more than 95%. Since this method has good adaptability and real-time performance, it can be popularized in the optical fiber prewarning systems all over the world. Furthermore, the results of the study have high practical value for monitoring the safety of gas and oil pipelines.

## 2. Optical Fiber Prewarning System

The OTDR system uses a low-coherence light source, and the phase information of the light wave is masked. But the phase change caused by external disturbance is more sensitive. In order to take advantage of the high sensitivity of phase shift, a  $\Phi$ -OTDR system was developed. The structure of the  $\Phi$ -OTDR system is similar to that of the OTDR, but with a narrow linewidth laser light source, the interference phenomenon of the backward Rayleigh scattered light within the optical pulse width is enhanced, and the sensitivity of the system is greatly improved [36–38]. The OFPS based on the  $\Phi$ -OTDR principle includes two main parts of PRS and DAS. Figure 2 represents the OFPS processing flow. The DAS's main function is to gather soil vibration signals near the pipeline in real time for monitoring invasion events.

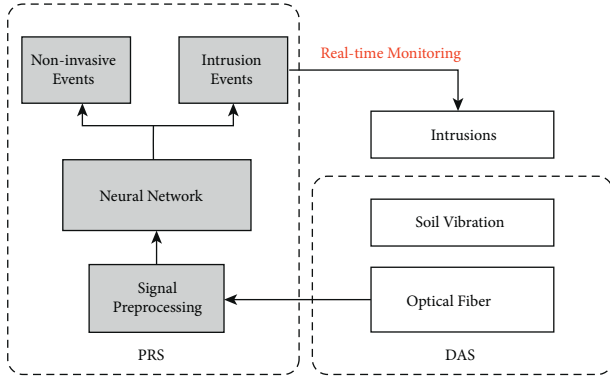


FIGURE 2: OFPS processing flow.

Within the DAS, a narrow line width laser source mainly emits the laser yielding the result of the interference of reflected Rayleigh scattered light. The events near the optical fiber can cause soil vibration signals. The pressure created by soil vibrations will act on the optical fiber sensing system, and then as a result of the photoelastic effect of the fiber, the refractive index of the fiber at the corresponding position will also alter. Subsequently, it will change the phase of light at the same point. Owing to the interference, the intensity of the backward Rayleigh scattered light will change with the phase. Therefore, when an intrusion event happens near the prewarning system, the intruding position intensity on the fiber varies from that before occurrence of the intrusion event, but the intensity at other positions remains unchanged. Vibration signals are collected by the DAS, and then they will be input into the PRS. The PRS is able to give the location and the type of the intrusion event.

Figure 3 shows the structure of the DAS utilized in this paper. A narrow line width laser is used in the DAS system as the light source to output continuous light with a wavelength of 1550 nm. In order to modulate the emitted light, the acousto-optic modulator is used to obtain a laser pulse, which is then amplified by an EDFA. The system utilizes two-way pumping Raman amplification to enhance system performance and amplify signal light at different locations in the fiber. A Raman laser is used by the amplifying part of the system as the pump source. The center wavelength of the pump source is 1450 nm with the maximum output power of 0.5 W. Through a 3 dB coupler and a wavelength division multiplexer (WDM), the amplified light pulse enters the sensing fiber. The sensing fiber is the common single-mode communication fiber. The amplified optical signal is filtered into the fiber grating (FBG) through the optical circulator, and the noise resultant from amplification was removed. Then, the intrusion signal is collected by the photodetector. Ultimately, the collected data is passed to the PRS for calculation and analysis.

### 3. Theoretical Analysis

**3.1. Soil Vibration.** Soil is a three-phase discontinuous material since the air, liquid, and soil particles are three different materials. The skeleton of soil is composed of loose soil particles, and each soil particle is filled with space between which the air and liquid exist. However, these three

media are not closely connected. Thus, when we analyze the indicators of soil physical properties, soil can be regarded as a discontinuous dispersion system [39].

Figure 4 shows the structure of the soil. As shown in the figure the structure is divided into air, water, and soil particles from top to bottom.  $m_a$  and  $V_a$  represent the mass and volume of the air;  $m_w$  and  $V_w$  represent the mass and volume of the liquid;  $m_s$  and  $V_s$  represent the mass and volume of soil particles. The total mass and volume of soil are expressed by  $m$  and  $V$ , respectively. Since the air has a mass of 0, the total mass of the soil is equal to the sum of the mass of liquid and the mass of soil particles; the volume of soil interstitial  $V_v$  can be regarded as the sum of the volume of liquid and the volume of air. The nature of the geotechnical soil is determined by these parameters. Thus, the forces on the skeleton of soil are different from the forces on the fluid. The forces on the soil skeleton can cause the deformation of both the soil itself and the fluid within the soil. In addition, according to different physical states, the density of medium can be divided into solid density and fluid density.

When the movement of soil particles, liquid, and air in the soil is not synchronized, the viscous force between them also weakens the elasticity of vibration. The range of action of vibration impact force on the cable is wide in the working process of the distributed optical fiber sensing system, and the effect of soil vibration signal is distributed in a section of fiber optic cable near the impact force. We used the theory of elastic half-space in our study. In this theory of elastic, there are three different types of waves including Primary Wave (P wave), Secondary Wave (S wave), and another elastic wave, Rayleigh wave (R wave). The vibration wave generated by the earth's surface is transmitted in the form of the R wave.

In the elastic half-space model, Poisson's ratio of foundation soil  $\mu$  and the modulus of rigidity  $G$  can be written as

$$\mu = \frac{v_p^2 - 2v_s^2}{2(v_p^2 - v_s^2)}, \quad (1)$$

$$G = \rho v_s^2,$$

where  $v_s$  and  $v_p$  represent wave velocity of S wave and P wave in elastic half-space theory, respectively. Poisson's ratio and shear modulus of soil are affected by the change of wave velocity. Under the vertical harmonic force of vibration source, at each point  $A_1$ , the soil vibration signal amplitudes can be expressed as

$$A_1 = \frac{F}{4\pi G} \left[ \frac{2(1-\mu)}{\sqrt{x^2 + Z^2}} + \frac{Z^2}{(x^2 + Z^2)^{3/2}} \right], \quad (2)$$

where  $F$  shows the concentrated vertical harmonic force,  $Z$  is the buried depth of fiber, and  $x$  represents the abscissa of any point on the fiber.

**3.2. Influence of Different Soil Types.** When the soil types are different, the basic parameters of the soil will also alter in the same season in a certain area. Table 1 represents the



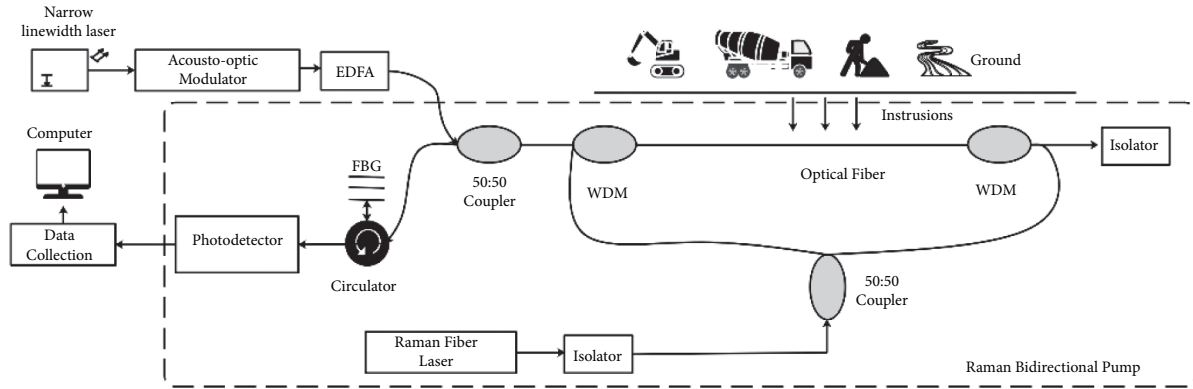


FIGURE 3: The DAS signal acquisition system.

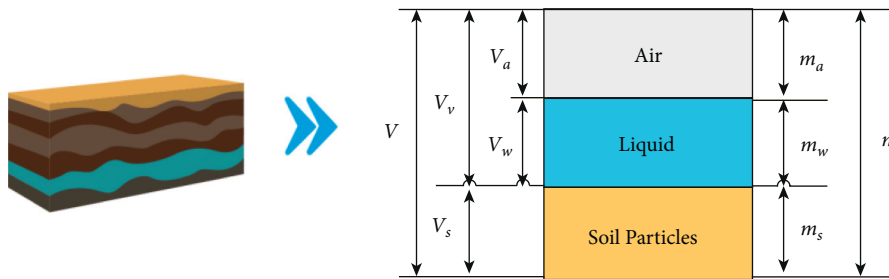


FIGURE 4: The structure of soil.

TABLE 1: The empirical values of two physical parameters of different soil types.

Physical parameters	Gravel soil	Sand	Cohesive soil	Sand clay
$G$	54–65	31–42	16–59	18–39
$\mu$	0.20	0.20–0.25	0.25–0.35	0.25–0.3

empirical values of two physical parameters of several common soil types in Shanghai city of China. The two physical parameters are very essential as the necessary dynamic parameter in the analysis of soil seismic response and an indispensable content in site vibration evaluation.  $\mu$  presents Poisson's ratio of foundation soil, and  $G$  denotes the modulus of rigidity.

According to Table 1, when the buried soil is different, Poisson's ratio of the soil is mainly within the range of 0.20–0.35, with little change. This parameter has little effect. However, the modulus of rigidity varies extensively. This will cause alterations in the soil vibration signal and affect the recognition accuracy of the OFPS. The vibration amplitude of the vibration signal of the soil is simulated by using equation (2), and the experimental parameters are shown in Table 2.

Figure 5 represents the mathematical relationship between the modulus of rigidity and the vibration amplitude of the soil vibration signal. It shows that the vibration amplitude of the soil's vibration signal gradually decreases by increasing the modulus of rigidity.

**3.3. Analysis of Real Signals.** Real soil vibration signals under different soil conditions were collected and analyzed. The distributed optical fiber sensing system used in the experiment is 22 km in Shanghai, with a buried depth of 1.2 m. The 22 km optical fiber is 12-core armored optical cable, which is directly buried under the surface without any packaging. The response time is 60 s or less, and the sampling frequency of the system is 750 Hz. We utilized a small tamping machine in the same gear to generate vibration signals and collected soil vibration signals from different sensor locations at the same temperature. The signals collected here are mechanical vibration signals. The soil types at the locations where the signals are collected are gravel soil, sandy soil, and clay with high moisture content. Figure 6 shows the signals of mechanical vibration under three certain conditions.

By comparison, the same vibration signal is changed after collecting by the OFPS in the case of different soil types, and the time-domain characteristics of some signals are quite different compared to others, such as the signals in clay with high moisture. By analyzing the collected soil vibration signals, the system gives the event recognition probability without the NN method. The specific information is shown in Table 3. According to Table 3, the system's recognition probability of event occurrence varies greatly under different soil types before the improved neural network method is used. And the recognition probability is less than 85% and the recognition effect of the system is relatively poor.

TABLE 2: The numerical value of the simulation parameter.

Force on the fiber optic cable $F$ (kN)	Horizontal coordinates of fiber optic cable $x$ (m)	Buried depth of fiber optic cable $Z$ (m)	Poisson's ratio $\mu$
1	1	0.5	0.25

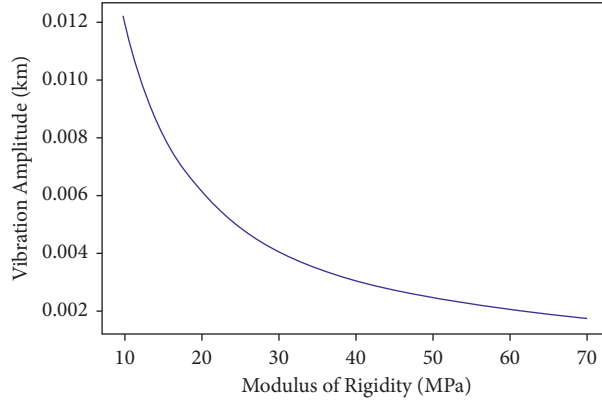


FIGURE 5: The relationship of vibration amplitude of soil vibration signal with the modulus of rigidity.

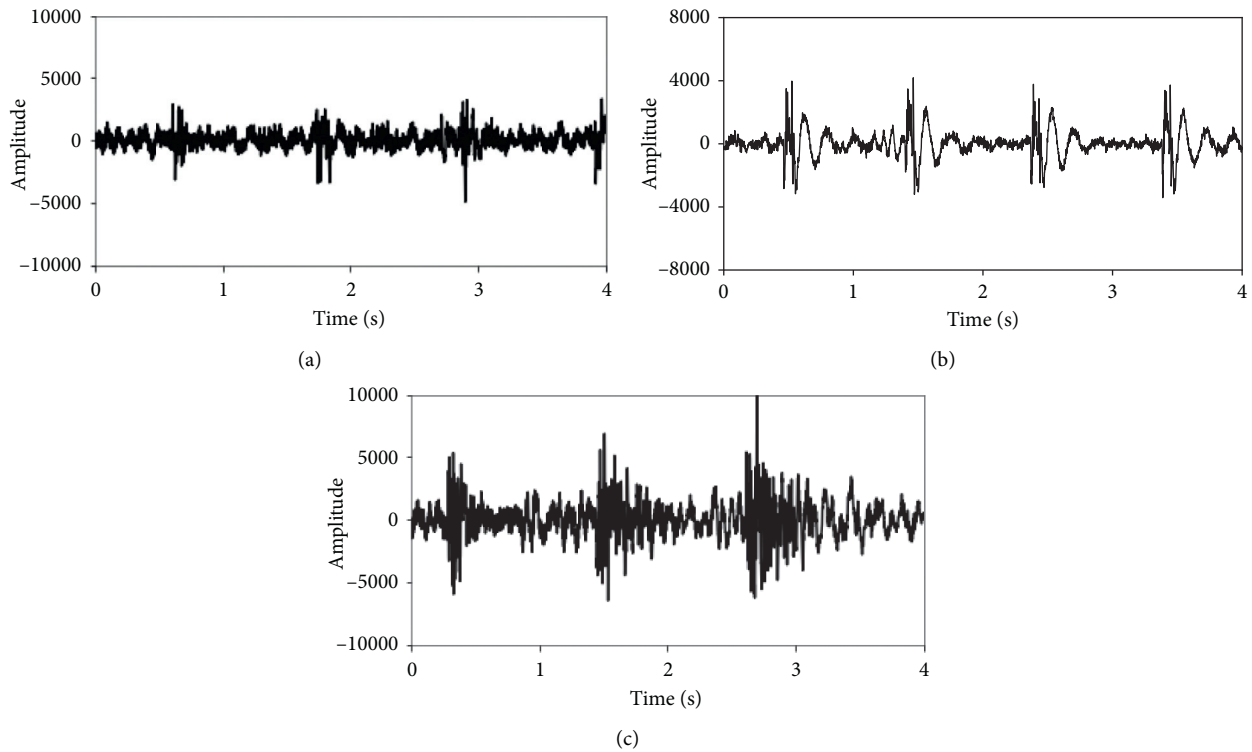


FIGURE 6: The signals under different conditions: (a) gravel soil, (b) sandy soil, and (c) clay with a high moisture.

### 4. Signal Recognition Methods

4.1. *Improved Neural Network (Method 1)*. An improved NN method is proposed to solve the above problem in this paper. The architecture of the neural network mainly integrates the advantages of the network such as Convolutional Neural Networks (CNN) and Long Short-Term Memory (LSTM) in

modeling, which can obtain the characteristic information of the signal data more effectively [40, 41].

First, the intrusion signals gathered by the system are labeled and standardized. Standardization of data refers to scaling the data to fall into a small specific interval. To ensure the reliability of the results, it is essential to standardize the data and utilize the standardized data for analysis before



TABLE 3: The event recognition probability under different soil types.

Type of soil	Number of experimental signals	Recognition probability (%)
Gravel soil	500	84.2
Sandy soil	500	72.5
Clay	500	58.3

modeling the neural network. The Max Abs Scaler is the standardization technique explored in this study adjusting each feature within the range of  $[-1, 1]$ . It is divided by the maximum absolute value within each feature. The main mathematical basis is shown in

$$x' = \frac{x}{|\max|} \quad (3)$$

In the formula,  $x$  and  $x'$  are the signal matrix before and after normalization, and  $\max$  is the maximum value of a certain row or column of the signal matrix. Signal matrix is a kind of matrix whose element is soil vibration signal amplitude in each row. The elements are arranged by the same time interval. The specific situation depends on whether the normalization is the row compression mode or the column compression mode. This method has the characteristics of not destroying the data structure and not moving and gathering data, so it will not destroy any sparseness, and it is suitable for signals collected by optical fiber systems [42].

The standardized signals will be input into the improved NN for deep learning. The signals first are input into the CNNs. Through convolution, the CNNs effectively avoid the complex data reconstruction in signal feature extraction and classification. The special structure of weight sharing greatly reduces the parameters of the model and reduces the complexity. CNN mainly includes convolutional layer and pooling layer. The convolutional layer recognizes different shallow features of the input data by using multiple filters. The pooling layer is a filtering process. The pooling layer can reduce the connections between the convolutional layers, thereby reducing the computational burden and reducing the complexity of the operation. CNN can effectively reduce the frequency variation. LSTM can model the signal time series characteristics, connect CNN to reduce the signal frequency domain variation, and then insert the output results of CNN into several LSTM layers for time series modeling. Ultimately, the output results of LSTM are inserted into the fully connected layer for analysis, and the feature space will be mapped to the output layer. This layer is more easily categorized to create the feature representation that is more easily separated. Therefore, the recognition model established by this method has better recognition and classification characteristics than a single neural network. The illustrated neural network structure is mainly constructed by combining the features of the CNN network and the LSTM network comprising three CNN layers, one linear layer (dim red), one LSTM layer, and a fully connected layer in Figure 7(a). First, the intrusion signals gathered by the system are labeled and standardized. The Max Abs Scaler is the standardization technique explored in this study. The

time of each labeled signal is 4 seconds, and the frequency is 750 Hz. The signals first are input into the CNNs. There are three CNNs in this method in Figure 7(b). The CNN of each layer includes a frequency-time filter ( $1 \times 5$ ) and a maximum pooling layer of 2 and a step size of 2. Since the output size of CNN is the number of feature maps  $\times$  time  $\times$  frequency, the size is very large. Adding a linear layer can effectively reduce the parameters without loss of accuracy by following the CNN layer. In experiments, it is found that it is appropriate to reduce the dimensionality so that the linear layer has 256 outputs. After passing through the CNN layer, a linear layer with 256 outputs is used to construct the input of the LSTM layer. By modeling the frequency, the output is passed to the LSTM layer to model the signal's time series. The flow of LSTM is shown in Figure 7(c). The utilized LSTM layer included 64 units and 256 hidden units. Ultimately, the results of a fully connected layer are used as the output of the signal. With the abovementioned steps, the system can perform deep learning modeling simply on the collected intrusion signals to accelerate the creation of a neural network model. Then, the system is able to identify and classify the gathered intrusion signals through the model.

*4.2. Method for Comparison (Method 2).* In order to compare the effectiveness of Method 1, Method 2 is proposed. A 5-layer Deep Neural Network (DNN) is used (Figure 8) including one input layer, three hidden layers, and one output layer. For the three hidden layers, a hyperbolic tangent sigmoid function generally is selected as the activation function, in which five knots are set in the first hidden layer, four knots are set in the second hidden layer, and three knots are set in the three hidden layers based on an experimental parameters test. The output layer with a linear activation function consists of three knots.

## 5. Model Building and Recognition Test Analysis

*5.1. Model Building and Recognition Test Analysis.* In this section, the data collected in Shanghai was used to train the neural network model. First, the training sets and the test sets of the recognition model were prepared. We utilized signals from three different soil types to train and test the recognition accuracy of the neural network model. Then, the collected signals with time-domain characteristics were processed and labeled into 4 s sample data for each segment. The time-domain signals of labeled samples collected from three different soil types are shown in Figure 6.

The division ratio of the training sets and the test sets is 7:2. The specific experimental data is shown in Table 4. In total, there are 2100 sets of data for training including 700 sets of data collected from gravel soil at 2.99 km, 700 sets of data collected from sandy soil at 10.21 km, and 700 sets of data collected from clay with high moisture content at 18.86 km for training neural networks to get recognition model. After training the model for all data, the test sets are selected which are different from the training sets to test the recognition effect of the model. A total of 900 sets of new

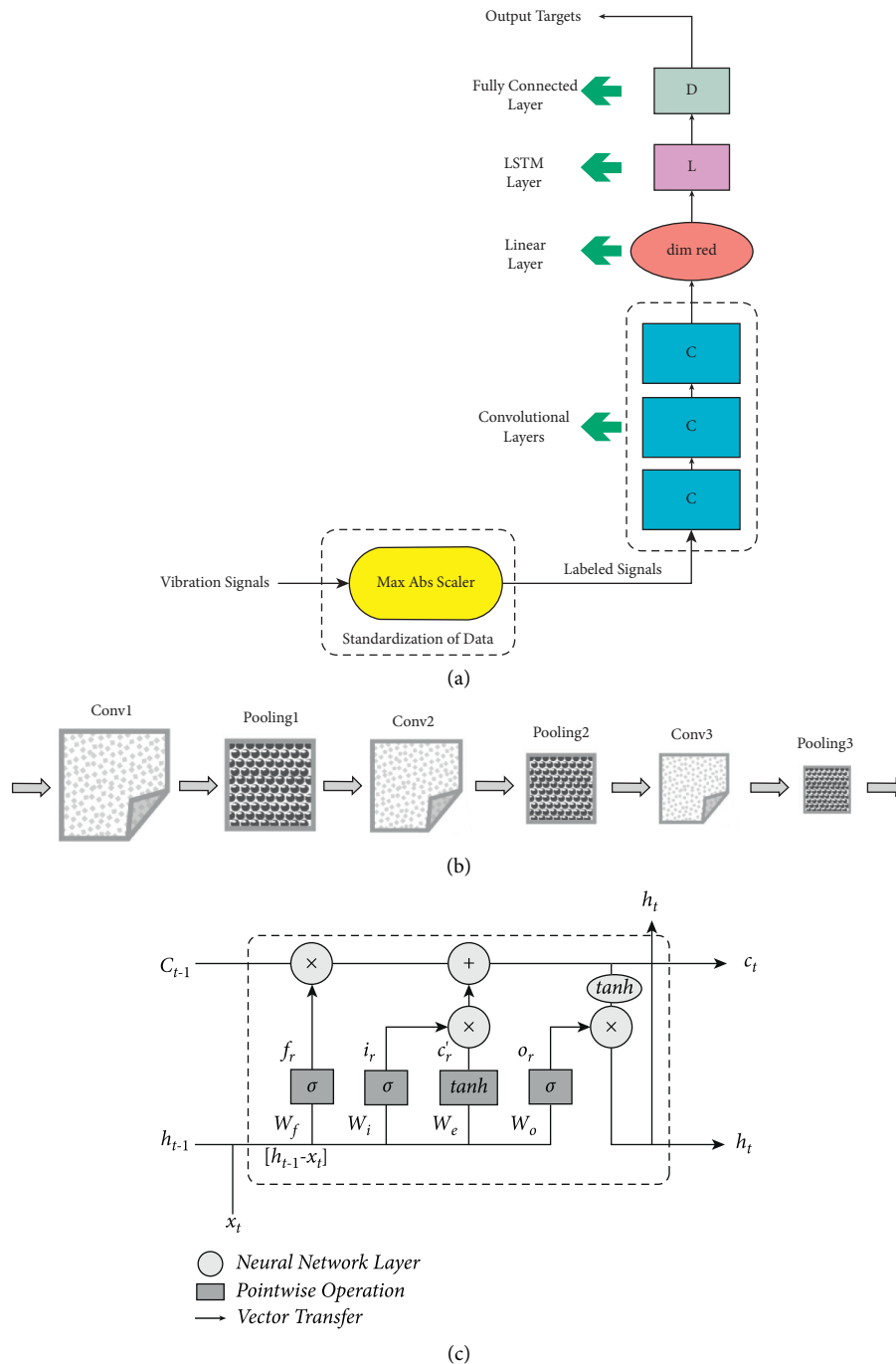


FIGURE 7: The improved neural network. (a) The flow of an improved neural network. (b) The convolutional layers. (c) The LSTM flow.

data are utilized as the test sets to test the recognition effect of the model including 300 sets from gravel soil, 300 sets from sandy soil, and 300 sets from clay.

When training, all training datasets are trained once for one epoch. The fitting degree of the neural network to the data is determined by the number of the epochs. Numerous epochs may cause overfitting of the data; otherwise, underfitting the data is caused. The number is determined by the validation accuracy of the neural network. Provided that the network self-test accuracy reaches over 99%, the training

can be stopped to avoid overfitting caused by excessive epoch. Figure 9 represents the relationship between epoch and validation accuracy used in the neural network in the first method indicating that when the epoch reaches 1183 times, validation accuracy meets the requirement. Training loss is also close to 0 based on Figure 9.

After training the model, the test sets are selected to examine the recognition effect of the model. According to Table 5, the signal recognition average accuracy of the OFPS obtained by Method 1 is 95.1%, and the recognition average

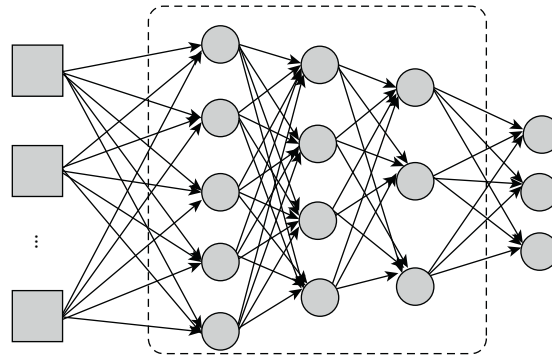


FIGURE 8: The 5-layer DNN network.

TABLE 4: The first experiment data.

Type of soil	Number of training sets	Collection location of training sets (km)	Number of test sets	Collection location of test sets (km)
Gravel soil	700	2.99	300	2.99
Sandy soil	700	10.21	300	10.21
Clay	700	18.68	300	18.68

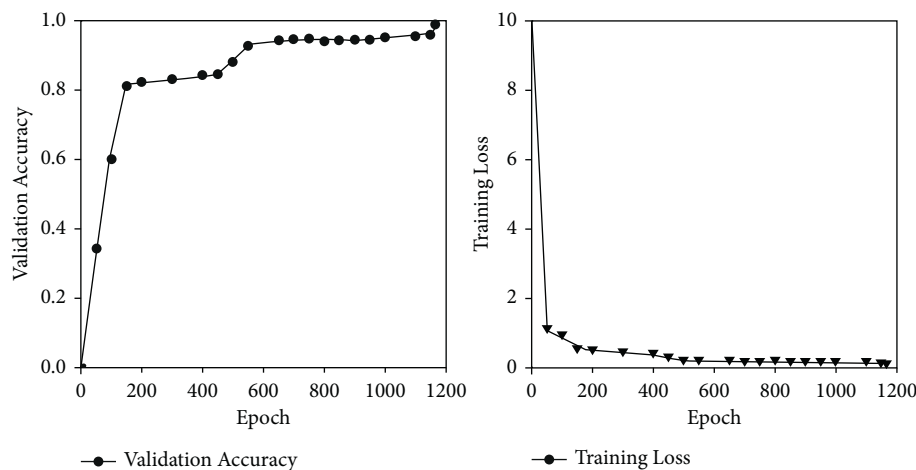


FIGURE 9: The relationship between epoch and validation accuracy and training loss.

TABLE 5: The signal recognition accuracy in the first experiment.

Type of soil	Method 1 (%)	Method 2 (%)
Gravel soil	96.5	91.6
Sandy soil	95.4	89.4
Clay	92.9	88.9
Average	95.1	89.8

accuracy of the OFPS obtained by Method 2 is 89.8%. Based on the comparison, it is observed that the testing effect of Method 1 is better and the recognition accuracy is over 95%.

**5.2. The Adaptability of the Method.** The adaptability of the method was studied by implementing the test and verifying of classification and identification effect of the optical fiber warning system in the actual environment. The adaptability

of the method referring to the data collected by the system in different regions has good recognition and classification capabilities. Thus, the signals of the three events were collected inducing manual digging (MG), mechanical excavation (ME), and noninvasion (NI) in different regions. The distributed optical fiber sensing system used in the experiment is 22 km in Shanghai, with a buried depth of 1.2 m. The response time is 60 s or less, and the sampling frequency of the system is 750 Hz. The signals of manual digging (MG) were obtained by digging the soil with a shovel. The signals of mechanical excavation (ME) were obtained by using a tamping machine to vigorously excavate the soil. Finally, we selected the places where no incident occurred to collect the signals of noninvasion (NI). This experiment is aimed to ensure the diversity and complexity of the collected data and to recognize the vibration signal at a remote location of the system. The vibration signal samples of three typical

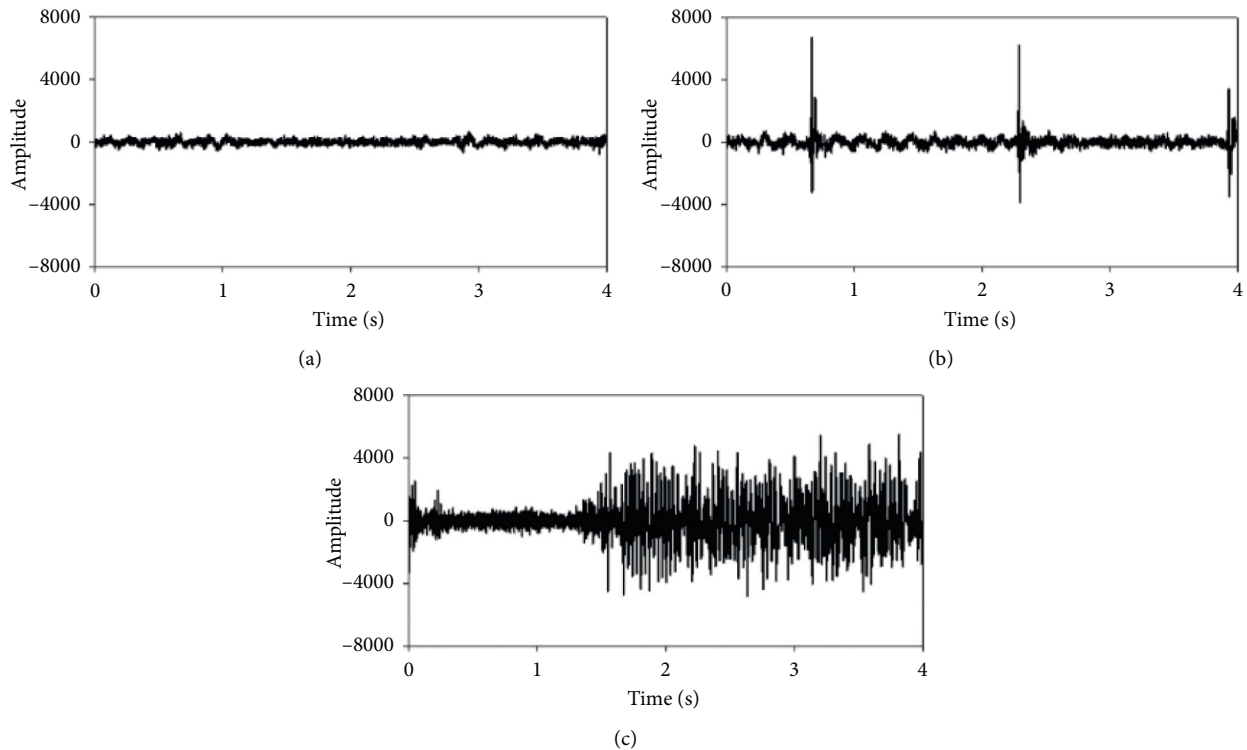


FIGURE 10: The signal samples. (a) The NI event. (b) The MG event. (c) The ME event.

intrusion events in this experiment are collected at different positions to guarantee the validity and authenticity of the sample set. Similarly, the collected signals with time-domain characteristics are also processed and labeled into 4 s sample data. As shown in Figure 10, they are the time-domain signals of labeled samples gathered.

The specific information of the input training and test sets of the neural network is shown in Table 6. In total, there are 16733 sets of data for training including 5528 sets of the NI events data, 5674 sets of the MG events data, and 5531 sets of the ME events data applicable for training neural networks to build recognition models.

The test results are provided in Table 7. In the second experiment, the signal recognition accuracy of the OFPS obtained by Method 1 is 95.6%, and the average accuracy obtained by Method 2 is 90.4%. By comparing the data in Table 7, it can be observed that the accuracy of Method 1 remained above 95% and this improved NN has good adaptability in the actual environment and can be popularized in long-distance OFPS.

**5.3. The Real-Time Capability of the Method.** Through the two experiments above, it can be seen that this new method can accurately classify signals, indicating that this improved NN is feasible. Therefore, we will run this identification part in real time in the pipeline prewarning system. Figure 11 shows the process of the pipeline prewarning system for real-time detection. The signal collection part of the pipeline prewarning system collects the data of each optical fiber sensor on the optical fiber every four seconds. When a

harmful intrusion event such as mechanical excavation occurs near the pipeline, it will cause the fiber optic sensor to respond. After the data is collected, it will be transmitted to the neural network for identification and classification, and the predicted probability of the occurrence of the intrusion event at that point will be given. The data used for model training of the neural network is collected in different soil environments, which will make the training set more complete. The data used for testing is the real-time data collected by the pipeline prewarning system every four seconds. This can better verify the real-time performance of the system.

To ensure the integrity of the analysis, the predictive ability of the system for the occurrence of interference events was compared between Method 1 and Method 2. The abscissa in the next two figures is the length of the whole optical fiber, and the ordinate is the probability of the predicted event. Figure 12 represents the recognition probability of each point on the whole fiber length when occurring in the manual mining event. The experimental data are the data collected on the whole optical fiber length during manual mining at 6.52 km. At this point, no other intrusions exist elsewhere on the fiber. It can be seen in Figure 12(a) that the system can estimate the manual mining events at 6.52 km with Method 2. However, the recognition rate is less than 80%, and there is a false alarm at other locations to a certain extent. After using the improved NN, it is observed (Figure 12(b)) that the recognition rate at 6.81 km exceeds 95%, and there is no false alarm at other locations. The overall recognition rate of the system model is enhanced.

TABLE 6: The second experiment data.

Type of event	Number of training sets	Collection location of training sets (km)	Number of test sets	Collection location of test sets (km)
NI	5528	2.99	2000	14.96
MG	5674	10.21	2000	16.86
ME	5531	18.68	2000	6.24

TABLE 7: The signal recognition accuracy in the second experiment.

Type of event	Method 1 (%)	Method 2 (%)
NI	97.5	93.6
MG	94.3	89.7
ME	95.2	88.3
Average accuracy	95.6	90.4

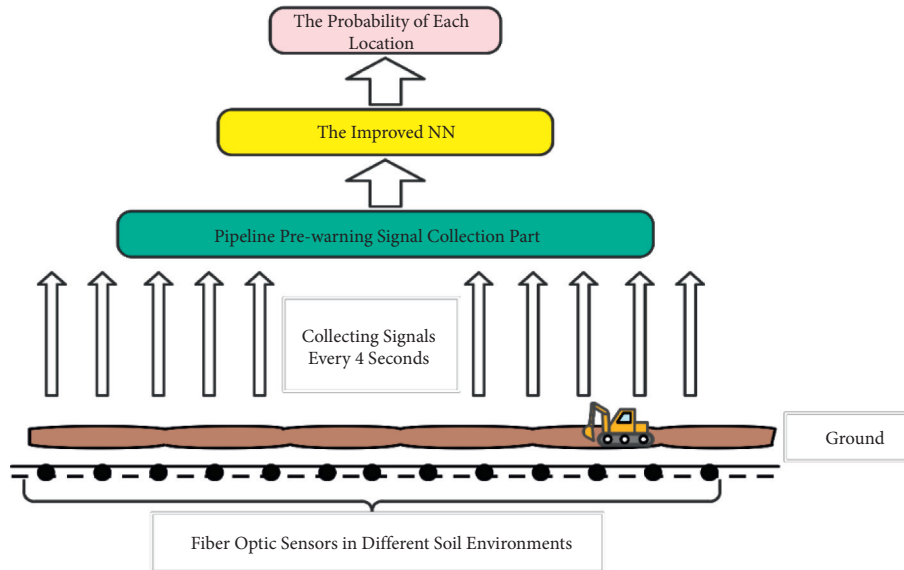


FIGURE 11: The process of the pipeline prewarning system for real-time detection.

Similarly, Figure 13 represents the recognition probability of each point on the whole fiber length when occurring in the mechanical mining event. The experimental data are the data collected on the whole fiber length during mechanical excavation at 5.57 km. No other intrusions exist at any other point along the length of the fiber. Considering the large intensity and wide influence range of mechanical excavation events, it is observed that the occurrence of events is predicted within a range of about 5.57 km. The comparison of the two figures shows that, before using the improved NN, the recognition rate of the system for mechanical excavation was also about 80%, and the false alarm was reported at other locations. After analyzing the data via the improved NN, it is observed that the recognition rate of the event exceeds 95%, and no events occur in other locations. This is consistent with the actual situation.

According to Sections 5.2 and 5.3, the improved NN has better adaptability and real-time capability. The reason why

the improved NN method works is as follows: LSTM is good at processing time-related data; CNN can abstract and extract features from data at multiple time points to reduce invalid data. CNN has the ability to process time information, and the ability of this abstract feature of CNN is higher than that of LSTM. The CNN layer can extract hidden information in the time dimension and then pass higher-quality and high-concentration features to the LSTM layer. These characteristics determine that the improved NN is more suitable for the recognition of optical fiber vibration signals than Method 2 and other methods. However, this method also has some disadvantages. First, this improved NN has only been tested in the field of fiber vibration signal recognition and has not been tried in other speech signal recognition. Besides, this method requires relatively high GPU performance, so a high-performance GPU is required for calculation. Since the optical fiber early warning system requires real-time detection, a high-performance computer is also necessary.

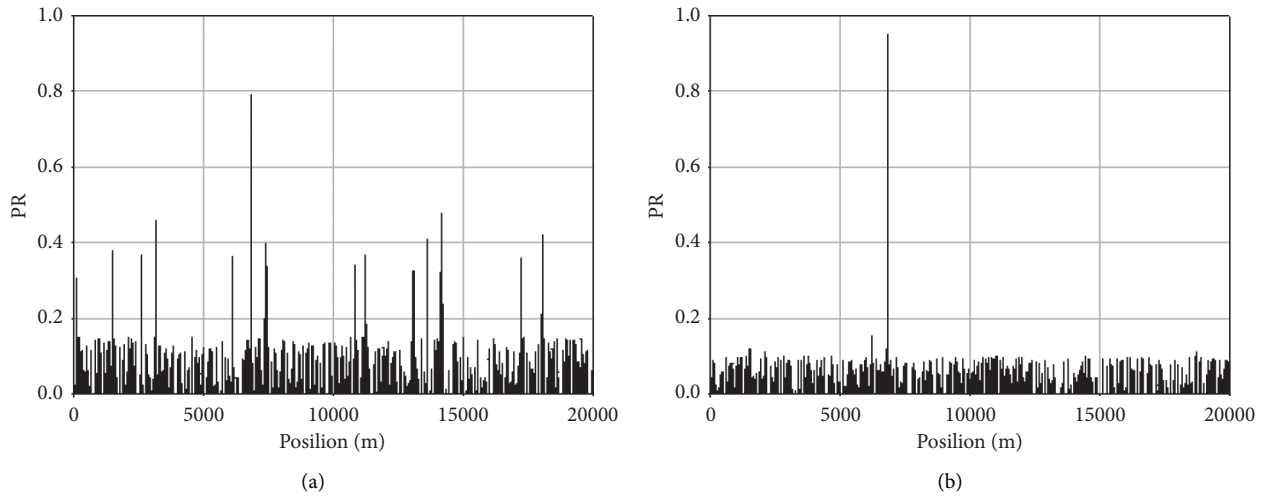


FIGURE 12: The comparison of occurrence probability of manual mining events. (a) Before using the improved neural (Method 2); (b) after using the improved neural network (Method 1).

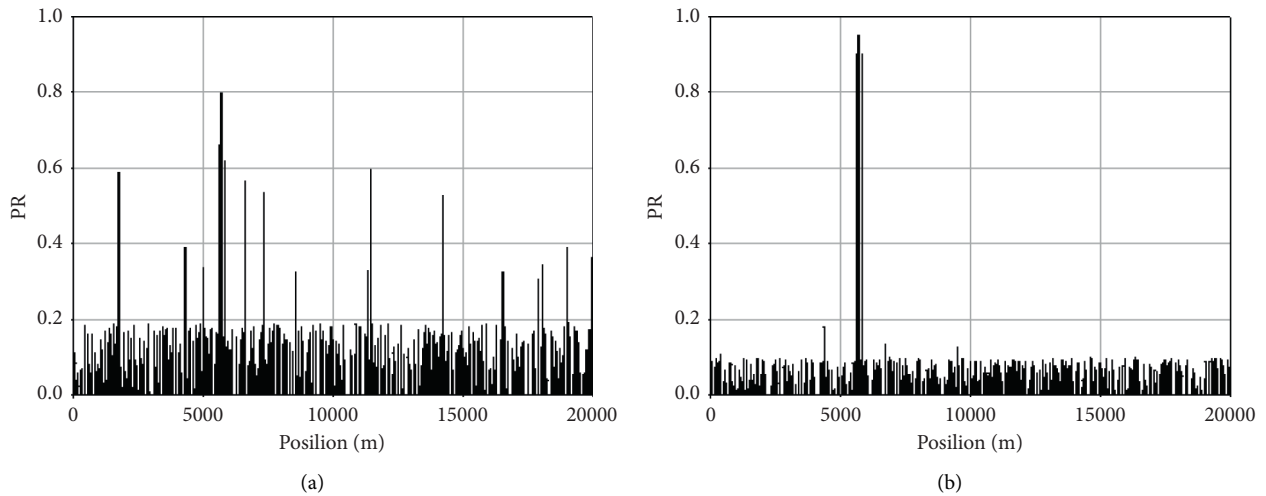


FIGURE 13: The comparison of occurrence probability of mechanical excavation events. (a) Before using the improved neural network (Method 2); (b) after using the improved neural network (Method 1).

## 6. Conclusion

In this paper, we found that the same vibration signals would vary greatly when collected in different soil environments and this problem would reduce the signal recognition accuracy of the OFPS. This phenomenon was theoretically studied, and soil vibration signals under different soil conditions were collected and analyzed. A novel highly intelligent method was proposed to improve signal acquisition of gas and oil pipeline prewarning system in the complex soil environment. First, we analyzed the effects of the real soil environment. The two principles of elastic half-space theory and optical fiber sensing theory were creatively integrated. The results indicate that this problem will affect the recognition rate of the OFPS. Therefore, we utilized an improved NN based on LSTM and CNN which is mainly attempted in the field of optical fiber signal recognition.

Based on the investigation, some remarkable conclusions can be drawn as follows:

- (1) The improved high-intelligence method is a new neural network method, which has the advantages of LSTM and CNN. LSTM is good at processing time-related data, and CNN can abstract and extract features from data at multiple time points to reduce invalid data. These advantages determine that the improved NN is more suitable for the recognition of optical fiber vibration signals than other traditional methods. It is a new attempt in the field of optical fiber prewarning. Through experiments, it is verified that this improved NN has good adaptability and real-time performance.
- (2) We collected three types of event signals in different soil environments for training and recognition, and

it is proved that the improved high-intelligence method has good adaptability, and the average recognition rate of three types of event signals is more than 95%.

- (3) This improved method was used to conduct real-time online monitoring of the pipeline prewarning system in Shanghai. Through the experiments of two types of intrusion events, it is proved that the method has good real-time performance and can quickly give the location and the probability of the event, and the prediction rate of the event has reached about 95%.

Since this method has good adaptability and real-time performance, it can be popularized in the optical fiber prewarning systems all over the world, which is helpful to maintain the safety of gas and oil pipelines and has far-reaching significance for the intelligence of gas and oil transportation systems. Furthermore, the results of the study have high practical value for monitoring the safety of gas and oil pipelines.

## Data Availability

The data used to support the findings of this study are available from the corresponding author upon request.

## Conflicts of Interest

The authors declare that there are no conflicts of interest regarding the publication of this study.

## Acknowledgments

The authors gratefully acknowledge the support given by HILONG Group of Companies. This work was supported by Shanghai Municipal Economic and Informatization Commission (Grant no. 2018-RGZN-02015).

## References

- [1] R. Cramer, D. Shaw, R. Tulalian, P. Angelo, and M. van Stuijvenberg, "Detecting and correcting pipeline leaks before they become a big problem," *Marine Technology Society Journal*, vol. 49, no. 1, pp. 31–46, 2015.
- [2] Y. J. Rao, J. Luo, and Z. L. Ran, "Long-distance fiber-optic  $\Phi$ -OTDR intrusion sensing system," *SPIE*, vol. 7503, pp. 1–4, 2009.
- [3] W. T. Lin, S. Q. Lou, and S. Liang, "Fiber-optic distributed vibration sensor for pipeline pre-alarm," *Applied Mechanics and Materials*, vol. 684, pp. 235–239, 2014.
- [4] N. D. Faber, "Costs and benefits for pipeline acoustic fiber optic monitoring," in *Pipelines 2017*, pp. 12–22, American Society of Civil Engineers, Reston, VA, USA, 2017.
- [5] J. M. López-Higuera, L. Rodríguez Cobo, A. Quintela Incera, and A. Cobo, "Fiber optic sensors in structural health monitoring," *Journal of Lightwave Technology*, vol. 29, no. 4, pp. 587–608, 2011.
- [6] J. C. Juarez, E. W. Maier, K. N. Kyoo Nam Choi, and H. F. Taylor, "Distributed fiber-optic intrusion sensor system," *Journal of Lightwave Technology*, vol. 23, no. 6, pp. 2081–2087, 2005.
- [7] L. Ren, T. Jiang, Z.-g. Jia, D.-s. Li, C.-l. Yuan, and H.-n. Li, "Pipeline corrosion and leakage monitoring based on the distributed optical fiber sensing technology," *Measurement*, vol. 122, pp. 57–65, 2018.
- [8] Q. Chai, Y. Luo, and Ren, "Review on fiber-optic sensing in health monitoring of power grids," *Optical Engineering*, vol. 58, no. 7, Article ID 072007, 2019.
- [9] X. Zhang, Z. Guo, Y. Shan, Z. Sun, S. Fu, and Y. Zhang, "Enhanced  $\Phi$  - OTDR system for quantitative strain measurement based on ultra-weak fiber Bragg grating array," *Optical Engineering*, vol. 55, no. 5, Article ID 054103, 2016.
- [10] L. Lv, F. Pang, and H. Liu, "50-km-long distributed vibration fiber sensor based on phase-sensitive otdr using coherent detection," in *Proceedings of the Conference on Lasers and Electro-Optics/Pacific Rim*, p. s1234, August 2017.
- [11] İ. Ölçer and A. Öncü, "A novel data adaptive detection scheme for distributed fiber optic acoustic sensing," *Fiber Optic Sensors and Applications XIII*, International Society for Optics and Photonics, vol. 9852Bellingham, WA, USA, , 2016.
- [12] J. Tejedor, J. Macias-Guarasa, H. Martins et al., "A novel fiber optic based surveillance system for prevention of pipeline integrity threats," *Sensors*, vol. 17, no. 2, p. 355, 2017.
- [13] D. Inaudi and B. Glisic, "Long-range pipeline monitoring by distributed fiber optic sensing," *Journal of Pressure Vessel Technology*, vol. 132, p. 1, 2010.
- [14] C. Xu, J. Guan, M. Bao, J. Lu, and W. Ye, "Pattern recognition based on time-frequency analysis and convolutional neural networks for vibrational events in  $\phi$ -OTDR," *Optical Engineering*, vol. 57, no. 1, Article ID 016103, 2018.
- [15] Y. Wang, B. Jin, and Y. Wang, "Real-time distributed vibration monitoring system using Phi-OTDR," *IEEE Sensors Journal*, vol. 17, no. 5, pp. 1333–1341, 2016.
- [16] Q. Wang, S. He, and W. Dang, "Study on performance evaluation of safety pre-warning technology on oil and gas pipeline," *Journal of Safety Science and Technology*, vol. 9, no. 1, pp. 98–102, 2013.
- [17] P. Chen, Y. Cai, and J. Li, "Study on modified Mach-Zehnder interferometer based on pipeline security and pre-warning system," *Chinese Journal of Sensors and Actuators*, vol. 22, no. 11, pp. 1661–1664, 2009.
- [18] L. Lin, W. Chen, and P. Zhang, "Distributed optic fiber sensor with a sub-ring," *Acta Photonica Sinica*, vol. 38, no. 5, pp. 1118–1121, 2009.
- [19] Y. Ma, Z. Hu, and J. Yang, "Oil pipeline security monitoring system based on fiber Bragg grating sensor," *Journal of Applied Optics*, vol. 30, no. 3, pp. 505–509, 2009.
- [20] Y. Muanenda, "Recent advances in distributed acoustic sensing based on phase-sensitive optical time domain reflectometry," *Journal of Sensors*, vol. 2018, Article ID 3897873, 16 pages, 2018.
- [21] H. He, L. Shao, H. Li et al., "SNR enhancement in phase-sensitive OTDR with adaptive 2-D bilateral filtering algorithm," *IEEE Photonics Journal*, vol. 9, no. 3, pp. 1–10, 2017.
- [22] Z. Qin, H. Chen, and J. Chang, "Signal-to-noise ratio enhancement based on empirical mode decomposition in phase-sensitive optical time domain reflectometry systems," *Sensors*, vol. 17, no. 8, p. 1870, 2017.
- [23] Y. Muanenda, C. J. Oton, S. Faralli, and F. Di Pasquale, "A cost-effective distributed acoustic sensor using a commercial off-the-shelf DFB laser and direct detection phase-OTDR," *IEEE Photonics Journal*, vol. 8, no. 1, pp. 1–10, 2015.
- [24] B. Lu, Z. Pan, Z. Wang et al., "High spatial resolution phase-sensitive optical time domain reflectometer with a frequency-swept pulse," *Optics letters*, vol. 42, no. 3, pp. 391–394, 2017.

- [25] J. Pastor-Graells, L. R. Cortés, M. R. Fernández-Ruiz et al., “SNR enhancement in high-resolution phase-sensitive OTDR systems using chirped pulse amplification concepts,” *Optics Letters*, vol. 42, no. 9, pp. 1728–1731, 2017.
- [26] W. Deng, J. Xu, and H. Zhao, “A novel gate resource allocation method using improved PSO-based QEA,” *IEEE Transactions on Intelligent Transportation Systems*, no. 99, 2020.
- [27] H. Wu, Y. Qian, W. Zhang, and C. Tang, “Feature extraction and identification in distributed optical-fiber vibration sensing system for oil pipeline safety monitoring,” *Photonic Sensors*, vol. 7, no. 4, pp. 305–310, 2017.
- [28] G. Wang, X. Li, and Y. Li, “The application of wavelet transform in the fiber pipeline safety pre-warning system,” in *Proceedings of the 27th Chinese Control and Decision Conference (2015 CCDC)*, pp. 3605–3608, IEEE, Qingdao, China, May 2015.
- [29] J. Tejedor, J. Macias-Guarasa, H. Martins, J. Pastor-Graells, P. Corredera, and S. Martin-Lopez, “Machine learning methods for pipeline surveillance systems based on distributed acoustic sensing: a review,” *Applied Sciences*, vol. 7, no. 8, p. 841, 2017.
- [30] Q. Tian, C. Zhao, Y. Zhang, and H. Qu, “Intrusion signal recognition in OFPS under multi-level wavelet decomposition based on RVFL neural network,” *Optik*, vol. 146, pp. 38–50, 2017.
- [31] Y. Wang, D. Gong, L. Pang, and D. Yang, “RVFL-based optical fiber intrusion signal recognition with multi-level wavelet decomposition as feature,” *Photonic Sensors*, vol. 8, no. 3, pp. 234–241, 2018.
- [32] J. Tejedor, H. F. Martins, D. Piote et al., “Toward prevention of pipeline integrity threats using a smart fiber-optic surveillance system,” *Journal of Lightwave Technology*, vol. 34, no. 19, pp. 4445–4453, 2016.
- [33] Q. Tian, D. Yang, Y. Zhang, and H. Qu, “Detection and recognition of mechanical, digging and vehicle signals in the optical fiber pre-warning system,” *Optics Communications*, vol. 412, pp. 191–200, 2018.
- [34] J. Tejedor, C. H. Ahlen, M. Gonzalez-Herraez et al., “Real field deployment of a smart fiber-optic surveillance system for pipeline integrity threat detection: architectural issues and blind field test results,” *Journal of Lightwave Technology*, vol. 36, no. 4, pp. 1052–1062, 2018.
- [35] J. Tejedor, J. Macías-Guarasa, and H. F. Martins, “Towards detection of pipeline integrity threats using a Smart fiber-Optic surveillance system: PIT-STOP project blind field test results,” in *Proceedings of the 2017 25th Optical Fiber Sensors Conference (OFS)*, pp. 1–4, IEEE, Jeju, Korea, April 2017.
- [36] A. Masoudi, M. Belal, and T. P. Newson, “A distributed optical fibre dynamic strain sensor based on phase-OTDR,” *Measurement Science and Technology*, vol. 24, no. 8, Article ID 085204, 2013.
- [37] Y. Lu, T. Zhu, L. Chen, and X. Bao, “Distributed vibration sensor based on coherent detection of phase-OTDR,” *Journal of Lightwave Technology*, vol. 28, no. 22, pp. 3243–3249, 2010.
- [38] L. Zhou, F. Wang, X. i. Wang et al., “Distributed strain and vibration sensing system based on phase-sensitive OTDR,” *IEEE Photonics Technology Letters*, vol. 27, no. 17, pp. 1884–1887, 2015.
- [39] K. W. Winkler and A. Nur, “Seismic attenuation: effects of pore fluids and frictional-sliding,” *Geophysics*, vol. 47, no. 1, pp. 1–15, 1982.
- [40] H. Sak, A. Senior, and F. Beaufays, “Long short-term memory based recurrent neural network architectures for large vocabulary speech recognition,” 2014, <https://arxiv.org/abs/1402.1128>.
- [41] T. N. Sainath, O. Vinyals, A. Senior, and H. Sak, “Convolutional, long short-term memory, fully connected deep neural networks,” in *Proceedings of the 2015 IEEE International Conference on Acoustics, Speech and Signal Processing (ICASSP)*, pp. 4580–4584, IEEE, South Brisbane, Australia, April 2015.
- [42] J. Mistry and B. Inden, “An approach to sign language translation using the intel realsense camera,” in *Proceedings of the 2018 10th Computer Science and Electronic Engineering (CEECS)*, pp. 219–224, IEEE, Colchester, UK, September 2018.



## Research Article

# An FBG Strain Sensor-Based NPW Method for Natural Gas Pipeline Leakage Detection

Qingmin Hou 

*School of Energy and Building Engineering, Harbin University of Commerce, Harbin 150028, China*

Correspondence should be addressed to Qingmin Hou; [sspawm@163.com](mailto:sspawm@163.com)

Received 8 January 2021; Revised 18 February 2021; Accepted 10 March 2021; Published 15 March 2021

Academic Editor: Haoran Zhang

Copyright © 2021 Qingmin Hou. This is an open access article distributed under the Creative Commons Attribution License, which permits unrestricted use, distribution, and reproduction in any medium, provided the original work is properly cited.

Natural gas pipeline leaks can lead to serious and dangerous accidents that can cause great losses of life and property. Therefore, detecting natural gas pipeline leaks has always been an important subject. The negative pressure wave (NPW) method is currently the most widely used leakage detection method. Generally, this method uses pressure sensors to detect NPW signals to assess the leak and determine the location of the leakage point. However, the installation of a pressure sensor requires penetrating the pipeline structure, so the sensor intervals are often distant, leading to large signal attenuations and the ineffective detection of small leaks. An NPW method based on fiber Bragg grating (FBG) strain sensors is proposed in this paper which detects NPWs by monitoring the annular strain of the pipeline. Moreover, due to the advantages of nondestructive installation FBG strain sensors can be arranged closer along the distance of the pipeline, the attenuation of the NPW is small and the detection of leaks is improved. This method is tested through experiments and compared with a pressure sensor-based method; the experimental results verify that the proposed method is more effective in detecting natural gas pipeline leaks.

## 1. Introduction

Natural gas pipelines are the preferred method of natural gas transmission. However, as gas is a hazardous material, a leaking or broken gas pipeline can cause great harm to the surrounding environment and personnel. When a gas pipeline leaks, especially a high-pressure gas pipeline compressed gas will expand rapidly and release a large amount of energy causing explosions and fires that can lead to considerable economic losses and casualties.

The service life of pipelines is similar to the lifespan of human beings which can be roughly divided into three stages: infancy (1~5 years old) adulthood (6~20 years old), and old age (over 20 years old). Correspondingly, the service process of pipelines can also be divided into these three stages. When the pipeline is in its infancy, the probability of accidents, especially leakage, is very low. When the pipeline is in middle age, the accident rates are relatively stable and can be kept at a low level. When the pipeline is old, the accident rates are higher and tend to increase over time.

There are many methods in use for gas pipeline leak detection but the principles and technical means of each method are different [1–7]. The pressure sensor-based negative pressure wave (NPW) method is widely used in this field because it can avoid the establishment of a complex mathematical model for the pipelines and is easy to operate [8]. This method is effective for the detection of sudden leaks but not for small leaks that occur slowly. This method is easily disturbed by external factors and it exhibits a high failure rate.

Detection technology based on distributed fiber sensors is widely used at present to detect pipeline leaks [9–20]. In this method, a fiber is arranged along the pipeline to determine whether the pipeline is leaking and to locate the leaking position by detecting the vibration or temperature change caused by the leak. However, due to the complex external environment of buried pipelines, they may cross urban areas, rivers, and so on. Many external factors may also lead to vibration or temperature changes such as rolling vehicles, random optical fiber vibrations, and climate change. Therefore, this method is prone to

interference has a high false alarm rate and can only determine an abnormal condition in a pipeline. At present, there are few applications of quasi-distributed optical fiber Bragg grating (FBG) used in the detection of natural gas pipeline leaks [21–25]. Lopez et al. developed an FBG sensor based on an expandable polymer that can expand when it encounters oil and thus produces strain [26]. However, because the main component of natural gas is methane which has stable chemical properties that hinder the expansion of a polymer, this sensor is not suitable for the detection of natural gas pipeline leaks.

In this paper, an idea is proposed. An NPW generated by a natural gas pipeline leak will cause a pressure variation in the pipeline; this pressure variation will create an annular strain in the pipeline and the pipeline leak can be detected by monitoring the annular strain of the pipeline through an FBG strain sensor. Based on the abovementioned principles, an FBG strain sensor-based NPW method for natural gas pipeline leak detection is proposed and this method is tested and compared with an experiment.

## 2. Pressure Sensor-Based NPW Method

Based on the theory of fluid mechanics, it can be seen that the pressure in a natural gas pipeline tends to be stable overall although there are some small fluctuations before the leak. When a pipeline leak occurs due to the pressure difference between the inside and outside of the pipeline, the fluid at the leak point will escape rapidly and the fluid density at the leak point will decrease, resulting in an instantaneous pressure drop. This instantaneous pressure drop propagates as a wave up and down the leak point. If the pressure inside the pipe under normal conditions is taken as the reference standard, the pressure wave generated by the leak is an NPW. With the generation and propagation of the disturbance, the NPW will reduce the pressure along the pipeline.

*2.1. Principle of Pressure Sensor-Based NPW Method.* To incorporate the pressure sensor-based NPW method, pressure sensors are installed upstream and downstream to collect NPW signals to detect leaks. According to the time difference for the detected signals and the propagation velocity in the medium, the exact position of the leak point can be calculated. The principle of the pressure sensor-based NPW method is illustrated in Figure 1.

In Figure 1, the distance between two pressure sensors is  $L$ , the propagation velocity of the NPW in the pipeline is  $v$ , the distance between the leak point and the upstream sensor is  $X$ , the times when the wave is detected by the two sensors are  $t_1$  and  $t_2$ , and the velocity of natural gas in the pipeline is  $u$ .

As the pipeline diameter and gas transportation velocity increase, the velocity of the natural gas cannot be ignored compared with that of the NPW. With the velocity of natural gas taken into consideration in our study, the relations between the length and time variables can be developed as follows:

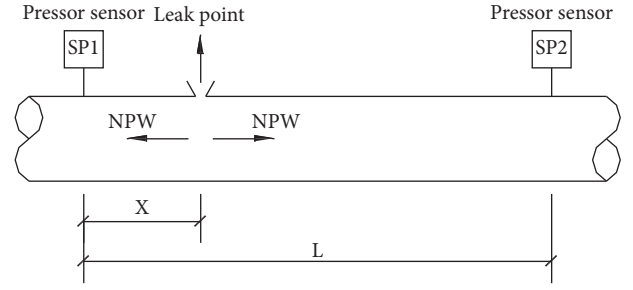


FIGURE 1: Schematic of pressure sensor-based NPW method.

$$\begin{aligned} t_1 &= \frac{X}{v - u}, \\ t_2 &= \frac{L - X}{v + u}, \\ \Delta t &= t_1 - t_2. \end{aligned} \quad (1)$$

The distance between the leak point and the upstream sensor can be obtained from the above three equations:

$$X = \frac{1}{2v} [L(v - u) + \Delta t(v^2 - u^2)]. \quad (2)$$

Equation (2) is the leak location formula.

*2.2. The law of NPW Propagation and Attenuation.* Wave propagation is a form of energy transmission and the NPW is no exception. Energy loss is inevitable in this process and the mathematical model of NPW attenuation [27] is

$$|\Delta P_x| = |\Delta P_0| e^{-\eta x}, \quad (3)$$

where  $|\Delta P_0|$  is the value of the NPW at the leak point,  $|\Delta P_x|$  is the value of the NPW at the point that is a distance of  $x$  from the leak point, and  $\eta$  is the attenuation coefficient.  $\eta$  is mainly determined by the internal diameter of the gas pipeline hydraulic friction factor gas compression factor NPW velocity and other factors. It is easy to see from equation (3) that the value of the NPW is inversely proportional to  $x$ .

As shown in Figure 1, when leakage occurs at the leak point according to the attenuation law of the NPW, the following can be obtained:

$$|\Delta P_1| = |\Delta P_0| e^{-\eta X}, \quad (4)$$

$$|\Delta P_2| = |\Delta P_0| e^{-\eta(L - X)}. \quad (5)$$

The pressure values measured by SP1 and SP2 before and after the occurrence of the leak are recorded. The difference between the two values is the pressure value of the NPW at these two points, namely,  $|\Delta P_1|$  and  $|\Delta P_2|$ . Moreover,  $X$  and  $L$  are known. Therefore, the pressure value of the NPW at the leak point  $|\Delta P_0|$  can be obtained by combining equations (4) and (5).

According to equations (4) and (5), it can be seen that the further away from the leak point, the greater the attenuation

of the NPW is and thus the smaller the pressure value of the NPW is. In contrast, the closer it is to the leak point, the smaller the attenuation of the NPW will be and thus the greater the pressure value of the NPW will be. The pressure value of the NPW is inversely proportional to the distance from the leak point.

**2.3. Minimum Detectable Pressure Value of the Pressure Sensor.** Pressure sensors are typically installed at the beginning and end of a section of pipe, as shown in Figure 1. The necessary condition for successful leak detection is that the pressure value of the NPW at these two sensors should be greater than the minimum detectable pressure value of these two sensors. That is, it satisfies the following inequality:

$$\begin{aligned} |\Delta P_1| > |\Delta P_1|_{\min} &= \lambda_1 \sqrt{h_1^2 + \sigma_1^2}, \\ |\Delta P_2| > |\Delta P_2|_{\min} &= \lambda_2 \sqrt{h_2^2 + \sigma_2^2}, \end{aligned} \quad (6)$$

where  $|\Delta P_1|_{\min}$  and  $|\Delta P_2|_{\min}$  are the minimum detectable pressure values of SP1 and SP2,  $\lambda_1$  and  $\lambda_2$  are the sensitivity coefficients of SP1 and SP2, respectively, and  $\sigma_1$  and  $\sigma_2$  are the standard deviation of noise at these two points  $h_1$  and  $h_2$  which are the measurement errors of SP1 and SP2.  $h_1$  and  $h_2$  can be calculated by the following equations:

$$\begin{aligned} h_1 &= (H_{1,\max} - H_{1,\min})\delta_1, \\ h_2 &= (H_{2,\max} - H_{2,\min})\delta_2, \end{aligned} \quad (7)$$

where  $H_{i,\max}$  and  $H_{i,\min}$  represent the upper and lower limits of the sensor range, respectively, and  $\delta_1$  and  $\delta_2$  represent the precision of SP1 and SP2. For certain sensors,  $h_1$  and  $h_2$  are constant.  $\sigma_1$  and  $\sigma_2$  can be calculated from actual data.

It can be seen from the abovementioned analysis that the minimum detectable pressure values of the sensors are determined by the precision of the sensors, the upper and lower limits of the sensor, and other parameters. Once the sensors are determined, the minimum detectable pressure values are determined.

**2.4. Disadvantages of Pressure Sensor-Based NPW Method.** According to the abovementioned study and the principle of fluid mechanics, the key to leak detection is whether the pressure values of the NPW at the sensors are greater than the minimum detectable pressure values of the sensors. The pressure values of the NPW at the sensors depend on the pipeline operating pressure, the leakage rate, and the distance between the leak point and the sensors. These pressure values are inversely proportional to the distance between the leak point and the sensors and are directly proportional to the operating pressure and the leakage rate. Among them, the operating pressure and leakage rate are uncontrollable which makes the distance between the leak point and the sensors a key factor affecting the pressure value of the NPW.

Pressure sensors are used to detect the NPW in this method. Since the installation of pressure sensors requires altering, the pipeline structure pressure sensors are usually

installed at the head and end of a pipeline or at compressor stations before the pipeline is placed into operation. Once the pipe is running, it is difficult to install pressure sensors. As a result, pressure sensors are typically placed far apart. When a leak occurs, the distance between the leak point and the pressure sensors is generally far. According to the analysis in Section 2.2, the pressure values of an NPW exhibit large attenuations at this time. If the pipeline operating pressure or leakage rate is low at this time, the pressure values of the NPW at the sensors are easily less than the minimum detectable pressure values of the pressure sensors and the NPW will be difficult to detect. This is the reason why the pressure sensor-based NPW method is basically ineffective for small leaks and has a high failure rate.

### 3. FBG Strain Sensor-Based NPW Method

Through the abovementioned study, it can be seen that to overcome the shortcomings of the pressure sensor-based NPW method, the pressure value of the NPW at the sensors must be increased. The most direct way to achieve this is to reduce the distance between the leak point and the sensors to reduce the attenuation of the NPW and achieve the purpose of increasing the pressure value of the NPW at the sensors. In this paper, a method based on an FBG strain sensor is proposed to detect the NPW.

**3.1. Using an FBG Strain Sensor to Detect NPW in the Pipeline.** An FBG sensor is a kind of fiber optic sensor in which ordinary light will pass through a grating without being affected by it. Only certain wavelengths of light will be reflected at the grating. The spacing of the grating will change due to changes in external stress or temperature which will also change the wavelength of the light reflected by the grating. Therefore, the strain and temperature changes in the external environment where the grating is located can be detected by monitoring the wavelength change in the reflected light.

Figure 2 shows a schematic diagram of a clamping FBG strain sensor. It can be seen in the figure that this sensor mainly consists of three parts: an FBG, a clamping part, and a fixed end. The FBG is glued and fixed on the clamping part. Assume the distance between the two fixed ends is  $I$  and the distance between the two clamping parts is  $I_f$ . The external strain is  $\varepsilon$  and the central wavelength of the sensor changes to  $\Delta\lambda_{\text{FBG}}$ .

According to the material mechanics and optical fiber sensing principle, the relationship between the central wavelength change of the sensors and the external strain can be written as follows:

$$\varepsilon = \frac{I_f \Delta\lambda_{\text{FBG}}}{1.2I}. \quad (8)$$

Equation (8) shows that the external strain is directly proportional to the central wavelength change of the sensor, so the external strain can be detected by measuring the central wavelength change of the sensor.

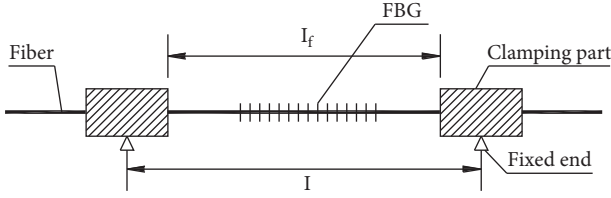


FIGURE 2: Sketch map of clamping FBG strain sensor.

The FBG strain sensors developed in this study are wrapped around the wall of the pipeline, as shown in Figure 3. A change in pressure within the pipeline leads to its expansion or contraction with the annular (circumferential) strain of the pipeline changing accordingly. The FBG strain sensors detect pressure changes within the pipe by sensing the annular strain. The annular strain within a pipeline system can be expressed as

$$\varepsilon = \frac{\sigma_y - \nu\sigma_z}{E}, \quad (9)$$

where  $\varepsilon_y$  is the pipeline annular strain,  $\nu$  is the pipeline Poisson's ratio,  $\sigma_y$  is the pipeline annular stress,  $\sigma_z$  is the pipeline axial stress, and  $E$  is the pipeline elasticity modulus.

Using equation (9), a relationship can be derived to relate the annular strain with the pipeline pressure and pipe wall thickness. First, it is assumed that the pipeline is infinitely long, so the axial stress can be neglected, that is,  $\sigma_z = 0$ . Meanwhile, as  $\sigma_y = PD_w/2h$ , the values for  $\sigma_y$  and  $\sigma_z$  can be substituted into equation (9) which gives

$$\varepsilon = \frac{PD_w}{2hE}, \quad (10)$$

where  $P$  is the pressure in the pipeline,  $D_w$  is the external diameter of the pipeline, and  $h$  is the pipeline wall thickness.

As seen from equation (10), the annular strain of the pipeline is also directly proportional to the pressure in the pipeline, so the pressure change in the pipe can be monitored by monitoring the annular strain of the pipeline. At this time, the distance between the two fixed fulcrums becomes the perimeter of the pipeline, that is,  $I = \pi D_w$ . Therefore, equation (8) can be expressed as

$$\varepsilon = \frac{I_f \Delta\lambda_{\text{FBG}}}{1.2I} = \frac{I_f \Delta\lambda_{\text{FBG}}}{1.2\pi D_w}. \quad (11)$$

Equation (11) is combined with equation (10) to obtain the relationship between the central wavelength change of the sensors and the pressure inside the pipeline as follows:

$$\Delta\lambda_{\text{FBG}} = \frac{0.6\pi D_w^2}{hEI_f} P. \quad (12)$$

Equation (12) shows that the central wavelength change of the sensor is directly proportional to the pressure in the pipeline. Therefore, the pressure in the pipeline can be detected by monitoring the central wavelength of the sensor. This is the operating principle of the FBG strain sensor for detecting pressure changes in the pipeline.

Temperature variations can also affect the annular strain; thus, for actual projects, FBG temperature sensors are needed to compensate for the effect of diurnal or seasonal temperature variations on the annular strain.

**3.2. FBG Strain Sensor-Based NPW Method.** According to the operating principle of the FBG strain sensor, detecting the NPW in pipelines above a leak detection method based on the FBG strain sensor is proposed, as shown in Figure 4. In this method, the FBG strain sensors are set at intervals along the pipeline, so that when a leak occurs in some parts of the pipeline, the leak point is very close to the sensors on both sides. Therefore, the attenuation of the NPW is very small and the pressure value of the NPW at the sensors is relatively large which overcomes the high failure rate of the NPW method based on a pressure sensor. At the same time, since the location of each sensor in this method is known, the calculation method of the leak point location is the same as that of the pressure sensor-based method.

The important reason why FBG strain sensors can be set at shorter intervals is that the installation of these sensors is simple requiring only the partial removal of the anticorrosion layer and adhering the sensor to the outer wall of the pipeline without destroying the pipeline structure. In addition, it is easy to add FBG strain sensors to an existing pipeline, thus realizing nondestructive installation. The cost is also lower. In addition, FBG strain sensors have the advantages of being insensitive to interference signals and exhibiting small attenuations along their traversed length.

### 3.3. Experiment

**3.3.1. Experimental Platform.** The experimental platform for testing the FBG strain sensor-based NPW method is outlined in this paper. The schematic and photo for this platform are shown in Figure 5. Two air tanks and a section of pipeline were used to simulate a realistic gas transfer. The pipeline in this experiment was made of steel with a diameter of 273 mm as frequently used in practice. The pipeline length was 11 m due to lab space limitations. A leak point was simulated by manually opening a valve at different locations, a rotameter was located at the leak point to measure the leak rate, and two FBG strain sensors (SF1 and SF2) and two pressure sensors (SP1 and SP2) were installed.

For safety considerations, the maximum design pressure of this platform was 1.0 MPa and air was used in this experiment instead of natural gas. In this leak detection experiment, we were concerned with physical changes to the pipeline and the chemical properties of natural gas were not involved, so this replacement was appropriate. In addition, due to the short leak time and the constant room temperature, there was no need to consider the effects of temperature variations on the FBG strain sensor or leak detection; thus, there were no temperature sensors installed on this platform.



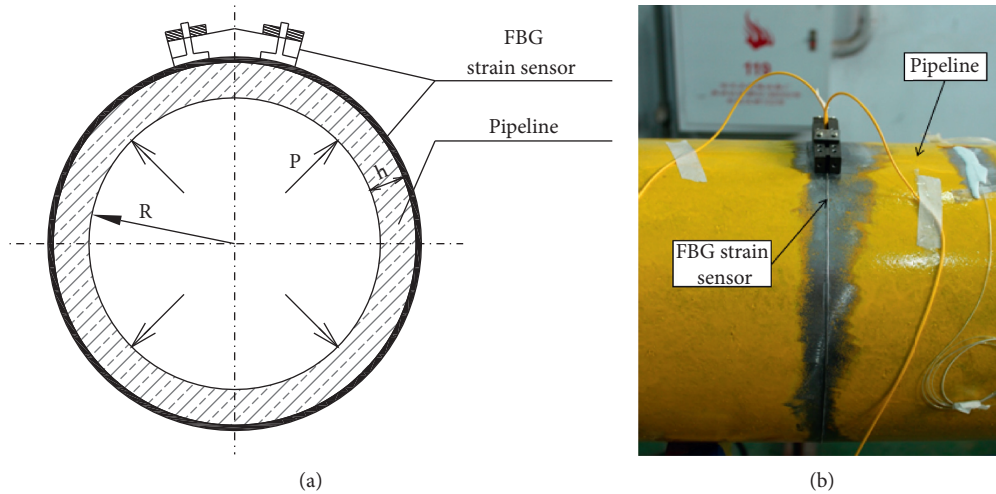


FIGURE 3: (a) Schematic of the FBG strain sensor. (b) Photo of a sensor mounted on a pipeline.

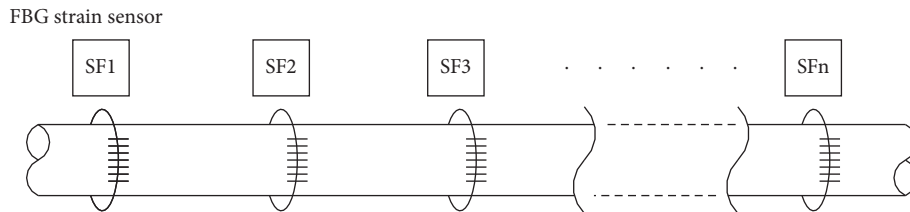


FIGURE 4: Schematic of FBG strain sensor-based NPW method.

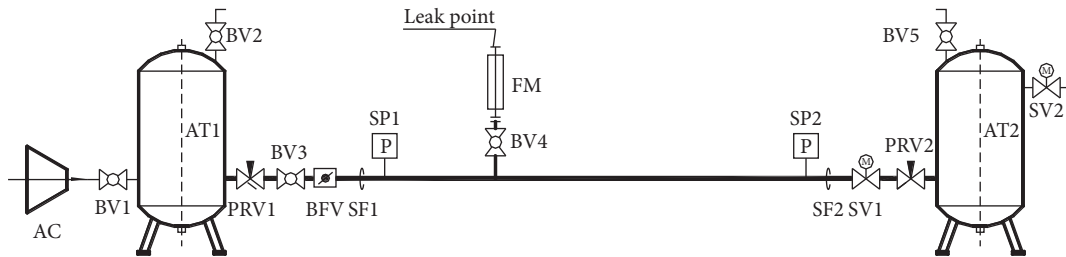
3.3.2. *Calibration of the FBG Strain Sensors.* The FBG strain sensors (SF1 SF2) were calibrated to help determine the relationship between pipeline pressure and wavelength change. The pipeline was pressurized by a compressor from 0 kPa to 800 kPa in approximately 50 kPa increments per step. At each pressure level, the wavelength changes at the fiber receptor were measured. Two calibration test results are plotted in Figure 6, showing the relationship between wavelength change and pressure. It is obvious that the linearity of the pressure-to-wavelength change is excellent and the coefficient of linear association is more than 0.999 which agrees well with the theoretical analysis mentioned above. In accordance with the equation represented in Figure 6, the sensitivity coefficients of these two sensors can also be obtained which are 0.088 pm/kPa and 0.091 pm/kPa, respectively.

3.4. *Experimental Test and Comparison.* The FBG sensors (SF1 and SF2) were tested by the experimental platform and the results were compared with those of the pressure sensors (SP1 and SP2). Briefly, the experimental process followed these four steps: (1) air is compressed into air tank AT1 by air compressor AC. AT1 plays the role of stabilizing the pressure in the pipeline. (2) When the pressure is stable, solenoid valve SV1 is opened to allow the flow of air into the pipeline from AT1 to AT2. (3) Ball valve BV4 at the leak point is opened to simulate a leak in the pipeline. In the meantime,

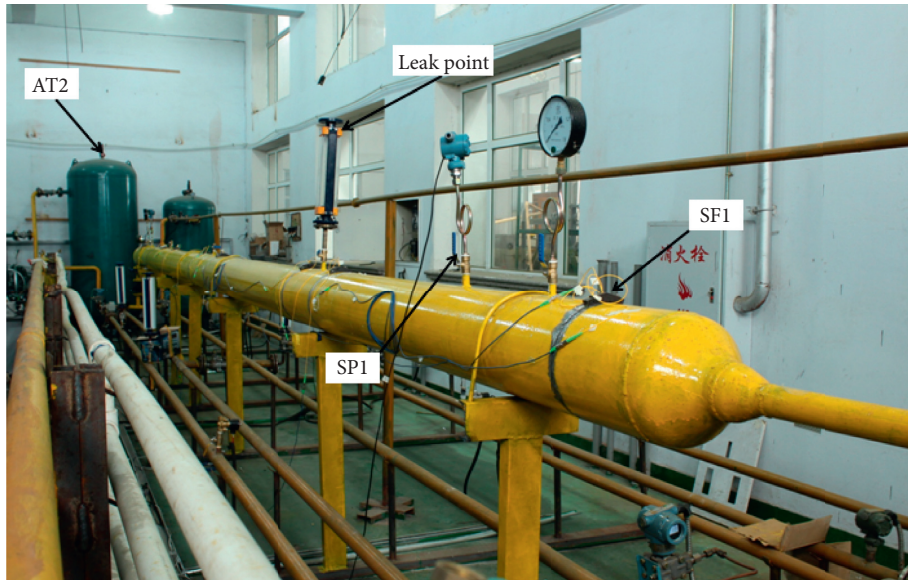
all the sensors gather data. (4) After a period of time, ball valve BV4 is closed and the experiment ends.

Figure 7 shows the pressure signal collected by FBG strain sensors SF1 and SF2. As seen in the figure, the pressure in the pipeline is stable before the leak occurs. When ball valve BV4 is opened and the pipeline leaks, the measured pressure signal in the pipeline drops suddenly. This is because the NPW generated by the leak propagates to both sides of the leak point, resulting in pressure drops at the positions of SF1 and SF2 which further causes changes in the annular strain of the outer wall of the pipeline. Strain changes are detected by SF1 and SF2 and thus pressure changes within the pipe are detected. This is consistent with the NPW theory. Figure 7 also shows that after a sudden drop in the pressure waveform, a small rise in the pressure tends to level off. This is because the leak only lasted for a short period of time in the experiment. When ball valve BV4 is closed to stop the leak, the water hammer phenomenon will be formed in the pipeline, causing a rise in the pressure in the pipeline and forming a small shock which will gradually stabilize. However, because of the loss of gas, the restored steady pressure was lower than the initial pressure. This result fully shows that it is feasible to use FBG strain sensors to collect pressure signals in the pipeline and detect gas pipeline leaks.

Figure 8 shows the pressure signal collected by pressure sensors SP1 and SP2. The pressure change trend is consistent with that collected by pressure sensors SF1 and SF2.



(a)



(b)

FIGURE 5: (a) System diagram of the experiment platform, AC, air compressor; AT1 AT2, air tank; SP1 SP2, pressure sensor; SF1 SF2, FBG strain sensor; BFV, butterfly valve; BV1 ~ BV5, ball valve; SV1 SV2, solenoid valve; FM, flowmeter; PRV1 PRV2, pressure-regulating valve. (b) Photo of experiment platform.

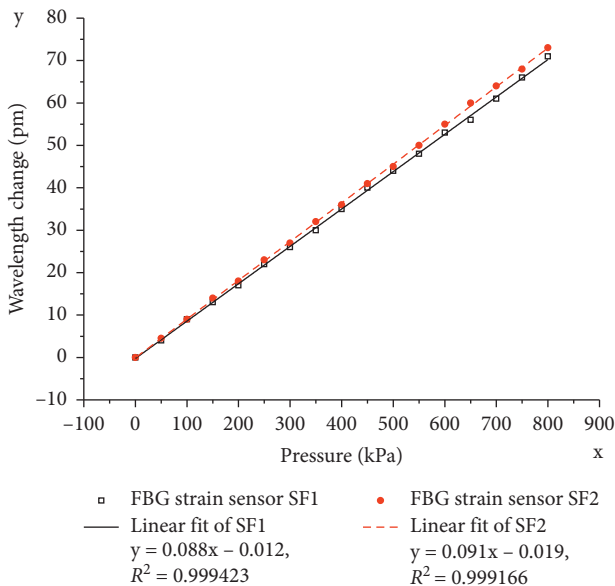


FIGURE 6: Calibration of FBG strain sensors (SF1 SF2).

Figures 7 and 8 can be used to compare the NPW detection effect of the FBG strain sensor and the pressure sensor. First, as can be clearly seen in the two figures, the noise of the signal captured by pressure sensors is significantly higher than the signal captured by the FBG strain sensors. Second, the noise of the signal captured by the pressure sensor SP2 is significantly higher than SP1. This is because the distance between the leak point and SP1 is shorter than the distance between the leak point and SP2. However, additional noise is not significantly present in FBG strain sensor SF2 compared with SF1 even though SF2 is farther from the leak than SF1. Therefore, the noise of the pressure sensors increases with greater distance from the leak point but the FBG strain sensors are less affected by this factor.

These results indicate that (1) FBG strain sensors filter out interference much more than pressure sensors and (2) the attenuation of FBG strain sensors is much smaller than that of pressure sensors. In addition to the above two advantages, FBG strain sensors also have the advantages of simple and nondestructive installation. Therefore, the sensors can be arranged at shorter intervals along the pipeline. This addresses the problems of large signal noise and the ineffective detection of small leaks inherent in the pressure sensor-based NPW method.

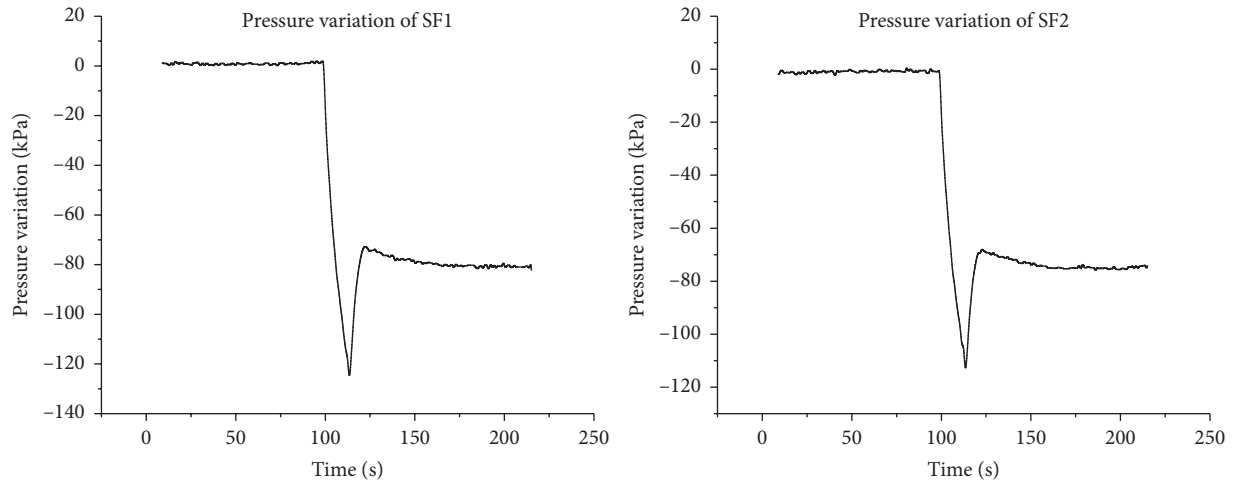


FIGURE 7: Signal captured by SF1 and SF2.

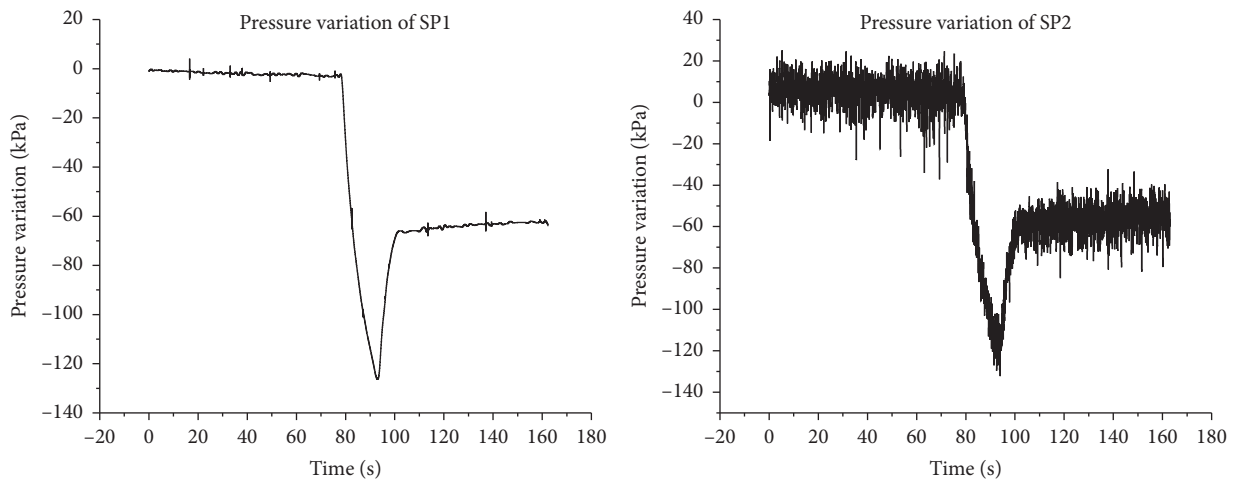


FIGURE 8: Signal captured by SP1 and SP2.

These results demonstrate that the FBG strain sensor-based NPW method is more suitable for natural gas pipeline leak detection.

#### 4. Conclusion

In this paper, the propagation and attenuation of NPWs in natural gas pipelines are introduced, the principle of detecting and locating leaks by the pressure sensor-based NPW method is studied, and the disadvantages of this method are noted. Then, in view of the shortcomings of the pressure sensor-based NPW method, a method of detecting the NPW in a pipeline by using an FBG strain sensor to monitor the annular strain of the pipeline is proposed and a method based on the FBG strain sensor to detect and locate pipeline leaks is proposed. Finally, through experimental tests and comparisons, it is concluded that using an FBG strain sensor to detect an NPW has the advantages of nondestructive installation of high

sensitivity and low interference. Therefore, the FBG strain sensor-based NPW method is easier to install and sensitive to small leaks and low noise, so it is more suitable for leak detection in natural gas pipelines.

As mentioned in Section 3.3.1, the laboratory temperature is relatively constant, thus the effect of temperature variations on the FBG strain sensor and leak detection is not considered in this paper. However, in practical engineering, the natural gas pipelines often span a wide range and have large temperature variation. The influence of temperature variation on leak detection should be further studied.

#### Data Availability

The data used to support the findings are available upon request.



## Conflicts of Interest

The author declares no conflicts of interest.

## Acknowledgments

This research was funded by the Doctoral Research Project of Harbin University of Commerce (no. 2016BS19) and Project of Harbin Science and Technology (no. 2016RAQXJ023). This work was also partially supported by the Fundamental Research Funds for the National Natural Science Foundation of China (no. 51978202), the Natural Science Fund in Heilongjiang Province (no. LH2020E028), and Science Foundation of Harbin University of Commerce (no. 18XN068).

## References

- [1] H. R. Zhang, Y. T. Liang, W. Zhang, N. Xu, Z. L. Guo, and G. M. Wu, "Improved PSO-based method for leak detection and localization in liquid pipelines," *IEEE Transactions on Industrial Informatics*, vol. 14, pp. 3143–3154, 2018.
- [2] H. R. Zhang, Y. T. Liang, Q. Liao, S. Yun, and X. H. Yang, "A self-learning approach for optimal detailed scheduling of multi-product pipeline," *Journal of Computational and Applied Mathematics*, vol. 327, pp. 41–63, 2018.
- [3] Q. Liao, H. R. Zhang, N. Xu, Y. T. Liang, and J. N. Wang, "A MILP model based on flowrate database for detailed scheduling of a multi-product pipeline with multiple pump stations," *Computers & Chemical Engineering*, vol. 11, pp. 763–781, 2018.
- [4] Q. Liao, P. M. Castro, Y. T. Liang, and H. R. Zhang, "New batch-centric model for detailed scheduling and inventory management of mesh pipeline networks," *Computers & Chemical Engineering*, vol. 130, no. 2, Article ID 106568, 2019.
- [5] Z. B. Li, H. X. Feng, Y. T. Liang, N. Xu, S. M. Nie, and H. R. Zhang, "A leakage risk assessment method for hazardous liquid pipeline based on Markov chain Monte Carlo," *International Journal of Critical Infrastructure Protection*, vol. 27, 2019.
- [6] B. Wang, Y. Liang, J. Zheng, T. Lei, M. Yuan, and H. Zhang, "A methodology to restructure a pipeline system for an oilfield in the mid to late stages of development," *Computers & Chemical Engineering*, vol. 115, pp. 133–140, 2018.
- [7] I. R. Ellul, "Advances in pipeline leak detection techniques," *Pipes and Pipelines International*, vol. 34, pp. 7–12, 1989.
- [8] R. A. Silva, C. M. Buiatti, S. L. Cruz, and J. A. F. R. Pereira, "Pressure wave behavior and leak detection in pipelines," *Computers and Chemical Engineering*, vol. 20, pp. 491–496, 1996.
- [9] B. Vogel, C. Cassens, A. Graupner, and A. Trostel, "Leakage detection systems by using distributed fiber optical temperature measurement," *SPIE*, vol. 4328, pp. 23–34, 2001.
- [10] E. A. Mendoza, R. A. Lieberman, J. D. Prohaska, and D. P. Robinson, "Distributed fiber optic chemical sensors for detection of corrosion in pipelines and structural components," *SPIE*, vol. 3398, pp. 136–143, 1998.
- [11] O. S. Wolfbeis, "Fiber-optic chemical sensors and biosensors," *Analytical Chemistry*, vol. 78, no. 12, pp. 3859–3874, 2006.
- [12] C. McDonagh, C. S. Burke, and B. D. MacCraith, "Optical chemical sensors," *Chemical Reviews*, vol. 108, no. 2, pp. 400–422, 2008.
- [13] D. S. Mekeehan, R. W. Griffiths, and J. E. Halkyard, "Marine application for a continuous fiber optic strain monitoring system," in *Proceedings of the 18th Annual OTC*, pp. 342–345, Houston, TX, USA, May 1986.
- [14] S. Yashiro, T. Okabe, and N. Takeda, "Damage identification in a holed CFRP laminate using a chirped fiber Bragg grating sensor," *Composites Science and Technology*, vol. 67, no. 2, pp. 286–295, 2007.
- [15] H. Tsuda, J.-R. Lee, and Y. Guan, "Fatigue crack propagation monitoring of stainless steel using fiber Bragg grating ultrasound sensors," *Smart Materials and Structures*, vol. 15, no. 5, pp. 1429–1437, 2006.
- [16] D. C. Betz, G. Thursby, B. Culshaw, and W. J. Staszewski, "Advanced layout of a fiber Bragg grating strain gauge rosette," *Journal of Lightwave Technology*, vol. 24, no. 2, pp. 1019–1026, 2006.
- [17] E. Liu, L. Lv, Y. Yi, and P. Xie, "Research on the steady operation optimization model of natural gas pipeline considering the combined operation of air coolers and compressors," *IEEE Access*, vol. 7, Article ID 83251, 2019.
- [18] E. Liu, X. Ma, and M. Zhou, "Analysis of discharge process of oil pipeline with complex topography," *Energy Reports*, vol. 5, pp. 678–687, 2019.
- [19] J. Zheng, Y. Dai, Y. Liang, Q. Liao, and H. Zhang, "An online real-time estimation tool of leakage parameters for hazardous liquid pipelines," *International Journal of Critical Infrastructure Protection*, vol. 31, Article ID 100389, 2020.
- [20] H. Lu, T. Iseley, S. Behbahani, and L. Fu, "Leakage detection techniques for oil and gas pipelines: state-of-the-art," *Tunnelling and Underground Space Technology*, vol. 98, Article ID 103249, 2020.
- [21] H.-J. Park and M. Song, "Linear FBG temperature sensor interrogation with Fabry-Perot ITU multi-wavelength reference," *Sensors*, vol. 8, no. 10, pp. 6769–6776, 2008.
- [22] N. Takeda, Y. Okabe, J. Kuwahara, S. Kojima, and T. Ogisu, "Development of smart composite structures with small-diameter fiber Bragg grating sensors for damage detection: quantitative evaluation of delamination length in CFRP laminates using Lamb wave sensing," *Composites Science and Technology*, vol. 65, no. 15–16, pp. 2575–2587, 2005.
- [23] A. Dandridge and C. Kirkendall, "Passive fiber optic sensor networks," in *Handbook of Optical Fiber Sensing Technology*, J. M. López-Higuera, Ed., pp. 433–448, Wiley, New York, NY, USA, 2002.
- [24] H. Tsuda, "Ultrasound and damage detection in CFRP using fiber Bragg grating sensors," *Composites Science and Technology*, vol. 66, no. 5, pp. 676–683, 2006.
- [25] Q. M. Hou, W. L. Jiao, L. Ren, H. Z. Cao, and G. B. Song, "Experimental study of leakage detection of natural gas pipeline using FBG based strain sensor and least square support vector machine," *Journal of Loss Prevention in the Process Industries*, vol. 8, pp. 56–69, 2014.
- [26] R. M. López, V. V. Spirin, M. G. Shlyagin et al., "Coherent optical frequency domain reflectometry for interrogation of bend-based fiber optic hydrocarbon sensors," *Optical Fiber Technology*, vol. 10, no. 1, pp. 79–90, 2004.
- [27] A. B. Sergey, F. L. Oleg, and Energoavtomatika Ltd, "Waves Attenuation and the Pressure Surge Method Performance," in *Proceedings of the PSIG Annual Meeting*, Alberta, Canada, October 2007.

## Research Article

# Modified Leakage Rate Calculation Models of Natural Gas Pipelines

Qingmin Hou <sup>1</sup>, Daheng Yang,<sup>1,2</sup> Xiaoyan Li,<sup>1</sup> Guanghua Xiao,<sup>3</sup> and Siu Chun Michael Ho<sup>4</sup>

<sup>1</sup>School of Energy and Building Engineering, Harbin University of Commerce, Harbin 150028, China

<sup>2</sup>School of Food Engineering, Harbin University of Commerce, Harbin 150028, China

<sup>3</sup>Department of Municipal and Environmental Engineering, Heilongjiang Institute of Construction Technology, Harbin 150025, China

<sup>4</sup>Department of Mechanical Engineering, University of Houston, Houston, TX 77004, USA

Correspondence should be addressed to Qingmin Hou; [sspawm@163.com](mailto:sspawm@163.com)

Received 9 October 2020; Revised 11 November 2020; Accepted 24 November 2020; Published 7 December 2020

Academic Editor: Yufei Wang

Copyright © 2020 Qingmin Hou et al. This is an open access article distributed under the Creative Commons Attribution License, which permits unrestricted use, distribution, and reproduction in any medium, provided the original work is properly cited.

The leakage rate is an essential parameter for the risk assessment and failure analysis of natural gas pipelines. The leakage rate of a natural gas pipeline should be calculated quickly and accurately to minimize consequences. First, in this study, models to estimate the leakage rate of natural gas pipelines are reclassified, and the theoretical range of application for each model is also analysed. Second, the impact of the leakage on the flow rate upstream of the leak point is considered, and the method of successive approximation is used to realize this feedback effect of flow rate change. Then, a modified hole-pipe model is developed to calculate the natural gas leakage rate in this paper. Compared with the leakage rate calculated by the hole-pipe model, the leakage rate calculated by the modified hole-pipe model is smaller and closer to the actual leakage rate due to the consideration of the feedback effect of the flow rate change. Finally, the leakage rate curves of the hole-pipe model and the modified hole-pipe model under different  $d/D$  conditions are obtained through simulation. The simulation results show that the modified hole-pipe model is able to calculate the leakage rate of any leak aperture, such as the hole-pipe model, and also at a higher accuracy level than the hole-pipe model.

## 1. Introduction

Natural gas is a high-quality, efficient, and clean source of energy. Since the 1970s, worldwide consumption of natural gas has accelerated, and research on natural gas exploitation, transportation, and storage has also increased to meet demands [1–10]. Pipeline infrastructure has been erected around the globe to support the natural gas operations. The sheer lengths of pipeline laid in a wide variety of environments inevitably lead to accelerated pipeline damage and failures in certain situations. International statistics of natural gas pipeline accidents show that artificial damage, construction errors, material defects, and corrosion are the common causes of natural gas pipeline leakages. Leakages can lead to fires and even deadly explosions; therefore, it is crucial to rapidly mitigate any pipeline accidents to reduce human, environmental, and corporate losses. Estimating the

leakage rate of a damaged natural gas pipeline is the first step for predicting the area affected by the leakage and guiding any needed personnel evacuation.

Due to the importance of rapid leakage detection and analysis, many researchers have contributed to the development of leakage models. Montiel et al. first proposed the concept of the hole-pipe model and discussed the usage of small hole, large hole, and pipe models of pipeline leakage [11]. Zhou analysed the thermal process of slow discharge of natural gas storage tanks and established a corresponding mathematical model [12, 13]. Woodward and Mudan proposed an ideal fluid leakage model for small holes in compression vessels [14]. Based on their model, the Center for Chemical Process Safety (CCPS) proposed several approximate formulas for calculating leakage rates under certain conditions [15]. Young et al. proposed a simplified calculation model for the small hole leakage rate of high-

pressure gas pipelines while considering the safety margin often required in practical situations, and due to the margin, the calculated results were larger than the actual results [16, 17]. Arnaldos et al. performed a simple analysis of the leakage rate calculation for both the pipe model and the small hole model [18]. Levenspiel developed a leakage model for when the pipeline is completely fractured and analysed the pressure drop along the pipeline. However, the model was developed based on the assumption that the pressure at the starting point remains constant and the gas flow and leakage in the pipe are adiabatic processes [19]. Dong calculated the steady state gas leakage of the long-distance pipeline [20]. Yang et al. established a steady state leakage model of a nonisothermal long-distance pipeline [21].

From these studies, the following conclusions can be drawn: The leakage models are usually classified into three types: (1) a small hole model which can be used to calculate the leakage rate of small holes. This model not only ignores the friction along the pipelines but also does not consider the effect of leakage on the pressure in the pipelines. Therefore, the error of this model is large, especially when the leak point is not small. (2) A pipe model to calculate the leakage rate of a natural gas pipeline when the pipeline is completely broken. This model assumes isentropic release, and a constant pressure is assumed at an initial point in the pipe. The pressure drop along the pipe is taken into account. This model provides accurate predictions for the case where the natural gas pipeline is completely broken, but it cannot be applied to the flow through holes with a diameter smaller than the pipe diameter. (3) The hole-pipe model, which was first proposed by Montiel et al., then became the critical cornerstone of the field. Theoretically, this widely used model can calculate the leakage rate for various apertures. The friction along the pipelines and the effect of leakage on the pressure in the pipelines are both taken into account in this model. However, the effect of leakage on the flow rate of natural gas pipelines is not considered. When the hole diameter is larger than the typical small hole diameter and smaller than the pipeline diameter, the error still cannot be ignored.

Based on the above analysis, this paper reclassifies the original leakage models. Furthermore, four new models for calculating the leakage rate are developed: the storage tank model, small hole model, modified hole-pipe model, and pipe model. The characteristics of each model and the specific conditions of their application are detailed. Considering how flow rate changes in natural gas pipelines can cause a feedback phenomenon, a modified hole-pipe model is proposed in this paper for calculating the leakage rate of various apertures, and an example is used to verify the superiority and rationality of the models.

## 2. Reclassification of the Leakage Rate Calculation Models

In the traditional classification, leakage rate calculation models are usually divided into three categories. According to the actual situations, this paper reclassifies them into four categories and gives the applicable scope of each model.

The system analysed is shown schematically in Figure 1 [11]. As shown in this figure, there is a length of pipeline  $L_e$  after which there is a hole with a certain diameter through which the pressure release takes place.

Locations of interest include point 1, at the beginning of the pipe

Point 2, at the center of the pipeline, on the same vertical axis as the leak point

Point 3, at the leak point

Point 4, at the outside of the pipe, exposed to atmospheric pressure

To calculate the leakage rate, the following hypotheses are assumed: (a) a model of essentially one-dimensional flow; (b) isentropic flow at the release point and adiabatic flow in the pipe; and (c) the gas behaves as an ideal gas. An air compression factor is added to the ideal gas equation of state to reduce the difference from the actual gas.

By applying the energy and momentum equations to the adiabatic flow through a pipeline, the following equation is obtained [22]:

$$\frac{k+1}{k} \ln\left(\frac{P_1 T_2}{P_2 T_1}\right) + \frac{M}{RG^2} \left(\frac{P_2^2}{T_2} - \frac{P_1^2}{T_1}\right) + \left(\frac{4\lambda X_e}{D}\right) = 0. \quad (1)$$

In this expression,  $\lambda$  is the Fanning friction factor. The natural gas leakage rate  $K$  at the hole can be calculated using the following expression, which is obtained from the continuity equation and the law of ideal gases for an isentropic expansion:

$$K = C_D A_{or} P_2 \sqrt{\frac{M}{ZRT_2} \frac{2k}{k-1} \left[ \left(\frac{P_a}{P_2}\right)^{2/k} - \left(\frac{P_a}{P_2}\right)^{k+1/k} \right]}, \quad (2)$$

where  $C_D$  is the flow correction coefficient of the leaking hole [23] and is usually set to a value between 0.6 and 1.0. This coefficient is classified according to the shape of the hole. When the exact shape of the hole is unknown, a conservative value of 1.0 is usually recommended. This value was used in this paper [11].

The flow rate at the leak point depends on whether the flow is sonic or subsonic, which can be determined by the critical pressure ratio (CPR):

$$\text{CPR} = \frac{P_a}{P_{2c}} = \left(\frac{2}{k+1}\right)^{k/k-1}, \quad (3)$$

where  $P_{2c}$  is the critical pressure at point 2. If the pressure  $P_2$  at point 2 increases gradually, the speed of gas leakage will increase until it is equal to the local sound speed. At this moment, if  $P_2$  continues to increase, then the gas leakage rate remains constant and is always equal to the local sound speed and demarcates a critical stage of flow.

When  $P_a/P_2 < \text{CPR}$ , then critical flow leakage has been reached, and equation (4) is substituted into equation (2) for the expression of the leakage:

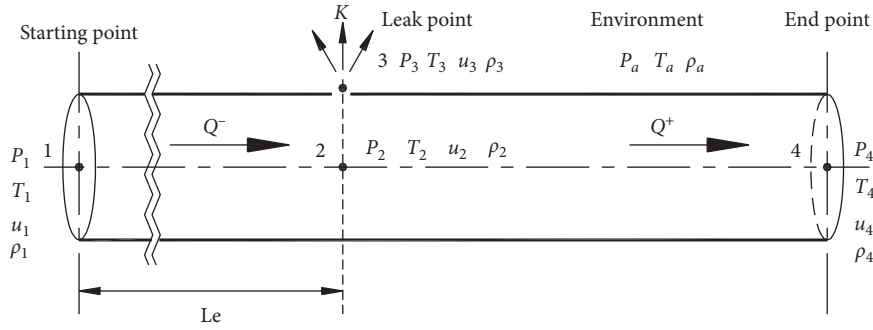


FIGURE 1: Schematic diagram of gas pipe leakage.

$$K = C_D A_{or} P_2 \sqrt{\frac{Mk}{ZRT_2} \left(\frac{2}{k+1}\right)^{k+1/k-1}}. \quad (4)$$

When  $P_a/P_2 \geq \text{CPR}$ , the leakage is at subcritical flow, and the leakage can be calculated by equation (2). Equations (2) and (4) are general formulas for calculating the natural gas leakage rate.

According to different but approximate conditions, natural gas pipeline leakage models (i.e., storage tank model, small hole model, modified hole-pipe model, and pipe model) are established in this paper. These four models will be detailed in the upcoming section.

**2.1. Storage Tank Model.** When a gas storage tank leaks, the following approximate assumptions can be made because of the large size of the tank: (a) the pressure inside the storage tank is not affected by the leakage, and the parameter values at point 2 remain unchanged both before and after the leakage. (b) The pressure loss caused by the friction between the container and the gas flow after the leakage is ignored. By these two assumptions, the parameters of point 1 are used to replace the parameter value of point 2, and the leakage rate can be calculated by formulas (2) and (4), which comprise the storage tank model. This model has been widely used in the accurate calculation of the leakage of large containers, such as storage tanks [18].

All these aspects make this model adequate for the prediction of release through a hole in a tank but not for leakages in natural gas pipelines. Because the gas pipeline is different from the storage tank, especially when point 2 is far from point 1, the pressure loss and velocity caused by internal friction must be considered. The related parameters of point 2 are not exactly the same as those at point 1. The leakage rate calculated by this model is larger than the actual leakage rate. Therefore, in general, the storage tank model is not suitable for the calculation of the natural gas pipeline leakage rates. Only when point 2 is close to point 1 and the hole diameter is very small can the storage tank model be used to calculate the leakage rate for natural gas pipelines.

**2.2. Small Hole Model.** A small hole model is used to calculate the natural gas pipeline leakage rate when the hole is

small. This model takes into account the effect of friction in the natural gas pipeline. Because the leakage is small, the effect of leakage on the pressure and flow rate in the natural gas pipeline is neglected. Assuming that the coefficient of friction is the same along the whole pipeline, the relationship between point 1 and point 2 can be defined by the following equations [11].

$$\frac{k+1}{2} \ln \left[ \frac{Ma_2^2}{Ma_1^2} \frac{2+(k-1)Ma_1^2}{2+(k-1)Ma_2^2} \right] - \left( \frac{1}{Ma_1^2} - \frac{1}{Ma_2^2} \right) + \frac{4\lambda X_\varepsilon}{D} = 0, \quad (5)$$

$$\frac{T_2}{T_1} = \frac{Y_1}{Y_2}, \quad (6)$$

$$\frac{P_2}{P_1} = \frac{Ma_1}{Ma_2} \sqrt{\frac{Y_1}{Y_2}}, \quad (7)$$

$$\frac{\rho_2}{\rho_1} = \frac{Ma_1}{Ma_2} \sqrt{\frac{Y_2}{Y_1}}, \quad (8)$$

where

$$Y_i = 1 + \left( \frac{k-1}{2} \right) \cdot Ma_i^2. \quad (9)$$

In these expressions, Ma is the Mach number, which can be calculated as follows:

$$Ma_i = \frac{u_i}{c} = \frac{u_i}{\sqrt{kZRT/M}}. \quad (10)$$

Under these conditions, the following relationships apply:

When  $P_a/P_2 < \text{CPR}$ , there is a critical flow at the leak point, and the leakage rate can be calculated by equation (4).

When  $P_a/P_2 \geq \text{CPR}$ , there is a subcritical flow at the leak point, and the leakage rate can be calculated by equation (2).

The small hole model considers the pressure loss caused by the friction of the natural gas pipeline and is more accurate than the storage tank model. However, because the small hole model neglects the effect of leakage on the pressure and flow rate in a natural gas pipeline, the parameters at point 2 remain unchanged upstream and downstream of the leakage. This hypothesis is still different



from the actual situation. Therefore, only when the leakage hole is very small can the small hole model be used to calculate the leakage rate.

**2.3. Pipe Model.** The pipe model is used for the case of the complete rupture of the natural gas pipeline or when the leakage diameter is close to the pipe diameter. The state of the natural gas in the pipe is the same as if the gas is in atmospheric conditions. According to the conservation of flow rate, the leakage rate is equal to the flow rate in a natural gas pipeline. Thus, the formula for calculating the natural gas leakage rate is as follows [18]:

$$K = Q = C_D A_{\text{or}} \sqrt{\frac{2M}{ZR} \frac{k}{k-1} \frac{T_2 - T_1}{(T_1/P_1)^2 - (T_2/P_2)^2}} \quad (11)$$

At this time, because the pipeline is completely broken,  $P_2 = P_3 = P_a$ , and  $T_2$  can be obtained by using equation (6). The model gives good predictions for the case of the complete destruction of the natural gas pipelines, but it cannot be applied to the flow through holes with a diameter smaller than the natural gas pipeline diameter.

**2.4. Modified Hole-Pipe Model.** Before introducing the modified hole-pipe model, the hole-pipe model should be introduced first. Two aspects have been taken into account by the hole-pipe model: the pressure loss caused by the friction of the pipeline and the effect of leakage on the pressure in the pipeline. However, the effect of the leakage on the flow rate upstream of the leak point is not considered.

In the hole-pipe model, the leakage rate is also calculated by equations (2) and (4). Equations (5)–(10) express the relationship of parameters between points 1 and 2, and these equations are substituted into equations (2) and (4) to reflect the consideration of pressure loss caused by the friction of the natural gas pipeline.

For the critical flow at the leak point hole, the relationship of parameters between points 2 and 3 is defined as follows:

$$\begin{cases} P_3 = \left[ \frac{2}{(k+1)} \right]^{k/(k-1)} P_2, \\ T_3 = \left[ \frac{2}{(k+1)} \right] T_2, \\ \rho_3 = \left[ \frac{2}{(k+1)} \right]^{1/(k-1)} \rho_2. \end{cases} \quad (12)$$

For the subcritical flow at the leak point hole, the pressures at point 3 and the environment are same, so the relationship of parameters between points 2 and 3 is defined as follows:

$$\begin{cases} P_3 = P_a, \\ T_3 = \left( \frac{P_a}{P_2} \right)^{(k-1)/k} T_2, \\ \rho_3 = \left( \frac{P_a}{P_2} \right)^{1/k} \rho_2. \end{cases} \quad (13)$$

Equations (12) and (13) are used to calculate  $P_2$  after leakage occurs, and this can reflect the effect of leakage on the pressure, but the calculations are complicated.

The above is the main introduction of the hole-pipe model.

The modified hole-pipe model proposed in this paper is also used to calculate the gas leakage rate when the leak point hole diameter is larger than that of the small hole model. Because the hole diameter and leakage rate are larger, the influence of the following two aspects are considered:

- (a) The effect of leakage on the pressure in the natural gas pipeline. The pressure at leak point  $P_2$  will be reduced after leakage occurs, and the corresponding leakage rate will change. This effect has been taken into account by the hole-pipe model, but it requires complicated calculations. This effect is also considered in the modified hole-pipe model, and the successive approximation method is used to avoid complicated calculations.
- (b) The effect of leakage on the flow rate upstream of the leak point. According to the law of conservation of mass, the flow rate upstream of the leak point should be equal to the sum of the leakage rate and the flow rate downstream the leak point. Thus, the flow rate upstream of the leak point will change, leading to a change in the pressure in the pipeline. The change in pressure further affects the leakage rate, which in turn affects the flow rate upstream of the leak point. This series of events acts as a feedback loop. The effect of leakage on the flow rate upstream of the leak point will extend to the vicinity of the source, and this is not taken into account by the hole-pipe model but is considered in the proposed modified hole-pipe model.

For convenience of calculation, the pressure  $P_4$  at the end of the pipe is assumed to be a fixed value. In this model, the method of successive approximation is used to calculate the natural gas leakage rate. The concrete steps are as follows:

- (1) The flow rate upstream of the leak point  $Q^-$  is known, and the leakage rate  $K$  and the pressure of point 2  $P_2$  are calculated by the small hole model
- (2) If  $P_2 > P_4$ , then the pipe flow rate after the leak point  $Q^+$  can be obtained according to pressures  $P_2$  and  $P_4$ . According to mass conservation, the natural gas pipeline flow rate before the leak point can be obtained by  $Q^- = K + Q^+$ , and  $Q^-$  is inserted into step 1 to calculate the new  $K$  and  $P_2$ . This process is

iterated until the calculation results of the natural gas leakage rate tend to be stable.

- (3) If  $P_2 \leq P_4$ , then the natural gas pipeline flow rate after the leak point  $Q^+$  is 0. According to the mass conservation,  $Q^{-'} = K$  can be obtained, and  $Q^{-'}$  is inserted into step 1 to calculate the new  $K'$  and  $P_2'$ . This process is continued until the calculation results of the natural gas leakage rate are stable.

The flowchart of the modified hole-pipe model is shown in Figure 2, where  $\sigma$  represents the threshold.

Through the above specific steps, it can be found that the  $P_2'$  and  $P_2$  obtained after a cycle will inevitably change. Thus, the influence of the change in  $P_2'$  on the flow state in the pipe should be considered. The flow at the leak point hole can then be classified as critical flow and subcritical flow, and the three states of flow in the pipeline and at the hole can be obtained:

- (a) Subcritical flow in the pipeline and the critical flow at the leak point hole

$$\begin{cases} P_2' > P_1 Ma_1 \sqrt{\frac{2Y_1}{k+1}}, \\ \frac{P_a}{P_2'} < \text{CPR} \iff P_2' > P_{2c}. \end{cases} \quad (14)$$

At this point, the formula for calculating the leakage rate by the small hole model in step 1 is equation (4)

- (b) Subcritical flow in the pipeline and the subcritical flow at the leak point

$$\begin{cases} P_2' > P_1 Ma_1 \sqrt{\frac{2Y_1}{k+1}}, \\ \frac{P_a}{P_2'} \geq \text{CPR} \iff P_2' \leq P_{2c}. \end{cases} \quad (15)$$

At this point, the formula for calculating the leakage rate by a small hole model in step 1 is equation (2)

- (c) Critical flow in the natural gas pipeline and the critical flow at the leak point

$$\begin{cases} P_2' < P_1 Ma_1 \sqrt{\frac{2Y_1}{k+1}}, \\ \frac{P_a}{P_2'} < \text{CPR} \iff P_2' > P_{2c}. \end{cases} \quad (16)$$

At this point, the formula for calculating the leakage rate by a small hole model in step 1 is equation (4)

Similarly, the pressure  $P_2'$  at point 2 obtained in each cycle should be selected as described above. The modified

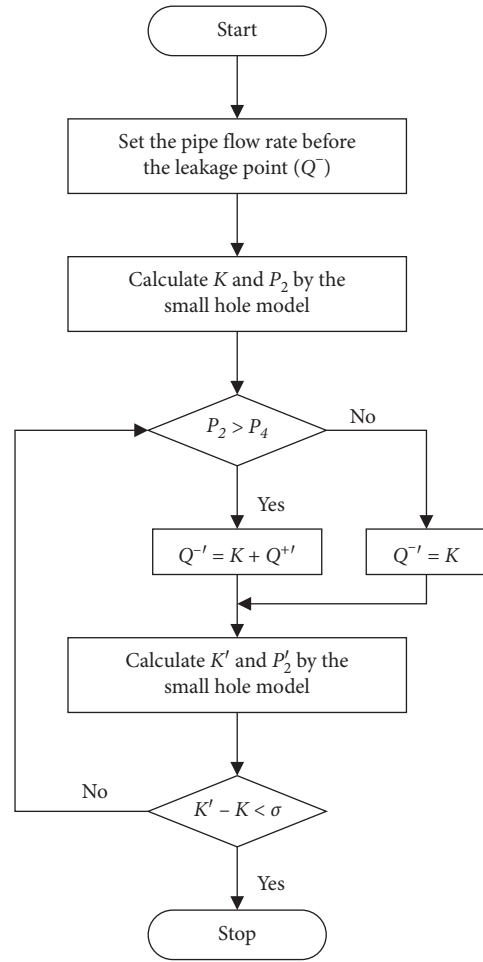


FIGURE 2: Flow chart of the modified hole-pipe model.

hole-pipe model takes into account the effect of leakage on the flow rate of the natural gas pipeline upstream and downstream the leak point, which is more in line with the actual situation. Moreover, the iterative approximation method used in this model can avoid the need for complicated mathematical derivations.

### 3. Comparison between Models

Due to the flammable and explosive character of natural gas, it is impractical to carry out leakage rate measurement experiments on real natural gas pipelines. Even if compressed air is used for the experiments, it is difficult to simulate several leakages of different aperture sizes to obtain different  $d/D$  (the ratio of the leak point hole diameter to the pipeline diameter) values. Therefore, simulations are used in this paper to do a comparison between models.

*3.1. Introduction of Calculation Example.* To verify the effectiveness of the models, especially to compare the hole-pipe model and the modified hole-pipe model, this paper applies these models to the following accident scenarios. The parameters are shown in Table 1.

TABLE 1: Basic computational parameters.

$Q$ (kg/s)	$k$	$R$ (J/(mol·K))	Re
108	1.334	8.314	3000
$D$ (m)	$E$ (mm)	$P_a$ (pa)	$M$ (kg/mol)
0.216	0.045	$10^5$	$16.48 \times 10^{-3}$
$P_1$ (MPa)	$P_4$ (MPa)	$T_1$ (k)	$Le$ (m)
18	6.8	293	1300

**3.2. Discussion and Comparison.** Based on the above proposed models as well as the parameters, the relationship between the natural gas leakage rate and  $d/D$  of different models under steady state conditions is shown in Figure 3. The natural gas leakage rates calculated by the storage tank model and the small hole model increase rapidly with increasing  $d/D$ . Only when the  $d/D$  is small are the leakage rates of these two models close to the leakage rate of the modified hole-pipe model, which conforms to the scope of application of these two models. Only when the leakage point is very close to point 1 of the natural gas pipeline and the leakage hole is very small can the storage tank model be applied. It can also be seen from Figure 3 that the leakage rates of the modified hole-pipe model and the hole-pipe model show the same trend, both of which are very close. However, the leakage rate of the modified hole-pipe model is smaller than that of the hole-pipe model. The leakage rate difference at different  $d/D$  values are shown in Figure 4. As  $d/D$  increases, the difference between these two models first increases and then decreases.

When the leakage hole is very small, the small hole model can be applied. The diagram also shows that the natural gas leakage rate calculated by the storage tank model is larger than that of the small hole model, which is also consistent with the effect of the internal friction of the small hole model; therefore, the small hole model is more accurate for calculating the natural gas leakage rate than the storage tank model. Because leakage occurs, the pressure of point 2 will decrease (but will not decrease indefinitely), which makes the leakage rate calculated by the hole-pipe model smaller than the leakage rate calculated by the small hole model; but the difference is not significant. Therefore, when the aperture is small, the leakage rates of the two models are very close. When the aperture increases, the effect of the decrease in the pressure at point 2 on the leakage rate will also increase. Thus, the leakage rate will not continue to increase but will tend towards being smooth and steady and will eventually be equal to the predictions of the pipeline model.

In the case of a real leak, once a leak occurs at a certain point, the flow rate (flow velocity) upstream of the leak point must increase. According to Bernoulli's equation, the flow pressure will decrease as the flow velocity increases. This effect is not considered in the hole-pipe model; thus, the leakage rate calculated by the hole-pipe model is larger than the actual leakage rate. When  $d/D$  is small, the leakage rate is small, the change in flow rate is small, and the pressure of point 2 experiences minimal change compared to the healthy state. Therefore, the feedback effect typically brought on by leakage to the pressure in the pipeline upstream of the

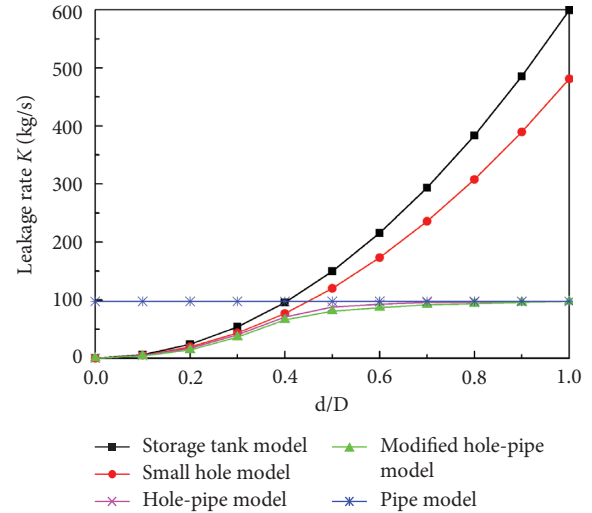
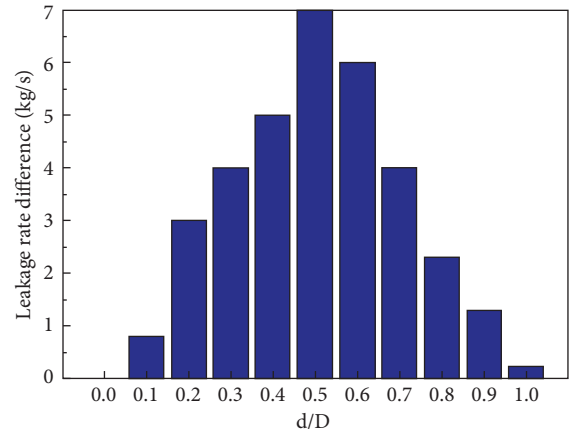
FIGURE 3: Relationship between leakage rate  $K$  and  $d/D$  under different models.

FIGURE 4: Leakage rate difference between the modified hole-pipe model and hole-pipe model.

leakage point can be neglected. However, as the aperture gradually increases, this feedback cannot be neglected. In the modified hole-pipe model, considering the occurrence of leakage at point 2 (as shown in Figure 1), the flow velocity in the pipeline upstream of point 2 will increase while the upstream pressure decreases. At this time, the iterative model in Figure 2 is used to calculate the new pressure and leakage rate of point 2. The iterative model is looped until the relevant parameters of natural gas in the pipeline downstream of leakage are close to the actual situation. Thus, the leakage rate calculated by these parameters is closer to the actual leakage rate, which explains why the leakage rate calculated by the modified hole-pipe model is smaller than the leakage rate calculated by the hole-pipe model (Figure 3). With increasing  $d/D$ , the aperture size increases, and then, the leakage rate increases. Furthermore, the feedback effect of leakage on gas parameters (flow rate, velocity, and pressure) in pipelines becomes increasingly obvious, which makes the leakage rate difference between the modified pipe-hole model and the pipe-hole model increasingly larger.



When  $d/D$  approaches 1, the aperture size is close to the diameter of the natural gas pipeline, and the pressure  $P_2$  of point 2 is decreased and close to  $P_a$ . Subsequently, the leakage rate formula turns to equation (4), so the leakage rates calculated by these two models finally converge to a stable value together, further reducing the difference. This explains why the difference first increases and then decreases in Figure 4.

The natural gas leakage rate calculated by the pipe model is a straight line and does not vary with a change in the leakage aperture. Only when the leakage diameter is close to or equal to the diameter of the natural gas pipeline can the pipe model be applied. When the hole diameter is small, the gas leakage rate of the modified hole-pipe model is very close to the leakage rate calculated by the storage tank model or the small hole model. As  $d/D$  increases, the natural gas leakage rate increases quickly and then slowly flattens. When the leakage aperture is close to the diameter of the natural gas pipeline, the leakage rate calculated by the modified hole-pipe model coincides with the leakage rate calculated by the pipe model. This result indicates that the modified hole-pipe model is suitable for any leakage aperture.

Figure 5 shows the relationship between the natural gas leakage rate  $K$  and  $L_e$  (distance between point 1 and the leakage point) of the modified hole-pipe model ( $P_1 = 18$  MPa) for different  $d/D$ . As the  $L_e$  increases, the natural gas leakage rate exhibits a nonlinear downward trend. This downward trend is due to the reduction of pressure caused by friction inside the pipeline. Moreover, different leakage  $d/D$  ratios have different severities. Specifically, when  $d/D$  is small, the influence of the leakage on the parameters of natural gas in the pipeline is small, and the decrease in the leakage rate is smooth. When the leakage  $d/D$  decreases below a certain extent, the influence of the leakage on the parameters of natural gas in the pipeline can be neglected, and the decrease in the natural gas leakage rate becomes insignificant. When the leakage  $d/D$  increases, the curve becomes flatter. Figure 6 shows the relationship between the  $K$  and  $d/D$  as predicted by the modified hole-pipe model ( $P_1 = 18$  MPa) under different  $L_e$ . It can be seen from this figure that leakage rate curves under each  $L_e$  are similar to the leakage rate curve predicted by the modified hole-pipe model in Figure 3. Figure 6 also shows the leakage rate of the pipe model for each  $L_e$ . The figure further verifies the correctness of the modified hole-pipe model. At the same time, it can be seen from the figure that the leakage rate decreases with  $L_e$ . When  $d/D$  is small, the leakage rate decreases slowly, and as the  $d/D$  increases, the leakage rate decreases more rapidly. This is consistent with the results shown in Figure 5.

Figure 7 shows the relationship between  $K$  and  $P_1$  (the pressure of point 1) of the modified hole-pipe model ( $L_e = 1300$  m) under different  $d/D$ . The natural gas leakage rate increased linearly with increasing  $P_1$ . Additionally, different leakage  $d/D$  ratios lead to different levels of severities. Small  $d/D$  leads to minimized increases in leakage rate from increases in pressure. Conversely, larger  $d/D$  leads to higher sensitivity between pressure and leakage rate. This is because when  $d/D$  is small, the influence of the leakage on

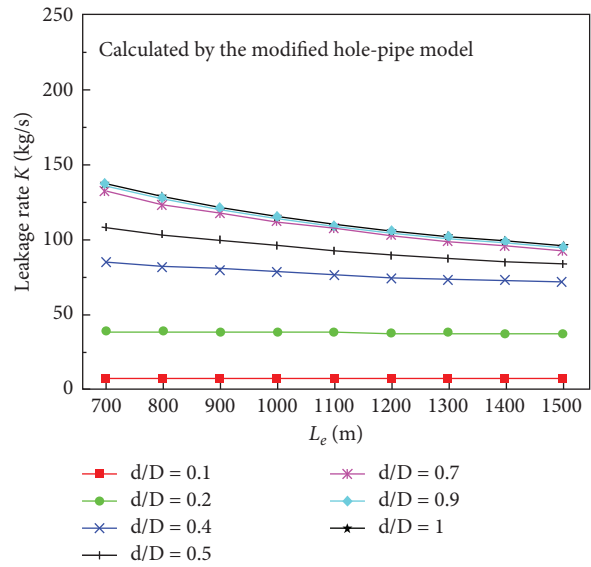


FIGURE 5: Relationship between leakage rate  $K$  and  $L_e$  under different  $d/D$  ( $P_1 = 18$  MPa).

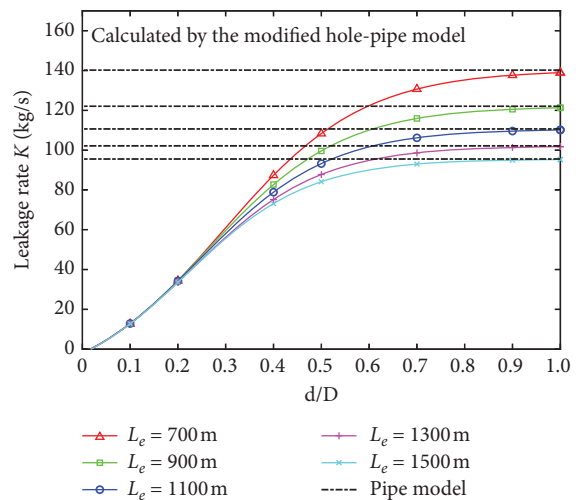


FIGURE 6: Relationship between leakage rate  $K$  and  $d/D$  under different  $L_e$  ( $P_1 = 18$  MPa).

the parameters of natural gas in the pipeline is small; when the  $d/D$  is large, this influence is large. Figure 8 shows the relationship between the natural gas leakage rate  $K$  and  $d/D$  of the modified hole-pipe model ( $L_e = 1300$  m) under different  $P_1$ . It can be seen from this figure that the leakage rate curves under each  $P_1$  are similar to the leakage rate curve predicted by the modified hole-pipe model in Figure 3. Figure 8 also shows the leakage rate of the pipe model under each  $P_1$ . The leakage rate decreases as  $P_1$  decreases. When the  $d/D$  is small, the leakage rate decreases less obviously, and as the  $d/D$  increases, the leakage rate decreases more obviously. This is consistent with the results of Figure 7. The above further verifies the modified hole-pipe model.

Figures 5–8 further demonstrate the correspondence between the parameters of equation (2) and equations

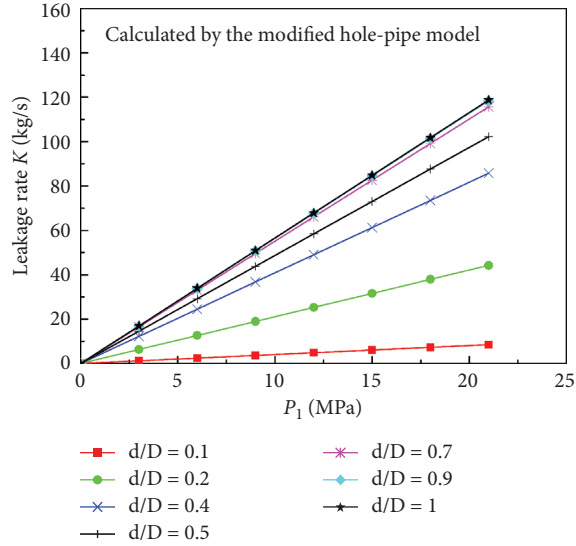


FIGURE 7: Relationship between leakage rate  $K$  and  $P_1$  under different  $d/D$  ( $L_e = 1300$  m).

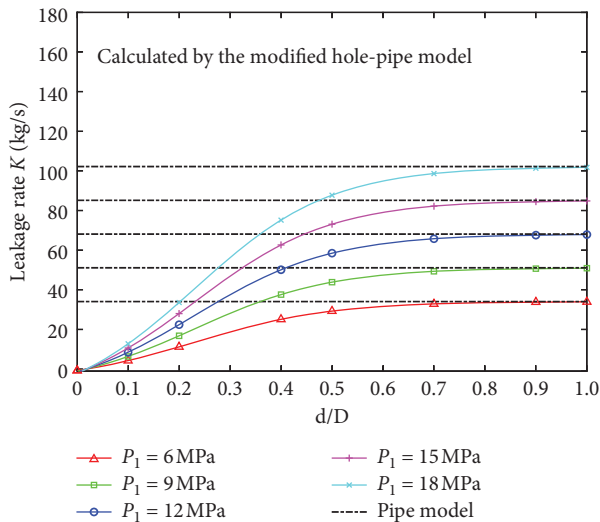


FIGURE 8: Relationship between leakage rate  $K$  and  $d/D$  under different  $P_1$  ( $L_e = 1300$  m).

(4)–(10). The relationship between  $P_2'$  and  $d$  (diameter of the leak point hole) is shown in Figure 9.

According to the algorithm of the modified hole-pipe model shown in Section 2.4, as  $d$  increases, the leakage rate  $K$  increases, and therefore, the flow rate (flow velocity) upstream of the leakage point must increase because of the mass conservation. According to Bernoulli's equation, the flow pressure decreases as the flow velocity increases. From what has been discussed above,  $P_2'$  decreases as  $d$  increases, which is consistent with the trend shown in Figure 9. Furthermore, according to equations (12)–(14), before  $P_2'$  drops to  $P_{2c}$ , the flow at the leakage point is in a state of critical flow. Once  $P_2'$  drops below  $P_{2c}$ , the flow at the leakage point becomes subcritical flow. The demarcation point between critical flow and subcritical flow is about  $d = 195$  mm.

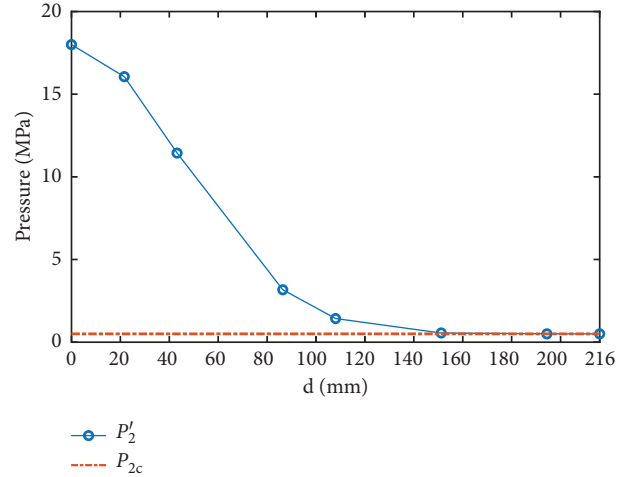


FIGURE 9: Relationship between  $P_2'$  and  $d$  ( $P_1 = 18$  MPa and  $L_e = 1300$  m).

#### 4. Conclusions

This paper reclassifies the natural gas leakage models into four kinds. (a) Storage tank model—in this model, the parameters of the natural gas are considered the same as the parameters of the start point and there is no change when the leak occurs. Therefore, this model is applicable to the case where the leak point is close to the beginning of pipeline, and the leak point diameter is small; (b) small hole model—unlike the storage tank model, this model takes into account the influence of friction along the natural gas pipeline, but the pressure  $P_2$  at point 2 is assumed to remain constant after the leakage. Therefore, this model is applicable to the case where the leak point diameter is small; (c) pipe model—this model is used for the case of the complete rupture of the natural gas pipeline or when the leak point diameter is close to the pipeline diameter; and (d) modified hole-pipe model—this model is a general model that can calculate the leakage rate at any leak point diameter.

The above classifications are more representative of the actual situation. Once the size of the leakage point can be determined, the appropriate model can be selected to estimate the leakage rate. However, the goal of most natural gas pipeline leakage problems is to determine the leakage rate as early as possible, and the leak point diameter cannot be known ahead of time. Therefore, the general model is used to estimate the leakage rate most of the time. In this case, the accuracy of the general model to calculate the leakage rate is crucial for risk assessment and failure consequence analysis. In this paper, a modified hole-pipe model is proposed, and the innovations of this modified model are as follows: (1) considering the influence of leakage on upstream flow rate change, flow rate change will produce flow velocity change. According to Bernoulli's equation, flow velocity change will produce pressure change, and pressure change will further affect the leakage rate, which is a loop problem. This influence is not taken into account in the hole-pipe model, but it is

taken into account in this modified model by using the loop iterative algorithm of successive approximation. (2) In the hole-pipe model, the influence of leakage on the leak point pressure has been considered, but complex hydrodynamics and thermodynamics calculations are required. In this modified hole-pipe model, the successive approximation iterative loop algorithm can take the influence of leakage on the leak point pressure into account and avoids complex computation due to the advantages of the algorithm. A comparison and analysis of the calculation results in this paper shows that the modified hole-pipe model, like the hole-pipe model, is a general model that can calculate the leakage rate at any leak point diameter, and the leakage rate calculated by the modified hole-pipe model is lower than that calculated by the hole-pipe model, which conforms to the theoretical analysis and should be closer to the actual leakage rate. Therefore, the modified hole-pipe model proposed in this paper can calculate the leakage rate more accurately.

## Nomenclature

$P$ :	Pressure (Pa)
$P_i$ :	Pressure for each point (Pa)
$P_a$ :	Pressure for surrounding (Pa)
$P_{2c}$ :	Critical pressure at point 2 (Pa)
$T$ :	Temperature (K)
$T_i$ :	Temperature for each point (K)
$u_i$ :	Flow velocity (m/s)
$G$ :	Mass flux ( $\text{kg}/\text{m}^2\cdot\text{s}$ )
$k$ :	Heat capacity ratio
$Q$ :	Flow rate before leakage point ( $\text{kg}/\text{s}$ )
$Q^+$ :	Flow rate after leakage point ( $\text{kg}/\text{s}$ )
$K$ :	Leakage rate at the leakage point ( $\text{kg}/\text{s}$ )
$M$ :	Molar mass ( $\text{kg}/\text{mol}$ )
$R$ :	Ideal gas constant ( $\text{J}/(\text{mol}\cdot\text{K})$ )
$X_e$ :	Equivalent between point 1 and point 2 (m)
$D$ :	Inner diameter of pipes (m)
$\rho$ :	Density of gas ( $\text{kg}/\text{m}^3$ )
$E$ :	Roughness of pipes (mm)
$Re$ :	Reynolds number
$\lambda$ :	Fanning friction factor
$A_{or}$ :	Hole area ( $\text{m}^2$ )
$C_D$ :	Hole flow correction coefficient
$Z$ :	Air compression factor
CPR:	Critical pressure ratio
$L_e$ :	Distance between point 1 and point 2 (m)
$D$ :	Diameter of the pipeline (mm)
$D$ :	Diameter of the leak point hole (mm).

## Data Availability

The data used to support the findings of this study are available from the corresponding author upon request.

## Conflicts of Interest

The authors declare that they have no conflicts of interest.

## Acknowledgments

This research was funded by Scientific Research Project of Harbin University of Commerce (No. 17XN013) entitled "Research about detection and location of natural gas pipeline leakages based on Kalman filter and Fiber sensing" and the Doctoral Research Project of Harbin University of Commerce (No. 2016BS19).

## References

- [1] H. R. Zhang, Y. T. Liang, W. Zhang, N. Xu, Z. L. Guo, and G. M. Wu, "Improved pso-based method for leak detection and localization in liquid pipelines," *IEEE Transactions on Industrial Informatics*, vol. 14, pp. 3143–3154, 2018.
- [2] H. R. Zhang, Y. T. Liang, Q. Liao, S. Yun, and X. H. Yang, "A self-learning approach for optimal detailed scheduling of multi-product pipeline," *Journal of Computational and Applied Mathematics*, vol. 327, pp. 41–63, 2018.
- [3] Q. Liao, H. Zhang, N. Xu, Y. Liang, and J. Wang, "A milp model based on flowrate database for detailed scheduling of a multi-product pipeline with multiple pump stations," *Computers & Chemical Engineering*, vol. 117, pp. 63–81, 2018.
- [4] Q. Liao, P. M. Castro, Y. T. Liang, and H. R. Zhang, "New batch-centric model for detailed scheduling and inventory management of mesh pipeline networks," *Computers & Chemical Engineering*, vol. 130, 2019.
- [5] Z. B. Li, H. X. Feng, Y. T. Liang, N. Xu, S. M. Nie, and H. R. Zhang, "A leakage risk assessment method for hazardous liquid pipeline based on markov chain monte carlo," *International Journal of Critical Infrastructure Protection*, vol. 27, 2019.
- [6] B. Wang, Y. Liang, J. Zheng, T. Lei, M. Yuan, and H. Zhang, "A methodology to restructure a pipeline system for an oilfield in the mid to late stages of development," *Computers & Chemical Engineering*, vol. 115, pp. 133–140, 2018.
- [7] A. Chebouba, F. Yalaoui, A. Smati, L. Amodeo, K. Younsi, and A. Tairi, "Optimization of natural gas pipeline transportation using ant colony optimization," *Computers & Operations Research*, vol. 36, no. 6, pp. 1916–1923, 2009.
- [8] Q. Ji, Q. Kong, and G. Song, "Study on energy focusing synthesis on pipe using time reversal technique," in *Proceedings of the 11th IEEE International Conference on Networking, Sensing and Control*, pp. 625–630, Miami, FL, USA, 2014.
- [9] G. Park, H. H. Cudney, D. J. Inman, and J. I. Daniel, "Feasibility of using impedance-based damage assessment for pipeline structures," *Earthquake Engineering & Structural Dynamics*, vol. 30, no. 10, pp. 1463–1474, 2001.
- [10] Q. Ji, S. M. Parvasi, S. C. M. Ho, M. Franchek, and G. Song, "Wireless energy harvesting using time reversal technique: an experimental study with numerical verification," *Journal of Intelligent Material Systems and Structures*, vol. 28, no. 19, pp. 2705–2716, 2017.
- [11] H. Montiel, J. Vilchez, J. Casal, and J. Arnaldos, "Mathematical modelling of accidental gas releases," *Journal of Hazardous Materials*, vol. 59, no. 2, pp. 211–233, 1998.
- [12] Z. Zhou, "Thermal analysis of slow discharge from a pressurized natural gas storage tank," *Applied Thermal Engineering*, vol. 17, no. 11, pp. 1099–1110, 1997.
- [13] Z. Zhou, B. Smith, and G. Yadigaroglu, "A mathematical model and its analytical solution for slow depressurization of a gas-filled vessel," *Journal of Engineering Mathematics*, vol. 31, no. 1, pp. 43–57, 1997.

- [14] J. L. Woodward and K. S. Mudan, "Liquid and gas discharge rates through holes in process vessels," *Journal of Loss Prevention in the Process Industries*, vol. 4, no. 4, pp. 161–165, 1991.
- [15] CCPS, *Guidelines for Use of Vapor Cloud Dispersion Models*, AICE, New York, NY, USA, 2 edition, 1996.
- [16] J. D. Young and A. J. Bum, "A simple model for the release rate of hazardous gas from a hole on high-pressure pipelines," *Journal of Hazardous Materials*, vol. 97, pp. 31–46, 2003.
- [17] J. D. Young and A. J. Bum, "Analysis of hazard areas associated with high-pressure natural-gas pipelines," *Journal of Prevention in the Process Industries*, vol. 15, no. 3, pp. 179–198, 2002.
- [18] J. Arnaldos, J. Casal, H. Montiel, M. Sánchez-Carricondo, and J. A. Vilchez, "Design of a computer tool for the evaluation of the consequences of accidental natural gas releases in distribution pipes," *Journal of Loss Prevention in the Process Industries*, vol. 11, no. 2, pp. 135–148, 1998.
- [19] O. Levenspiel, *Engineering Flow and Heat Exchange*, Plenum, New York, NY, USA, 1984.
- [20] Y. H. Dong, "The calculation of the steady-state rate of gas leakage in long-distance pipeline," *Oil and Gas Storage and Transportation*, vol. 34, pp. 11–15, 2002.
- [21] Z. Yang, F. R. Zhang, and J. B. Lai, "Steady leakage calculation models of non-isothermal long gas pipeline," *Journal of Tianjin University of Technology*, vol. 38, pp. 1115–1121, 2005.
- [22] K. Wojciech J and S. Janusz, "Real gas flow simulation in damaged distribution pipelines," *Energy*, vol. 45, pp. 481–488, 2012.
- [23] N. Bariha, I. M. Mishra, and V. C. Srivastava, "Hazard analysis of failure of natural gas and petroleum gas pipelines," *Journal of Loss Prevention in the Process Industries*, vol. 40, pp. 217–226, 2016.

## Research Article

# A Multisource Monitoring Data Coupling Analysis Method for Stress States of Oil Pipelines under Permafrost Thawing Settlement Load

Changliang Jiang <sup>1</sup>, Pengchao Chen <sup>1</sup>, Rui Li <sup>1</sup>, and Xiaoben Liu <sup>2</sup>

<sup>1</sup>Petrochina Pipeline Company, Langfang 065000, Hebei, China

<sup>2</sup>National Engineering Laboratory for Pipeline Safety, MOE Key Laboratory of Petroleum Engineering, Beijing Key Laboratory of Urban Oil and Gas Distribution Technology, China University of Petroleum-Beijing, Beijing 102249, China

Correspondence should be addressed to Xiaoben Liu; [xiaobenliu@cup.edu.cn](mailto:xiaobenliu@cup.edu.cn)

Received 22 October 2020; Revised 5 November 2020; Accepted 13 November 2020; Published 25 November 2020

Academic Editor: Qi Liao

Copyright © 2020 Changliang Jiang et al. This is an open access article distributed under the Creative Commons Attribution License, which permits unrestricted use, distribution, and reproduction in any medium, provided the original work is properly cited.

Thaw settlement is one of the common geohazard threats for safe operation of buried pipelines crossing permafrost regions, as pipes need to bear additional bending stress induced by settlement load. In the presented study, a novel coupled data analysis method was proposed for stress state estimation of buried steel pipeline under thawing settlement load. Multisource data including pipe bending strain derived by inertial measurement unit, pipe longitudinal strain derived by strain gauges, and thawing displacement loads derived by soil temperature monitoring were used to estimate the pipe's mechanical states. Based on the derived data, finite element method-based pipe soil interaction model was established to predict pipe's actual stress distribution. A monitored pipe segment of one crude oil pipeline in northeast China operated since 2010 was adopted as a prototype for the investigation, monitoring data derived in the last ten years was employed to predict the settlement loading, and relative accurate stress results was obtained via the established pipe soil interaction model. The mean absolute error (MAE) of the predicted pipe stresses compared with the monitoring results in 2014, 2017, and 2018 are 5.77%, 12.13%, and 13.55%, respectively. Based on the analyzed stress results, it can be found that the investigated pipe was subjected to an increasing settlement load from 2010–2016, made the bending stress increased up to 149.5 MPa. While after 2016, due to the depth of frost soil in this area is no more than 3.5 m, the thawing settlement load almost remained constant after 2016. As the investigated pipe is made by X65 line pipe steel, the von-Mises stress in pipe is much smaller than the allowable one indicating pipe's structural safety status so far. The proposed method can also be referenced in the status monitoring of buried pipeline crossing other geological hazard regions.

## 1. Introduction

Crude oil is commonly transported by pipelines in the arctic region. With the rising of crude oil temperature in the pipeline, buried heated oil pipeline with insufficient insulation is always affected by permafrost thawing. Subjected to the thaw settlement load, bending strain can be accumulated in the pipe. The buckling or rupture failures of pipe may happen if bending strain becomes larger than the ultimate strain of pipe [1]. In order to ensure the safe and efficient operation of pipelines in frozen soil areas, lots of researchers

and pipeline operators have conducted relative research studies.

Since field monitoring data are the fundamental information reflecting pipe's mechanical states, various monitoring methods have been investigated and developed for pipeline status monitoring. Generally, the permafrost temperature field can be monitored by distributed temperature sensors. The thawing depth around the pipe can be analyzed based on the temperature field results or measured directly. For pipeline itself, commonly pipe strain was monitored to calculate pipe's stress component. While no techniques are



able to sensor the absolute strain values in pipe so far, pipe strain components such as the bending strain component or the longitudinal strain increment component are commonly monitored. Pipe bending strains and longitudinal strains can be obtained based on the inertial measurement unit (IMU) and strain gauge monitoring system, respectively. Specifically, Wang et al. [2, 3] presented the layout of one special soil temperature monitoring system at four monitoring sites of an inservice oil pipeline crossing different geohazard areas. Based on the new developed system, variations of the thawing depth around pipe in recent years were obtained. Tan et al. [4] proposed a pipeline displacement monitoring technology based on total station surveying technique, which has been successfully applied in the displacement monitoring in permafrost regions. Li et al. [5–7] performed a series of research studies focusing on bending strain detection via IMU assembled in pipeline inline inspection tool, and this technology was employed by the Petrochina Pipeline Company to identify high thawing settlement risk areas. Similarly, Cho et al. [8] developed a bending strain calculation method of pipe bending strain based on the pipeline coordinates derived by IMU. Inaudi [9] conducted some engineering cases application analysis of this kind of strain monitoring systems. Glisic [10] conducted comparison analysis of strain monitoring results via different fiber optic strain sensors. Lei et al. [11, 12] summarized the dent strain detection methods based on the inline inspection data. Rajeev et al. [13] gave a brief overview of optical fiber technologies and outlined potential applications of these technologies for geotechnical engineering applications. It can be found that although ground temperature, soil displacements, and pipe strain can be derived more or less, the actual stress states of pipe can still not be sensed comprehensively. Witek et al. [14, 15] provided the method for gas leakage rate estimation method based on defect population. Life cycle estimation of high pressure pipeline was conducted based on inline inspection data. The existing monitoring data can only be adopted to estimate current safety status of pipeline approximately. The high-risk locations of pipeline failure may not be accurately identified, and the variation trend of pipeline's stress response cannot be predicted, which will affect the effectiveness of the pipeline safety assessment.

As for the mechanical analysis of buried pipeline subjected to thawing settlement, several related research studies have also been carried out. For instance, Xu et al. [16] investigated the stresses and strains of pipelines by infield experimental tests, which found that peak stress appears near the boundary of the settlement zone. Liu et al. [17] investigated the effects of soil frost heaving displacement and pipe diameter on the critical buckling axial load of buried heated pipeline based on experimental and numerical analysis. Wen et al. [18, 19] deduced an analytical model considering the strain hardening behaviour of pipe steel and analyzed the stress and deformation responses of pipes under various thawing settlement loads. Xia et al. [20, 21] conducted similar parametric analysis investigations focusing on pipe's deflections. Other researchers employed the numerical analysis models based on finite element method

to investigate pipe's stress and strain responses under various kinds of thawing settlement loads [22, 23]. As mentioned above, small-scale tests and numerical simulation investigations can be referred in stress and strain analysis of pipeline in permafrost zones. However, it can be found that pipe's loading conditions used in these documented research studies are mainly simplified to some types of assumed soil displacement loads which cannot reflect pipe's actual loading conditions monitored from actual engineering cases. Therefore, it is necessary to combine the multisource monitoring data and numerical simulation technology to improve the accuracy of monitoring results for pipe's actual mechanical states.

In this study, multisource monitoring data were employed. A coupling stress evaluation method of pipeline subjected to thawing settlement based on monitoring results and the numerical model was proposed. In the proposed method, thawing settlement was estimated via the soil temperature results, and a pipe soil interaction model based on finite element method was employed to reveal the actual stress states in pipe. A case study shows that the proposed method can accurately predict pipe's stress distributions in the thawing settlement zone, which successfully fills the gap that some most dangerous sections may not be monitored by distributed sensors. This method is also referable for pipelines located in other geohazard regions.

## 2. Monitoring System for Pipes in Permafrost Regions

As mentioned above, multisource monitoring data of pipelines can be obtained by different monitoring techniques. For pipeline crossing thaw settlement regions, two kinds of data are commonly needed, i.e., the environmental data and the pipeline strain data. Generally, as shown in Figure 1, the environmental data include the soil temperatures and the ground settlement displacement, and the pipeline strain data include different strain components, i.e., bending strains and longitudinal strains derived by IMU and strain gauges.

Temperature monitoring results can be used to acquire the variation of temperature field, and the characteristic parameters of permafrost regions, such as maximum depth of frozen soil, annual average surface ground temperature. The displacement monitoring results can be used to obtain the frost heave or thawing settlement displacement of some concerned points. Strain monitoring results can be adopted to determine whether the strain value exceeds the pipeline strain capacity. In the following sections, monitoring technologies which have been applied in the Petrochina Company will be introduced briefly.

### 2.1. Temperature Monitoring System for Frozen Soil.

Temperature field monitoring results of permafrost zones can reveal the variations of soil temperature with the seasonal oil temperatures and climatic changing conditions, which can provide an important reference for determining whether the buried pipeline has frost heave or thaw



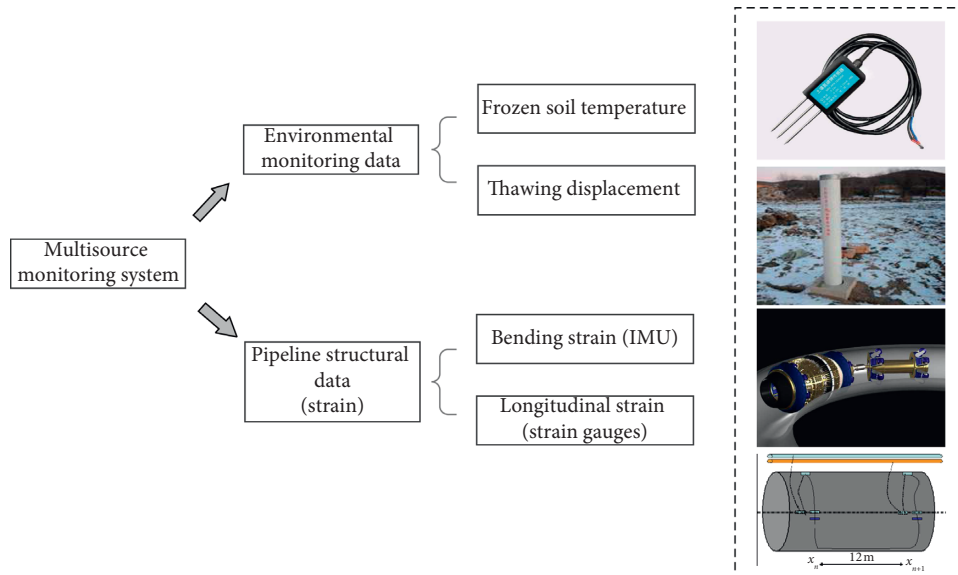


FIGURE 1: Established monitoring system for pipes in permafrost regions.

settlement hazards. Meanwhile, with detected frozen soil characteristic parameters, the maximum thaw settlement of frozen soil can be predicted by analyzing temperature monitoring data. Figure 2 illustrates the infield temperature system used in Petrochina Company. Commonly temperature sensors are distributed 20 meters away from the pipe axis in the horizontal direction and 15 meters beneath the ground surface in the vertical direction in order to get the whole temperature distribution around pipe.

2.2. Pipeline Strain Detection Based on IMU and Fiber Bragg Grating (FBG) Strain Monitoring. IMU inline inspection tool is one common technique to acquire the position and bending strain of pipeline widely employed by pipeline operators recently. Petrochina Pipeline Company also developed a series of inline inspection tools with the inertial measurement unit since 2014 [5], as shown in Figure 3.

The bending strain and bending strain variation characteristics of the entire pipeline can be acquired based on IMU-detected pipeline coordinate data at different time. Figure 4 shows the pipeline coordinate and strain results of one inspected pipeline in Petrochina Pipeline Company. In order to perform the integrity assessment, Petrochina Pipeline Company suggested strain criteria for IMU-detected bending strain, i.e., the absolute strain value and strain variation value should be less than 0.125% and 0.02%, respectively [22]. Based on the strain criteria acquired from Chinese standard GB 32167 Oil and gas pipeline integrity management specification, pipe segments with large bending strains were detected as shown in Figure 4(a). As can be observed from the figure that the longitude of the pipeline varies from 108.8° to 109.4°, the latitude of the pipeline varies from 34.8° to 35.8°, and the variation range of pipeline altitude is 600–1600.

In addition to IMU-based bending strain measurement, fiber Bragg grating (FBG) strain gauges are used to monitor the real-time strain increment of pipes at high-risk thawing

settlement zones. This kind of real-time warning can be helpful for pipeline safety. Figure 5 shows the arrangement of FBG strain gauges on pipes. Generally, three strain gauges are needed for one pipe section, and the longitudinal distance between the monitored pipe sections is set to be around 12 meters.

### 3. Coupling Data Analysis of Multisource Monitoring Data

Based on multisource monitoring data derived by different sensors, a coupling analysis method was proposed in this study. As shown in Figure 6, the analysis process can be divided into the following steps:

- (1) In the first step, the collection and analysis of multisource monitoring data was performed to estimate the possible geohazard types faced by the pipe.
- (2) In the second step, an assumed initial surface displacement of thaw settlement area was set based on multisource monitoring results.
- (3) In the third step, thaw settlement displacement load derived by the second step was applied to the numerical inversion model, and pipe-soil interaction parameters were derived by the filed investigation results.
- (4) In the final step, comparative analysis of pipeline strain detection results and numerical simulation results can be adopted to verify the accuracy of the numerical model. The reliability of numerical results can be improved by adjusting variable parameters of the model to make the performance indices less than allowable criteria. The three indices are the coefficient of determination ( $R^2$ ), mean absolute error (MAE), and root-mean-square-error (RMSE). These indices are commonly used in performance assessment of prediction models. The calculation formulas are listed as follows:

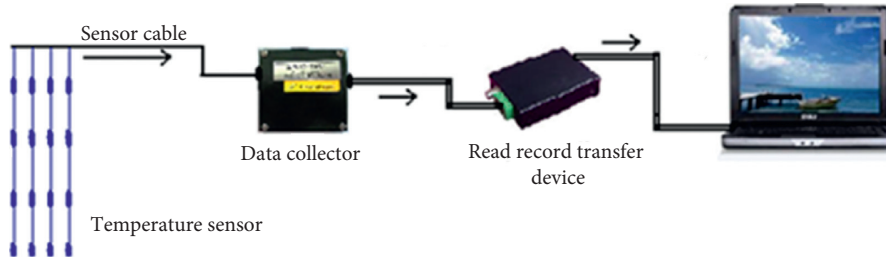


FIGURE 2: Temperature monitoring data acquisition process used in Petrochina Pipeline Company.

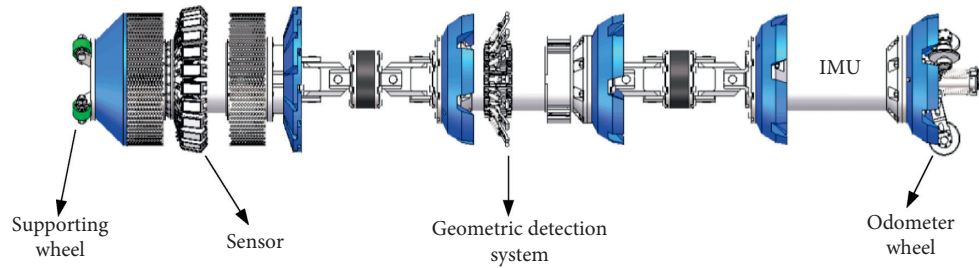


FIGURE 3: Inline inspection tool with IMU developed by Petrochina Pipeline Company.

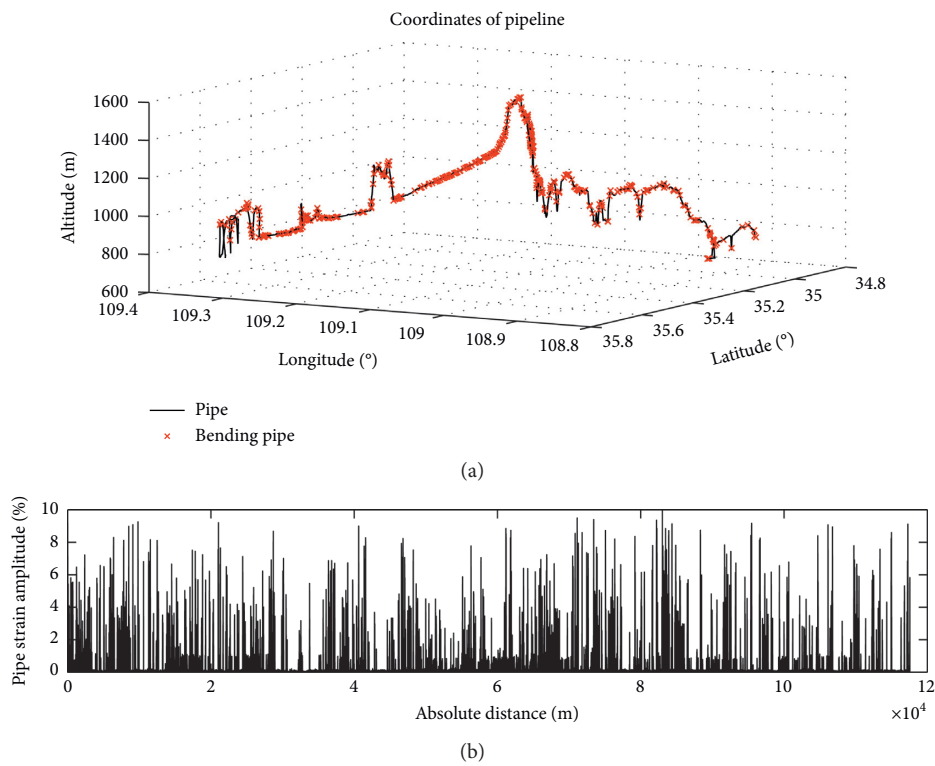


FIGURE 4: Pipe coordinates and pipe strain derived by IMU for one pipeline in China. (a) Pipe coordinates derived by IMU. (b) The primary strain results without treatment derived by IMU.

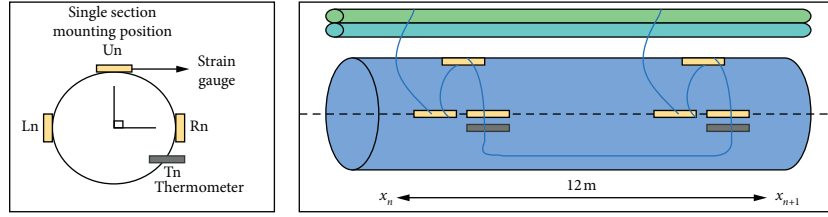


FIGURE 5: Schematic diagram of FBG monitoring used in Petrochina Pipeline Company.

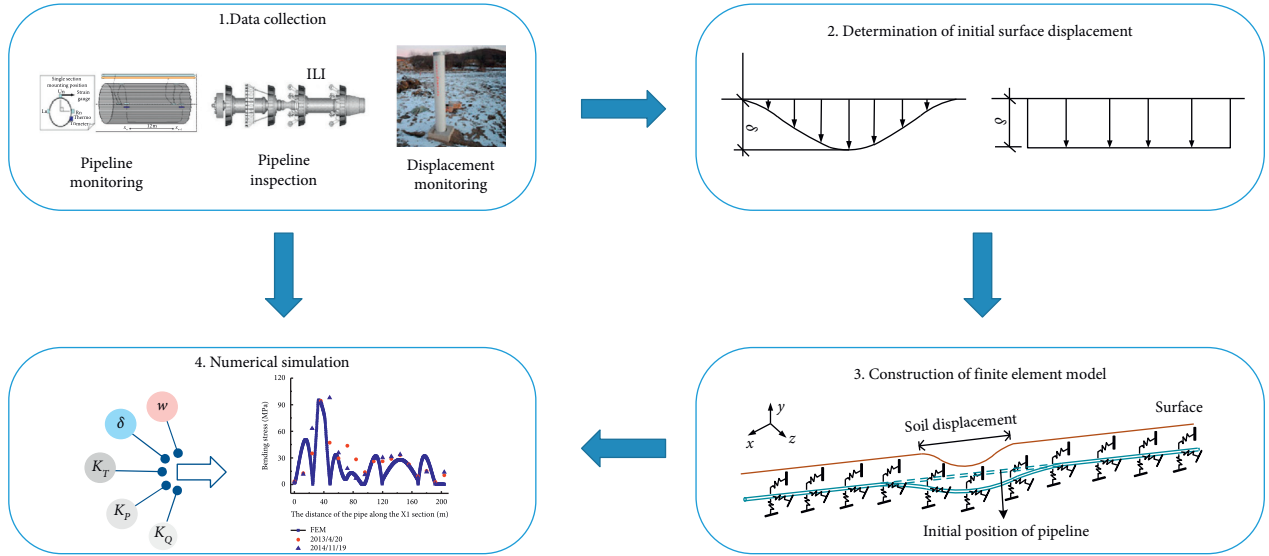


FIGURE 6: Pipeline coupling data analysis based on data analysis and numerical simulation.

$$\left\{ \begin{array}{l} \text{RMSE} = \sqrt{\frac{1}{N} \sum_{i=1}^N (\varepsilon_{ei} - \varepsilon_{mi})^2}, \\ R^2 = 1 - \frac{\sum_i (\varepsilon_{mi} - \varepsilon_{ei})^2}{\sum_i (\varepsilon_{mi} - \bar{\varepsilon}_m)^2}, \\ \text{MAE} = \frac{1}{N} \sum_{i=1}^N |\varepsilon_{ei} - \varepsilon_{mi}|. \end{array} \right. \quad (1)$$

Here,  $N$  is the number of strain values,  $\varepsilon_e$  is the estimated strain value,  $\varepsilon_m$  is the measured strain value, and  $\bar{\varepsilon}_m$  is the average monitored strain values.

The detailed analysis procedure is summarized in Figure 7. The bending strains of the monitored points of pipeline were compared with the measured ones.

#### 4. A Case Study

**4.1. Case Description.** As shown in Figure 8, the AA007 monitoring pipe segment is located 8.5 km away from the investigated pipeline's initial station. Due to the high moisture of surrounding soil and the rising of crude oil

temperature in the pipeline, this area becomes a typical thaw settlement zone. After the operation of the pipe, a comprehensive monitoring system at this location was installed continuously since 2010. As observed in Figure 9, there are 18 monitoring sections set up along the pipeline. The distance between adjacent monitoring sections is about 12 m, i.e., length of a common line pipe segment. Based on filed investigations, the X5-X6 section is located beneath a road, and the pipeline will inevitably be affected by ground surface pressure. Meanwhile, there is a large area of water accumulation at the upstream of X5 section and downstream of X6 section. Due to the existence of thawing area, the thaw settlement risk is significantly increased, which seriously affects the structural safety of the pipe.

**4.1.1. Soil Conditions of the Monitored Area.** The frozen soil in the monitoring area can be divided into three types depending on the soil's depth beneath the ground surface. As shown in Figure 10, they are sandy loam, silty clay, and weakly weathered base rock, respectively. The buried depth of the pipe was 2.5 m. The pipe diameter and pipe wall thickness are 813 mm and 16 mm, respectively. The soil parameters are listed in Table 1, which were acquired from geological investigation data during the pipe design stage. In the thawing settlement analysis, the ground surface

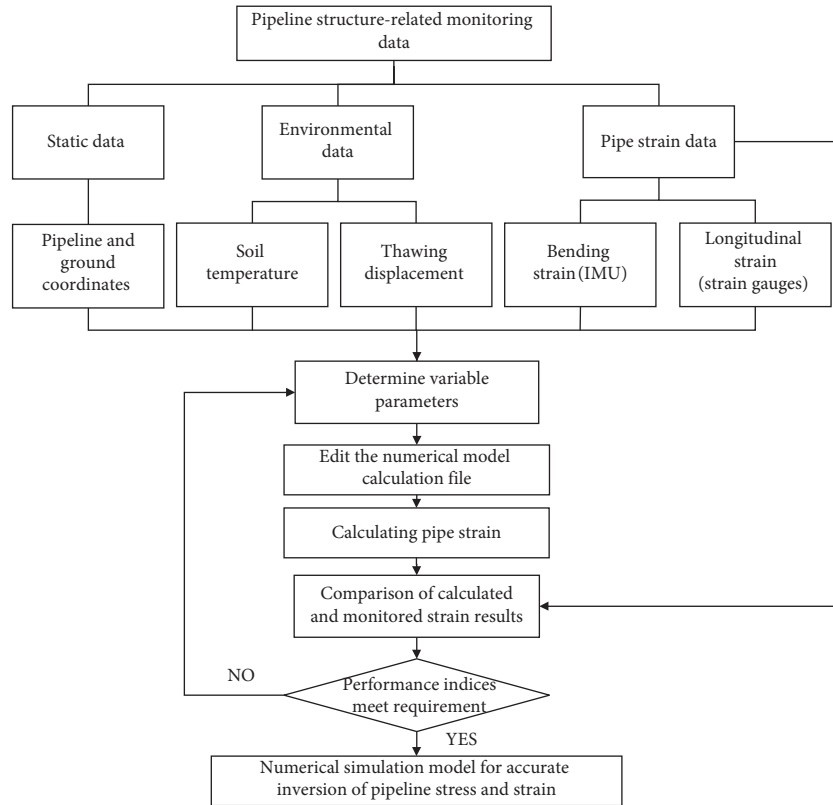


FIGURE 7: Coupling data analysis of pipelines’ mechanical state based on multisource sensing data.



FIGURE 8: Site survey map of AA007.

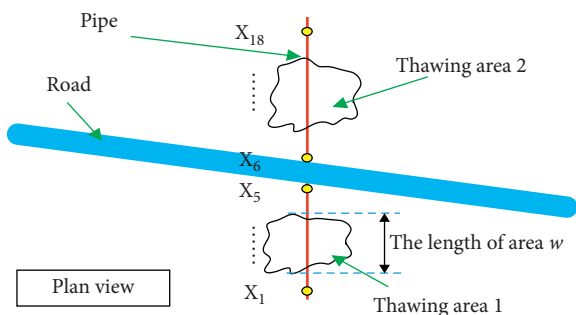


FIGURE 9: Site overview.

displacement can be calculated based on thawing depth of frozen soil and thawing settlement coefficient of the soil.

4.1.2. Trends of Oil Temperatures in the Initial Station.

The investigated crude oil pipeline was put into operation in 2010. The initial designed oil temperature was considered to be  $-6.41^{\circ}\text{C}$  in winter and  $3.65^{\circ}\text{C}$  in summer. While, after the operation, the oil temperature increased continuously. Recently, the maximum oil temperature in summer has increased up to  $28.5^{\circ}\text{C}$ . Trends of the oil temperature of the initial station between 2014 and 2020 is shown in Figure 11. Increased oil temperature increases the risk of thaw

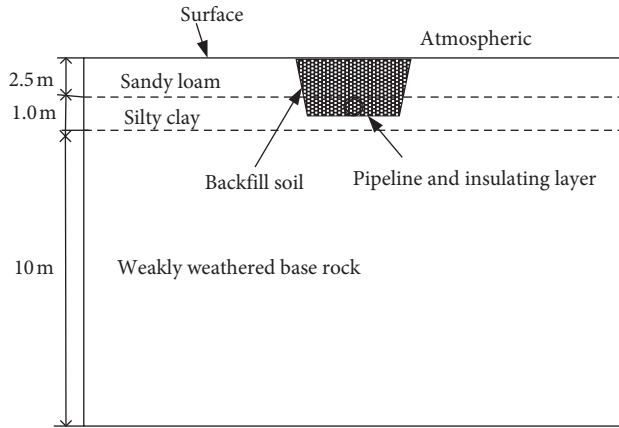


FIGURE 10: Soil distribution in frozen soil area.

TABLE 1: Thermal properties of soil layers.

Physical parameters	$\rho$	$C_f$	$C_u$	$\lambda_f$	$\lambda_u$
Unit	$\text{kg/m}^3$	$10^3 \text{ J}/(\text{kg}\cdot^\circ\text{C})$		$\text{W}/(\text{m}\cdot^\circ\text{C})$	
Sandy loam	1300	1.49	1.88	1.21	0.84
Silty clay	1600	2.54	3.35	1.04	0.72
Weakly weathered base rock	1600	1.50	1.90	2.12	1.42

$\rho$ : density;  $C_f$ : specific heat of frozen soil;  $C_u$ : specific heat of unfrozen soil;  $\lambda_f$ : thermal conductivity of frozen soil;  $\lambda_u$ : thermal conductivity of unfrozen soil.

settlement, which makes monitoring of pipe’s structural states becomes necessary.

4.2. Multisource Monitoring for the Pipe

4.2.1. Temperature Field Monitoring. The risk of thaw settlement in frozen soil area can be evaluated via detailed analysis of the soil temperature around the pipe. The temperature field monitoring system installed in this area is shown in Figure 12(a). The PT100 temperature sensor was selected to monitor the temperature distribution of frozen soil. There are 6 monitoring lines in every section with 168 temperature sensors installed. The L1 monitoring line is located above the pipeline. The other five monitoring lines are installed away from the pipeline laterally. The L6 monitoring line was set a little further away, which can be adopted to monitor the temperature distribution of the soil surround the pipeline under natural conditions. All the temperature data were collected twice a day and transmitted to the integrity management centre via the devices shown in Figure 12(b).

The soil temperature along L1 monitoring line and L6 monitoring line from August 2016 to June 2018 are plotted in Figure 13. As shown in the figure, soil temperature above the pipe is obviously affected by the seasonal meteorological temperature. As for the L1 monitoring line, the temperature of the soil above the pipe decreases with the increase of depth in summer. However, the temperature is monotonically increasing as the depth increases in winter. As for the L6 monitoring line, the soil temperature basically keeps

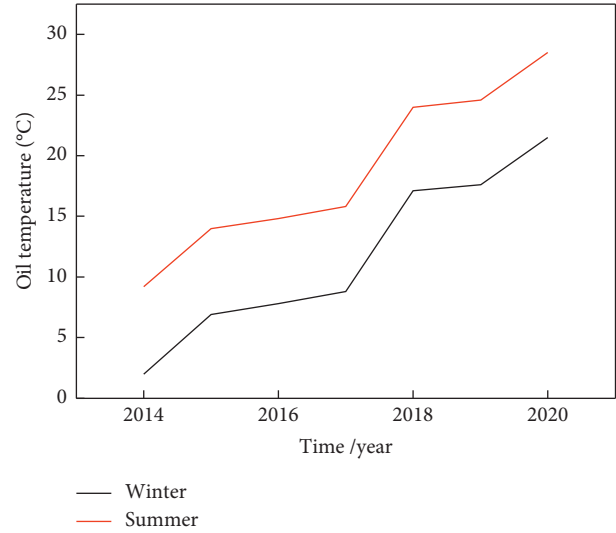


FIGURE 11: Temperature of oil in initial station of the pipeline.

invariant, when the depth is larger than 6 m. When the buried depth varies from 0 m to 2 m, the temperature of frozen soil rises rapidly, which indicated that the rising of crude oil temperature obviously accelerates the thawing of frozen soil around the pipeline.

4.2.2. IMU-Based Bending Strain Detection. IMU monitoring data can be adopted for bending strain analysis of long-distance oil pipeline. Petrochina Pipeline Company has developed several inline inspection tools with IMU modules, which can detect relatively accurate pipe bending strains. Based on the IMU monitoring results, the mechanical state of pipeline can be obtained to a certain extent, which makes quantitative safety assessment of pipelines possible. Figure 14 shows the preparing procedure before the inspection for the considered oil pipeline. Based on the IMU bending strain analysis results, high-risk area with large bending strains can be identified. For this high-risk area, real-time strain monitoring via strain gauges may be considered to ensure pipe’s safety.

Figure 15 illustrates the horizontal and vertical bending strain results for the considered pipe segment. Horizontal strain means the bending strain obtained in the horizontal plane, while the vertical strain means the bending strain obtained in the vertical plane. The strain results can be calculated via the coordinates derived by IMU according to reference [22]. The absolute distance of this pipe segment from the initial station varies from 8215 m to 8416 m. It can be readily observed that the variation of horizontal strain is not obvious, which mainly varies from  $-0.05\%$  to  $0.05\%$ . Thus, the bending strain of this pipe segment is mainly caused by vertical settlement. And the vertical strain derived by IMU peaks at 8353 m away from the initial station with the peak value equals  $0.71\%$ .

4.2.3. Longitudinal Strain Monitoring. Pipeline’s mechanical status also can be monitored via distributed strain gauges.



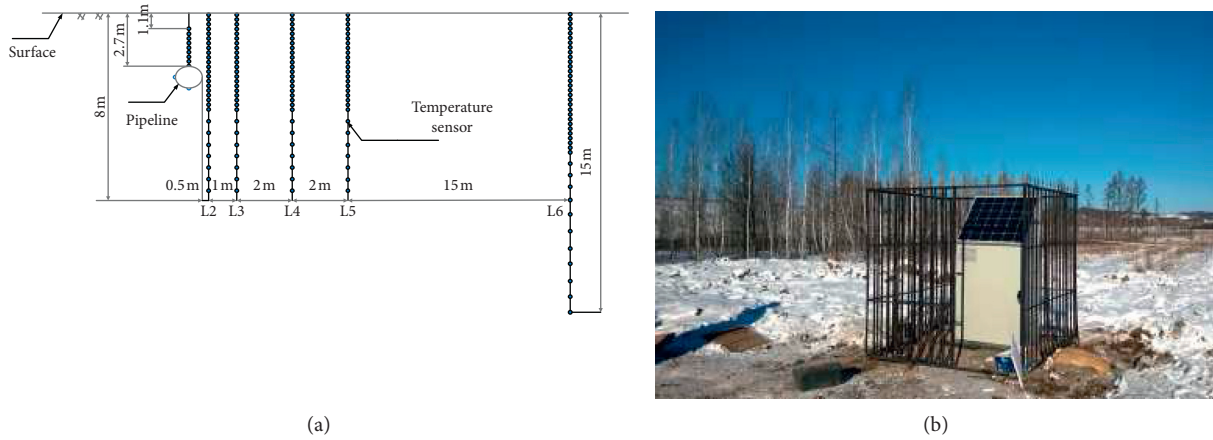


FIGURE 12: Temperature field monitoring system installed in the field. (a) Arrangement of temperature sensor in one pipe section. (b) Data automatic collection centre with solar power.

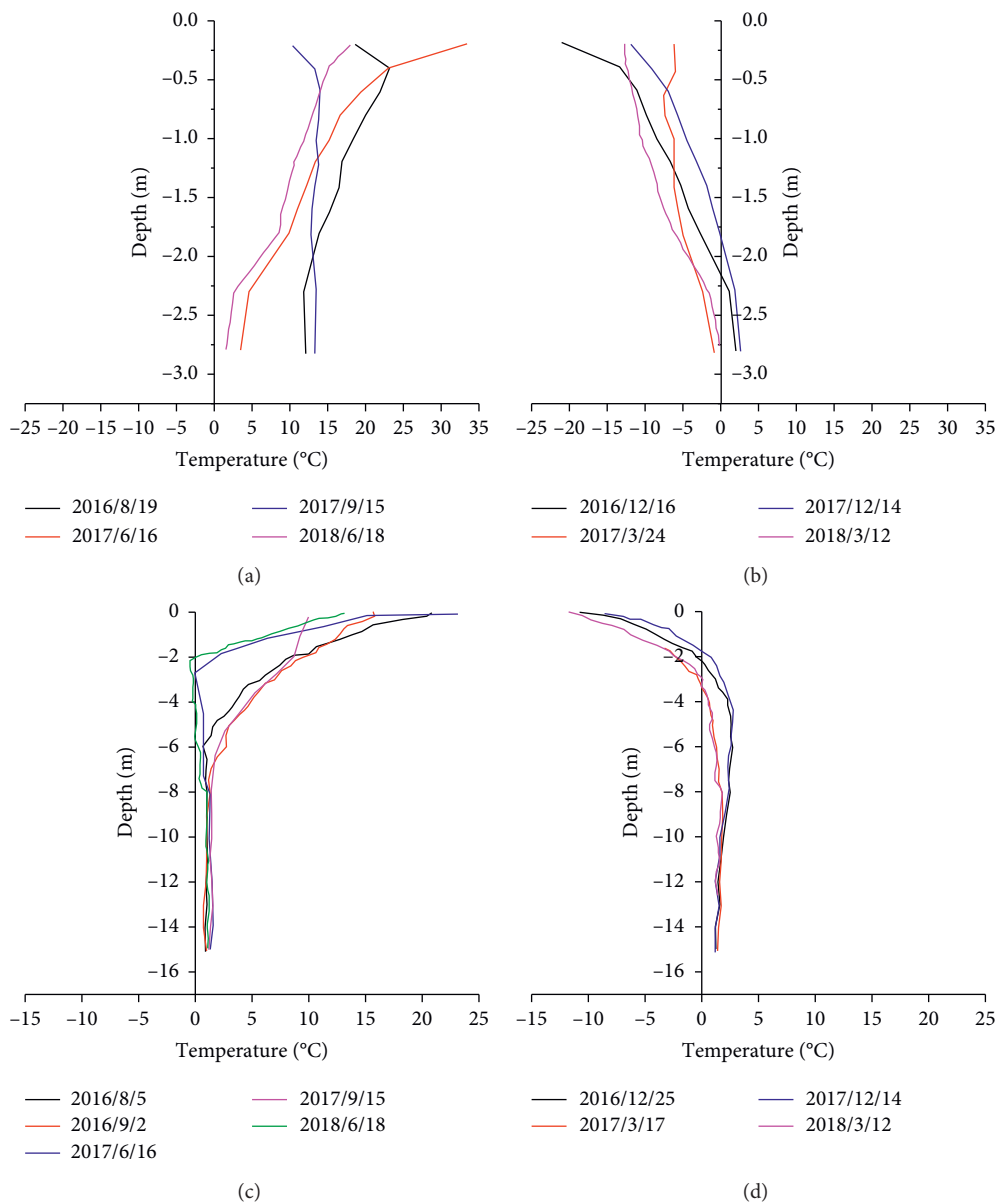


FIGURE 13: Trends of soil temperature with depth at different positions around the pipe. (a) Summer, L1 monitoring line. (b) Winter, L1 monitoring line. (c) Summer, L6 monitoring line. (d) Winter, L6 monitoring line.





FIGURE 14: IMU field inspection.

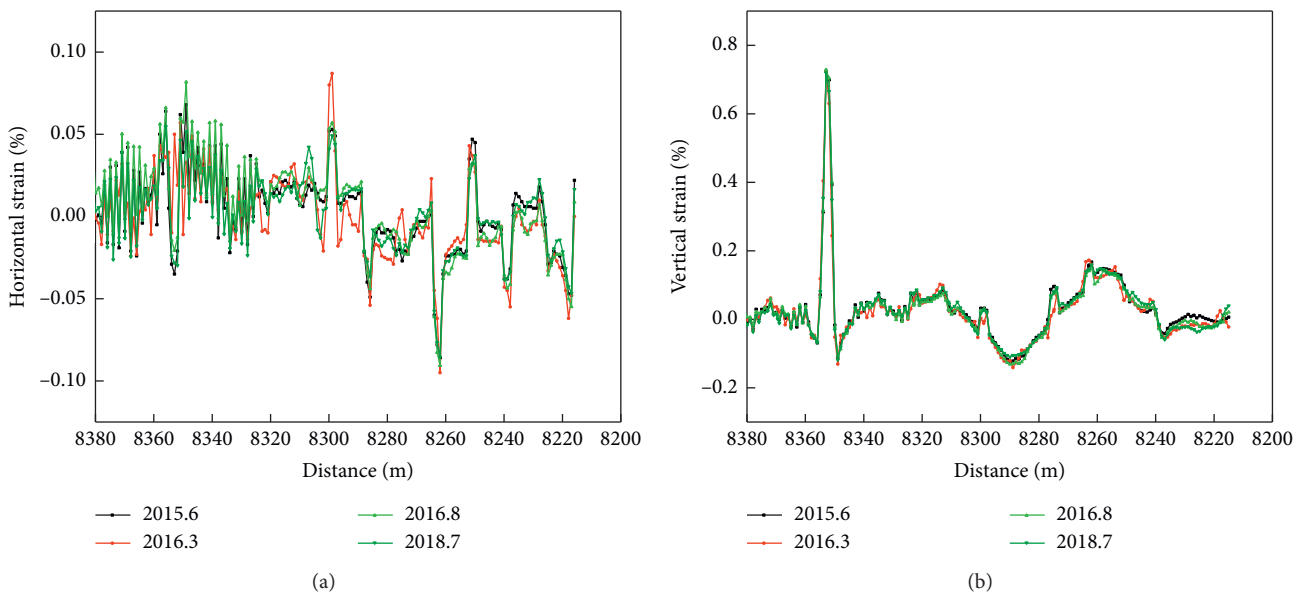


FIGURE 15: Bending strain derived by IMU. (a) Horizontal strain. (b) Vertical strain.

Due to this is a high thawing risk area, longitudinal strain monitoring of this segment has lasted near 10 years. Some bending stress results calculated by the strain gauges of each monitoring section are illustrated in Figure 16. It can be clearly noticed that, after 2010, bending stress has changed significantly from pipe section X2 to pipe section X6 and from pipe section X10 to pipe section X14. The stress value of X4 section has increased obviously, increasing from 10 MPa in 2010 to 149.5 MPa in 2016. However, the stress of X6 section increased slightly. And after 2016, the bending stress of entire pipeline was basically stable.

The comparative analysis of the IMU bending strain and longitudinal stress monitoring results was conducted. As shown in Figure 17, results derived by different technics show similar peak values and distributions. Especially, the peak stress results obtained by the two detection methods are basically the same.

**4.3. Coupling Data Analysis on Pipe’s Mechanical States.** The key of the proposed coupling data analysis method is the pipe-soil interaction model. Based on the accurate numerical model, multisource monitored data can be taken as input

boundary parameter values or output benchmarking targets. By adjusting the numerical model parameters, the true stress and strain distribution in pipe can be obtained, which can be further used in safety assessment.

**4.3.1. Numerical Analysis Model.** Nonlinear finite element method has been widely applied in the mechanical analysis of pipe structures subjected to geohazard loads. A pipe soil interaction model was established in this paper for the considered X65 steel pipeline. The pipe diameter and pipe wall thickness are 813 mm and 16 mm, respectively. Its operation pressure varies from 4 MPa to 6 MPa. In the numerical model, the pipe was modelled by ELBOW element developed by commercial finite element code package ABAQUS, as this special element can consider pipe’s section deformation more accurately comparing with the common pipe elements. In order to eliminate boundary effects, the entire pipe model (Figure 9) was extended to 600 m. As can be observed in Figure 18, a fine mesh with element length of 0.2 m was utilized for the 200 m pipeline in the middle section where settlement zones were located to obtain the accurate mechanical response of pipe subject to thawing

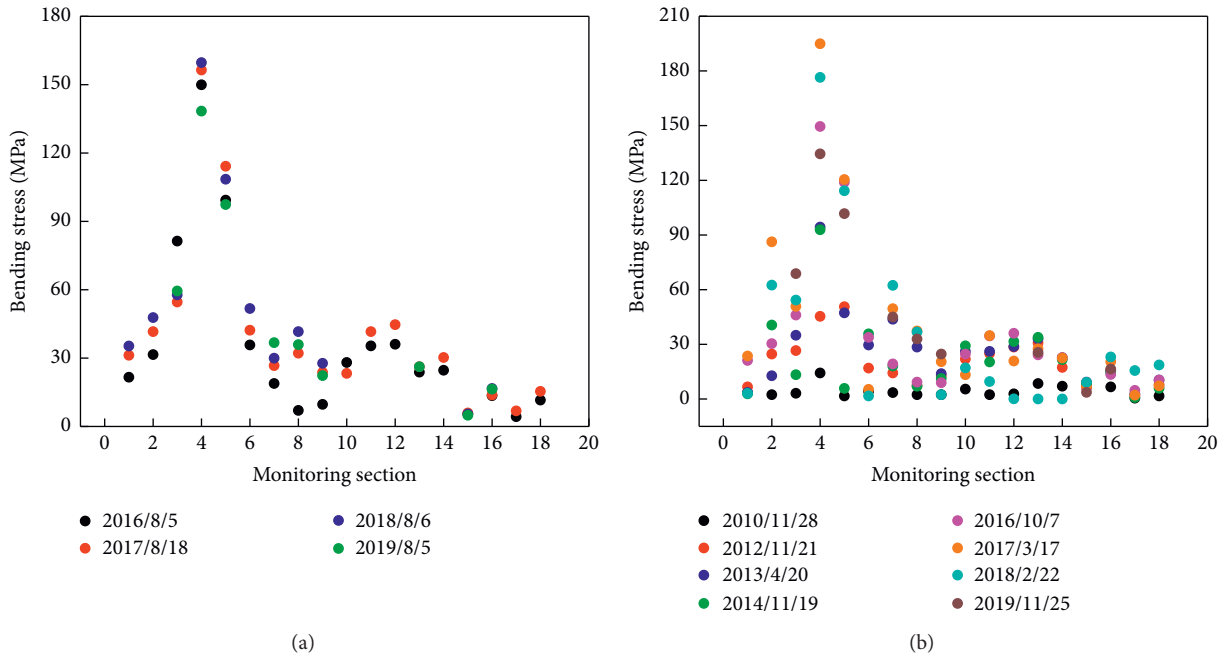


FIGURE 16: Monitor the bending stress distribution. (a) Summer. (b) Winter.

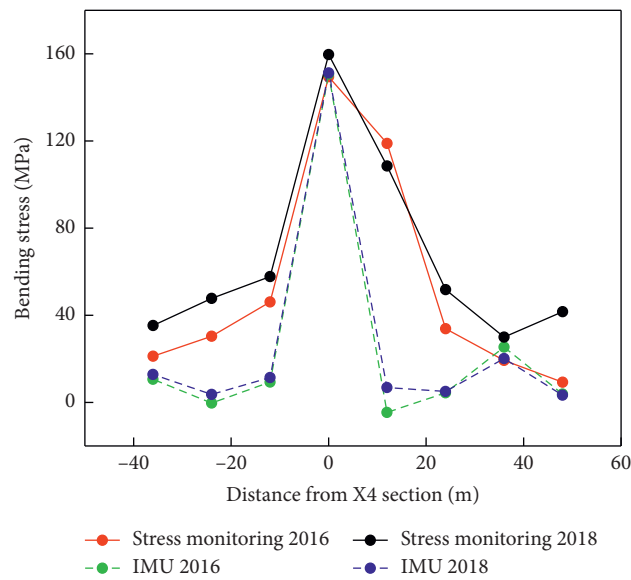


FIGURE 17: Comparison of bending stress and results derived by different methods.

settlement. Meanwhile, a coarse mesh with an element size of 1 m was used for both extended pipes at the two sides.

As shown in Figure 19, the soil resistant force on the pipe can be described by nonlinear springs, which can be realized by the three-dimensional 4-node pipe-soil interaction elements (PSI 34) developed by ABAQUS. The soil spring parameters  $f_{iw}$ ,  $p_{iw}$  and  $q_u$  ( $q_d$ ) represent the maximum soil resistant forces per unit length of pipes in the axial, lateral, and vertical directions. And  $x_{iw}$ ,  $y_{iw}$  and  $z_u$  ( $z_d$ ) represent the yield displacements, respectively. The values of these parameters can be calculated by the equations suggested by the ALA-ASCE guideline [24].

In this study, backfill soil in the pipe trench is medium sand with a cohesive stress of 10 kPa, a friction angle of  $40^\circ$ , and an effective unit weight of  $20 \text{ kN/m}^3$ . However, the site soil is silty clay with a cohesive stress of 10 kPa, a friction angle of  $25^\circ$ , and an effective unit weight of  $17.09 \text{ kN/m}^3$ . The soil spring models are illustrated in Figure 20. According to ALA-ASCE guideline, axial soil spring parameters were calculated by the backfill soil parameters, while the lateral and vertical soil parameters were calculated by site soil parameters. Thus, the soil spring parameter values can be obtained as listed in Table 2.

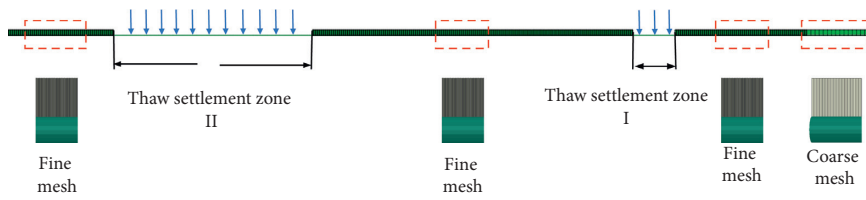


FIGURE 18: Sketch of the finite element model.

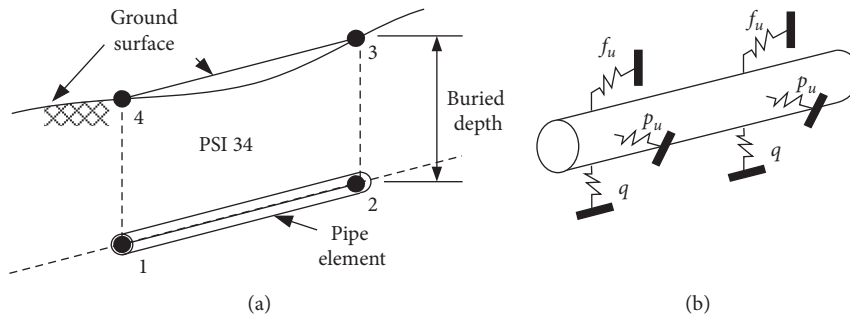


FIGURE 19: Soil springs simulating soil constraints on pipe. (a) PSI unit in ABAQUS. (b) Spring action mode.

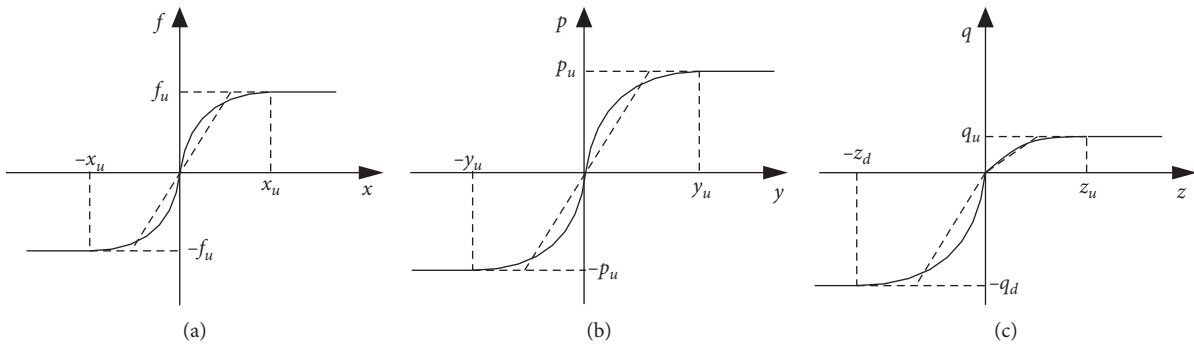


FIGURE 20: Soil spring model in ASCE guide. (a) Axial. (b) Lateral. (c) Vertical.

TABLE 2: Nonlinear soil spring parameters.

	Axial soil spring	Lateral soil spring	Vertical bearing soil spring	Vertical uplift soil spring
Peak soil resistant force (kN/m)	42.9	567.9	3486.8	112
Yield displacement (mm)	5	104.3	101.6	30

In the numerical model, two loading steps were needed. In the first operation load step, internal pressure and temperature loading were applied on the entire pipe. In the second settlement load step, the thaw settlement displacement was applied to the pipe segments in the thawing area. From the field investigation, it can be found that thawing depth of the two thawing area locating from pipe section X2 to pipe section X4 and from pipe section X10 to pipe section X14 should be the same, while the surface loading induced by the road increased the settlement of the X2-X4 zone. Approximate settlement displacements for these two areas were set to be 0.35 m and 0.21 m first. The displacement value can be adjusted during the data analysis process. Figure 21 shows the sketch of the established numerical model.

4.3.2. Mechanical Response of Pipeline in the Thawing Settlement Zone via Coupling Data Analysis. Vertical displacement results of the pipe in 2017 based on the established model and assumed parameters are shown in Figure 22. Due to thaw settlement displacement in zone I is larger, the pipe displacement is also larger. The maximum pipe vertical displacement was 0.36 m in 2017. Figure 23 illustrates the contour plots of the finite element model.

Figure 24 illustrates the comparison results of the multidata-based numerical model and the bending stress values monitored by distributed strain gauges. The results in 2014, 2017, and 2018 were shown as prototypes. Based on the numerical model, variations of pipe's bending stress in the high thawing settlement zone were derived, which can fill the

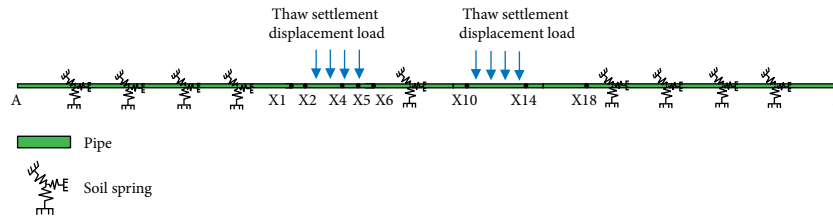


FIGURE 21: Schematic diagram of model boundary conditions.

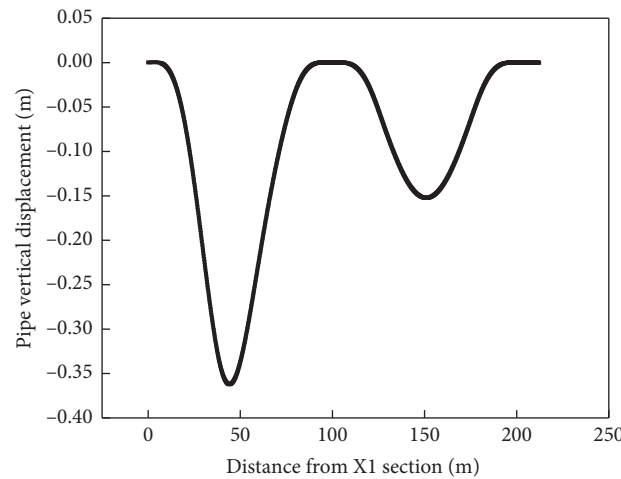


FIGURE 22: Pipe vertical displacement distribution along the pipe axis (2017/6).

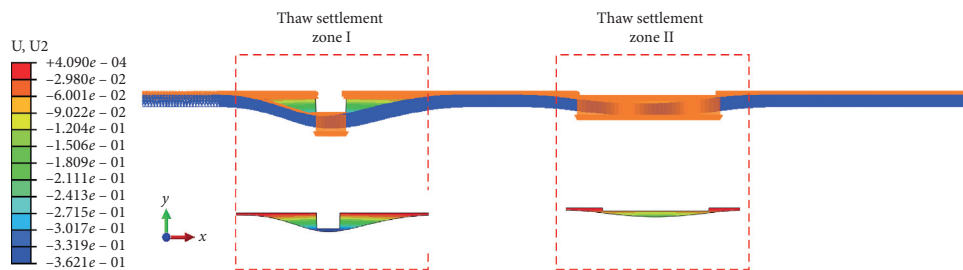


FIGURE 23: Vertical displacement contour results (2017/6).

gap that the strain gauge monitoring system can only monitor 18 pipe sections.

Performance of the proposed method was further studied using three indices, i.e., the coefficient of determination ( $R^2$ ), mean absolute error (MAE), and root-mean-square-error (RMSE). As shown in Table 3, relatively good results were obtained for all the three years, which reflects that the proposed numerical model can predict pipe's structural status reasonably.

Based on the validated numerical model, variations of the peak bending stress, i.e., the bending stress of X4 section from 2010 to 2018 are further discussed as shown in Figure 25. It can be found that, the bending stress of pipeline

due to thaw settlement of permafrost significantly increased before 2016. However, the value of bending stress changes slightly from 2016 to 2018, which is due to the fact that thaw depth has reached the maximum depth of frozen soil. As soil constraint stiffness may increase a little in winter, the bending stress of pipeline is slightly larger than that in summer. In general, the maximum Mises stress in pipeline is 282 MPa, which is less than the allowable stress, i.e.,  $0.9 \sigma_s$  (SMYS of X65 line pipe steel, 405 MPa). The comparative analysis of numerical simulation results and stress detection results show that the numerical inversion model can accurately reflect pipe's true mechanical status.

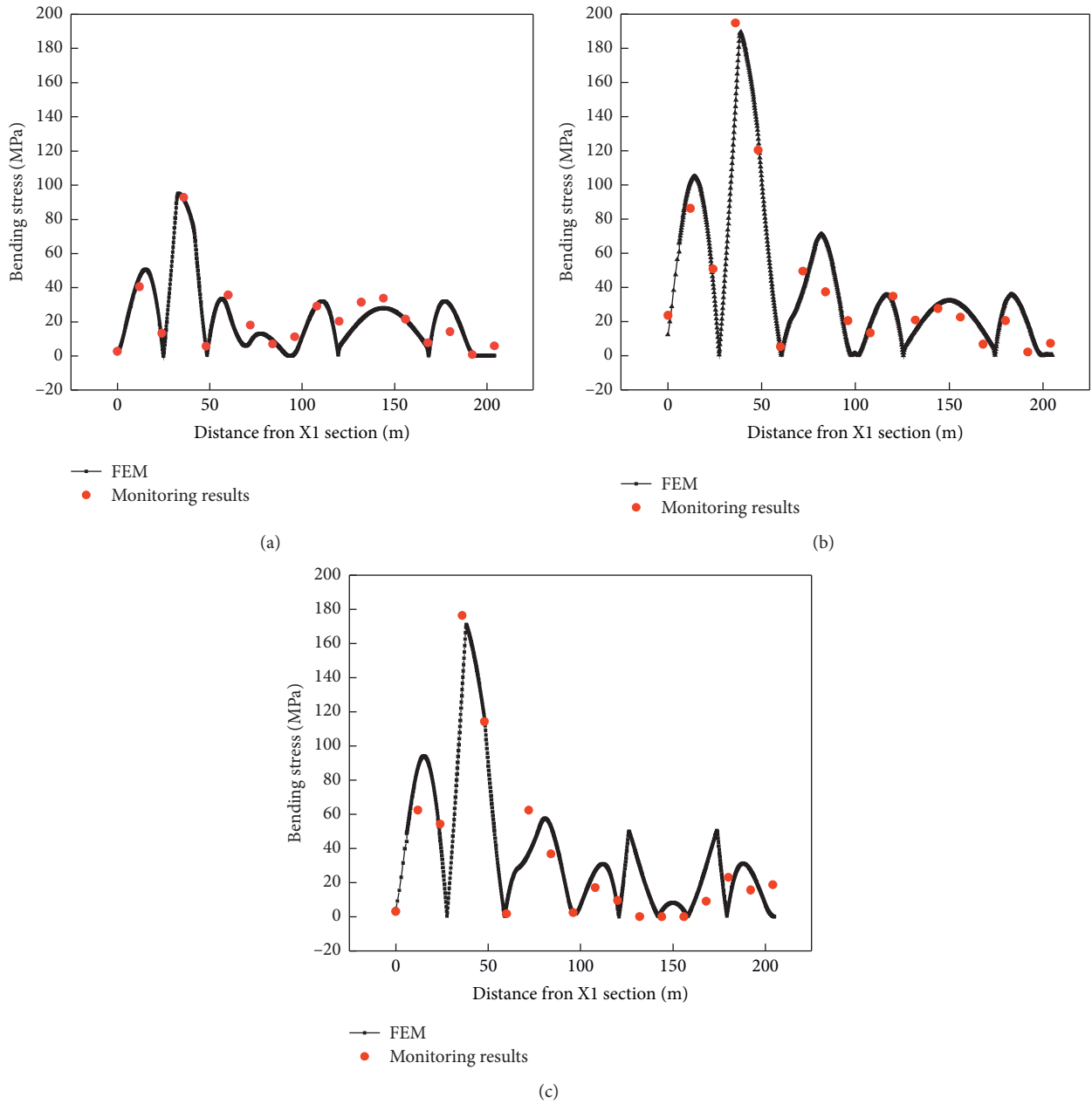


FIGURE 24: Bending stress of pipeline versus distance from X1 section for various years. (a) X1-X18 section (2014/11/19). (b) X1-X18 section (2017/3/17). (c) X1-X18 section (2018/2/22).

TABLE 3: Performance of the proposed multidata-based numerical model.

Date	$R^2$	MAE	RMSE
2014/11/19	0.882	5.77	7.60
2017/3/17	0.875	12.13	16.46
2018/2/22	0.850	13.55	17.80

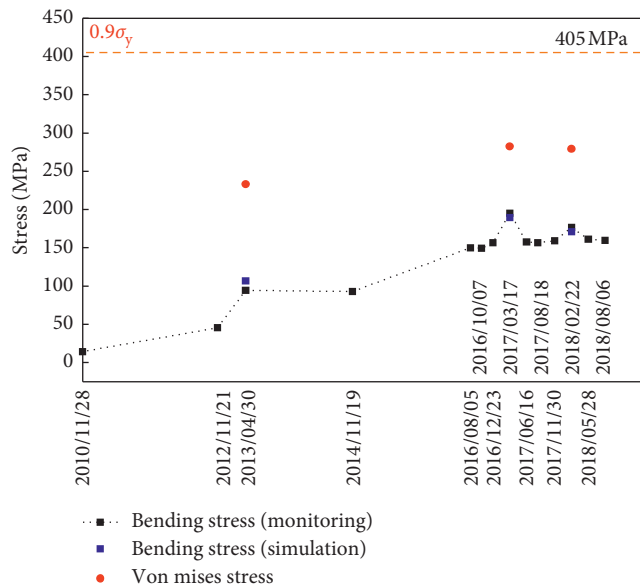


FIGURE 25: Variation of peak stress in pipe from 2010 to 2018.

## 5. Conclusions

Stress analysis of the buried heated oil pipeline crossing permafrost areas via multisource monitoring data-based numerical method was studied in this paper. Taking one heated pipeline in northeastern China as prototype, a general coupling data analysis procedure was proposed. Results show that based on the pipe soil interaction model assumed according to monitoring data, the pipe's overall stress state in the geohazard area can be more accurately obtained, which fills the gap that monitoring data can only reflect the monitored pipe section's mechanical states. Based on the investigation, some remarkable conclusions can be drawn as follows:

- (1) IMU bending strain results and strain gauge-based longitudinal strain results both can reflect pipe's mechanical states to some extent. Consistent peak stress and strain results and distributions were found by these monitoring methods in the considered case in the presented paper.
- (2) Nonlinear soil springs-based pipe soil interaction model with reasonable soil parameters can reflect pipe's mechanical loading induced by frozen soils, as quite small error was found between the proposed numerical model and the filed monitoring results.
- (3) The proposed method can reveal pipe's actual stress state precisely. For the considered X65 pipeline, three years' numerical results show that the maximum relative error of pipe's peak bending stress is less than 15%.
- (4) For the investigated pipeline, the peak stress was found based on the proposed method is located at section X4. The peak bending stress in pipe increased from 10 MPa to 149.5 MPa during 2010 to 2016. The vertical strain of this section achieved the maximum

value of 0.73% in 2016. After 2016, the thawing settlement in this area becomes stable, and only small stress variations appear in the pipe due to the seasonal temperature change.

- (5) Based on the application results, it can be found that safety assessment of buried heated oil pipeline crossing permafrost areas can be evaluated more quantitatively based on the established model.
- (6) The proposed coupling data analysis method can also be referred in stress/strain analysis of buried pipeline crossing other types of geohazards, such as mining subsidence regions and landslide regions. Based on the multisource monitoring data of pipeline, the possible geohazard types faced by the pipe and assumed initial surface displacement can be determined, which can be used for the establishment of numerical inversion model. The comparative analysis of simulation results and monitoring results was adopted to verify the reliability of the inversion results. Based on the relatively accurate inversion model, assessment of pipeline safety status subjected to geological hazard was conducted.

## Data Availability

The data used to support the findings of this study are included within the article.

## Conflicts of Interest

The authors declare no conflicts of interest.

## Acknowledgments

This research has been cofinanced by the National Science Foundation of China (no. 52004314); Tianshan Youth Program (no. 2019Q088); China National Key Research and Development Project (no. 2016YFC0802105); Science Foundation of China University of Petroleum-Beijing (nos. 2462018YJRC019 and 2462020YXZZ045); and China Petroleum Science and Technology Innovation Fund (no. 2017D-5007-0606).

## References

- [1] ASME B31.4-2016, *Pipeline Transportation Systems for Liquids and Slurries*, ASME B31.4-2016, New York, NY, USA, 2016.
- [2] F. Wang, G. Y. Li, W. Ma et al., "Permafrost thawing along the China-Russia crude oil pipeline and countermeasures: a case study in jiagedaqi, northeast China," *Cold Regions Science and Technology*, vol. 155, 2018.
- [3] F. Wang, G. Y. Li, W. Ma et al., "Pipeline-permafrost interaction monitoring system along the China-Russia crude oil pipeline," *Engineering Geology*, vol. 254, no. 2, Article ID 03013, 2019.
- [4] D. J. Tan, J. Zhen, Y. B. Ma et al., "Displacement monitoring of mohe-daqing oil pipeline in the permafrost area," *Oil & Gas Storage and Transportation*, vol. 31, no. 10, 2012.
- [5] R. Li, L. Zhang, X. L. Zhao et al., "Long-term strain and displacement monitoring of long-distance oil-gas pipeline,"



- China Petroleum Machinery*, vol. 44, no. 6, Article ID 06026, 2016.
- [6] F. X. Wang, Q. S. Feng, J. X. Yang et al., "Inertial surveying internal detection method and its application in oil and gas pipeline," *Oil & Gas Storage and Transportation*, vol. 31, no. 5, 2012.
- [7] B. J. Yue, Y. Q. Tang, Y. J. Zhang et al., "Application of integrated navigation technology in inertial pipeline surveying system," *Journal of Chinese Inertial Technology*, vol. 16, no. 6, 2008.
- [8] S. H. Cho and E. S. Lee, "A development of 3-dimensional coordinates monitoring system for underground pipeline using IMU sensor," *Applied Mechanics and Materials*, vol. 1975, Article ID 2749, 2012.
- [9] D. Inaudi, "Distributed optical fiber sensors for strain and deformation monitoring of pipelines and penstocks," *Geotechnical Engineering Journal of the SEAGS & AGSSEA*, vol. 50, no. 2, 2019.
- [10] B. Glisic, "Comparative study of distributed sensors for strain monitoring of pipelines," *Geotechnical Engineering Journal of the SEAGS & AGSSEA*, vol. 50, no. 2, 2019.
- [11] Z. Q. Lei, J. Chen, F. X. Wang et al., "A calculation method for the strain of pipeline dents based on ILI data," *Oil & Gas Storage and Transportation*, vol. 35, no. 2, 2016.
- [12] P. Zhang, Z. Y. Pu et al., "Comparative analysis of magnetic and ultrasonic method data on defects in pipeline," *China Safety Science Journal*, vol. 24, no. 10, 2014.
- [13] P. Rajeev, J. Kodikara et al., "Distributed optical fibre sensors and their applications in pipeline monitoring," *Key Engineering Materials*, vol. 2436, Article ID 558424, 2013.
- [14] M. Witek, "Life cycle estimation of high pressure pipeline based on in-line inspection data," *Engineering Failure Analysis*, vol. 104, 2019.
- [15] M. Witek, A. Batura, I. Orynyak et al., "An integrated risk assessment of onshore gas transmission pipelines based on defect population," *Engineering Structures*, vol. 173, 2018.
- [16] G. F. Xu, J. L. Qi, H. J. Jin et al., "Model test study on influence of freezing and thawing on the crude oil pipeline in cold regions," *Cold Regions Science and Technology*, vol. 64, no. 3, Article ID 04010, 2010.
- [17] X. B. Liu, H. Zhang, M. Y. Xia et al., "Research on experimental method of upheaval buckling of pipeline in permafrost zone," *Petro-Chemical Equipment*, vol. 43, no. 4, 2014.
- [18] Z. Wen, Y. Sheng, H. J. Jin et al., "Thermal elasto-plastic computation model for a buried oil pipeline in frozen ground," *Cold Regions Science and Technology*, vol. 64, no. 4, Article ID 01009, 2010.
- [19] Y. P. Wu, Y. Sheng, Y. Wang et al., "Stresses and deformations in a buried oil pipeline subject to differential frost heave in permafrost regions," *Cold Regions Science and Technology*, vol. 64, no. 3, Article ID 07004, 2010.
- [20] M. Y. Xia, H. Zhang et al., "Stress and deformation analysis of buried gas pipelines subjected to buoyancy in liquefaction zones," *Energies*, vol. 11, no. 9, 2018.
- [21] W. Wang, W. Y. Xia, H. N. Liu et al., "Sensitivity of influencing factors of freezing and thawing of pipeline foundation in permafrost regions," *Oil & Gas Storage and Transportation*, vol. 39, no. 10, 2020.
- [22] X. M. Zhao, R. Li, P. C. Chen et al., "Identification and evaluation on bending deformation of China-Russia eastern gas pipeline," *Oil & Gas Storage and Transportation*, vol. 39, no. 7, 2020.
- [23] X. B. Liu and H. Zhang, "Numerical analysis and strength evaluation of an exposed river crossing pipeline with casing under flood load," *Periodica Polytechnica Civil Engineering*, vol. 62, 2018.
- [24] American Lifelines Alliance (ALA), *Seismic Guidelines for Water Pipelines*, G&E Engineering Systems Inc., Oakland, CA, USA, 2005.